Vehicle Dynamic and Control of Constrained Multi-Actuation Systems at the Limits of Handling

by

Shamim Mashrouteh

A thesis
presented to the University of Waterloo
in fulfillment of the
thesis requirement for the degree of
Doctorate of Philosophy
in
Mechanical and Mechatronics Engineering

Waterloo, Ontario, Canada, 2021

Examining Committee Membership

External Examiner	NAME: Zuomin Dong Title: Professor, University of Victoria, B.C.
Supervisor(s)	NAME: Amir Khajepour Title: Professor
	NAME: Ebrahim Esmailzadeh Title: Adjunct Professor, Ontario Tech University
Internal Member	NAME: Kaan Erkorkmaz Title: Professor
Internal Member	NAME: Ehsan Hashemi Title: Adjunct Assistant Professor, University of Alberta
Internal-external Member	NAME: Naser Lashgarian Azad Title: Associate Professor

Author’s Declaration

I hereby declare that I am the sole author of this thesis. This is a true copy of the thesis, including any required final revisions, as accepted by my examiners.

I understand that my thesis may be made electronically available to the public.

Abstract

With recent advances in electric vehicles, having electric motors directly driving the wheels is gaining attraction. When a vehicle is equipped with four independent electric hub motors or independently controlled brakes in each of the four wheels, it gives the control designers the option of controlling each wheel independently in real-time. Independent torque distribution enables developing optimal torque distribution systems for various objective functions. A good example of the benefits of an independent torque distribution strategy is the ability to maximize the vehicle's lateral grip. When a vehicle is operated at the friction handling limits, optimizing the lateral grip will maximize the vehicle maneuverability resulting in reduced vehicle’s oversteer or understeer behavior. Vehicle dynamics at the limits of handling is highly nonlinear, and hence, detailed dynamic analysis is necessary to understand the behavior of the vehicle.

In this dissertation, the equations of motion of a vehicle driven on a road with the bank and grade angles are derived. The effect of these angles on the nonlinear vehicle dynamic model is studied and compared with a high-fidelity CarSim model for evaluation. A comprehensive dynamic analysis, based on the phase portrait method, is performed to investigate the effect of axle torque distribution on the stability of the vehicle dynamics. Inspired by the dynamic square method, an optimal torque distribution method is studied with the objective of maximizing the vehicle's lateral grip while the vehicle remains at its friction handling limit is developed. An optimal torque distribution algorithm is then developed in the form of a feedforward controller for two different configurations, one for the axial torque distribution and one for the corner torque distribution. The controllers are evaluated through simulation and experimental studies and results show improvement in both maneuverability and stability when the vehicle is operated at the handling limits.

The new optimal actuation strategy is extended to controller design for performance vehicles equipped with active aerodynamic systems. Active aerodynamic systems are one of the few actuators capable of increasing normal loads acting on the wheels. Increasing the wheels' normal loads would result into

higher tire-ground forces, hence providing higher brake/drive torque inputs. A control platform consists of a feedforward controller and a constrained feedback model predictive controller (MPC) is developed for such performance vehicles equipped with a front and rear active aerodynamic system. The objective function of the feedback MPC is for the yaw tracking, while the objective of the feedforward controller is to maximize the vehicle lateral grip. This new controller will optimize the active aerodynamic actuation system to maximize vehicle performance and maneuverability. The controller provides the optimal angle of attack for each aero surface so that the yaw tracking error be minimized. The controller has been evaluated in the CarSim simulation environment.

Subsequently, the optimal torque distribution and the active aerodynamic controller are integrated into the form of a constrained multi-actuation model predictive control structure. The actuators of this control system are the four in-wheel independent electric motors and the two active aerodynamic surfaces at the front and rear of the vehicle. The control structure has constraints on the vehicle states, input amplitudes, and the input increments. The objective of the controller is to stabilize the vehicle while minimizing the yaw tracking error. A constraint adjustment module is designed to observe the actuators' constraints. This module prevents any excessive actuation command by adjusting the input constraints. This will minimize the cost and energy and reduce the computational time of the optimization solver by deactivating unnecessary actuators. The proposed multi-actuation controller is simulated and verified on CarSim and the obtained results are presented with detailed explanations.

Acknowledgment

First of all, I would like to express my sincere gratitude to my supervisors, Prof. Amir Khajepour and Prof. Ebrahim Esmailzadeh for their endless support, passion for research, and encouragement during these years.

I would like to thank Dr. Seyed Alireza Kasaiezadeh in General Motors Research and Development Center in Warren, MI, for sharing his valuable knowledge generously and being such a great mentor during my PhD research. I also would like to acknowledge the financial support of Automotive Partnership Canada, Ontario Research Fund, and General Motors. I would like to thank Dr. Bakhtiar Litkouhi, and Dr. Shih-ken Chen in General Motors Research and Development Center in Warren, MI, for their technical support.

I also would like to thank the technicians in the Mechatronic Vehicle Systems laboratory, Jeff Graansma for his great driving skills. He was a great help in the experimental test presented in this research.

From the bottom of my heart, I want to thank my family without whom I would never be able to take even one step in this journey.

In the end, I want to dedicate this thesis to my beloved husband, Arash Fattahi, for his endless love, patience, and support.

I was truly blessed for having such amazing people next to me during my PhD research. None of these would be possible without them.

Dedication

*To my beloved husband, **Arash**,*

for being an endless source of support and encouragement during all challenges of graduate studies and life.

To my family

who are always encouraging me with their greatest love and support.

Table of Contents

Examining Committee Membership ii

Author's Declaration iii

Abstract iv

Acknowledgment vi

Dedication vii

List of Figures xii

List of Tables xvii

Nomenclatures xviii

Greek Nomenclatures xxii

Chapter 1 Introduction 1

1.1. Motivations 1

1.2. Objectives 4

1.3. Thesis Outline 5

Chapter 2 Literature Review and Background 7

2.1. Vehicle Dynamics at the Limits of Handling 7

2.1.1. "g-g" Diagram 8

2.1.2. Dynamic Square 10

2.1.3. Friction Estimation at the Limits of Handling 11

2.2. Vehicle Stability Analysis Based on Phase Portrait Approach 12

2.3. Vehicle Stability and Control with Torque Distribution Method 16

2.4. Vehicle Stability and Control with Active Aerodynamic Systems 19

2.5. Control and Stability of Multi-Actuation and Constrained Systems 21

2.6. Vehicle Dynamics on Non-Flat Road 23

Chapter 3 Vehicle Dynamics Modeling on Non-flat Roads 24

3.1. Vehicle Motions on Non-Flat Road 25

3.1.1. Combined Slip Tire Model 30

3.2. Vehicle Dynamic Model 32

3.3. Non-flat Road Effect on the Open-Loop Vehicle Dynamics 35

3.4. Summary 40

Chapter 4 Optimal Torque Distribution at Limits of Handling 41

4.1. Torque Distribution Based on Dynamic Square 42

4.2. Phase Portrait Analysis 48

4.3. Optimal Axial Torque Distribution 55

4.3.1. State-Space Representation 56

4.3.2. Actuation Dynamics 61

4.3.3. Performance Index 63

4.3.4. Constraints 64

4.3.5. Quadratic Programing Problem 65

4.3.6. Feedforward Axial Torque Distribution Controller 66

4.3.7. Simulation Results 67

4.3.8. Experimental Results 75

4.4. Optimal Corner Torque Distribution 80

4.4.1. State-Space Representation 80

4.4.2. Actuation Dynamics 83

4.4.3. Performance Index 85

4.4.4. Constraints 85

4.4.5. Quadratic Programing Problem 86

4.4.6. Feedforward Corner Torque Distribution Controller 87

4.4.7. Experimental Results 88

4.5. Summary 94

Chapter 5 Active Aerodynamic Control System 96

5.1. Active-Aerodynamic System Modeling 97

5.2. Active-Aerodynamic control system 100

5.2.1. Feed-Forward Active Aerodynamic Control 101

5.2.2. Feedback MPC Active Aerodynamic Control 103

5.3. Simulation Results 110

5.3.1. Straight Accelerating 110

5.3.2. Double Lane Change 113

5.4. Summary 116

Chapter 6 Optimal Torque Distribution and Active Aerodynamics Control Integration 118

6.1. Control System Design 118

6.1.1. Prediction Model 119

6.1.2. Constraints 125

6.1.3. High-Level Constraint Adjustment Module 127

6.1.4. Objective Function 128

6.2. Simulation Results 129

6.2.1. Sinusoidal Steering Input on Dry Road 129

6.2.2. Acceleration in Turn on Dry Road 132

6.2.3. Acceleration in Turn on Wet Road 133

6.3. Summary 134

Chapter 7 Conclusions and Future Work 136

7.1. Conclusions 136

7.2. Future Work 138

References 140

List of Figures

Figure 1-1. Tire Forces with respect to tire slip ratio and slip angle [1] 2
Figure 1-2. Effect of slip ratio on tire capacity. 3
Figure 2-1. Formula SAE racecar g-g diagram at the limits of handling [7] 8
Figure 2-2. Circle model of "g-g" diagram for vehicle limit handling 9
Figure 2-3. Dynamic square 10
Figure 2-4. Phase portrait of a planner vehicle model with no steering angle effect [28] 13
Figure 2-5. A stability envelope that divides stable and unstable regions 14
Figure 2-6. 3-D Phase portrait having steering and braking as control actions [35] 16
Figure 2-7. Optimal torque distribution based on Dynamic Square 19
Figure 3-1. Schematic modeling of vehicle on road with bank and grade angles 26
Figure 3-2. Rotation of the coordinate system as the vehicle moves along the inclined road 28
Figure 3-3. A double-track vehicle model 33
Figure 3-4. The path with gradient and bank angle: (a) 3-D view, (b) X-Y view, (c) X-Z view 36
Figure 3-5. Road angles of the path used in the CarSim simulation 37
Figure 3-6. Steering command to the vehicle 37
Figure 3-7. Open-loop Vehicle response obtained from CarSim® and mathematical modeling with and without road angles effect: (a) longitudinal velocity, (b) lateral velocity, (c) yaw rate 39
Figure 4-1.Effect of slip ratio on tire capacity 41
Figure 4-2. Dynamic Square 44
Figure 4-3. Dynamic Square and the optimal torque distribution 45
Figure 4-4. Road friction coefficient effect on the Dynamic Square 48
Figure 4-5. Open-loop dynamic and safe envelope, $vx = 40$ km/h, $\mu = 0.85$, and $\delta = 0$ 49
Figure 4-6. Open-loop dynamic sensitivity to torque distribution, $T = 1500$ Nm, $\mu = 0.55$, and $\delta = 0$ 51

Figure 4-7. Open-loop Dynamics and safe envelop ($\mu = 0.55$, $vx0 = 10$ m/s, $\tau = 1500$ Nm, $\delta = 0$) : (a) $Tf = 0.3T$, $Tr = 0.7T$, (b)) $T = 0.4T$, $Tr = 0.6T$, and , (c)) $Tf = 0.5T$, $Tr = 0.5T$ 53
Figure 4-8. Drive torque effect on vector field, $vx, 0 = 10$ m/s, $\mu = 0.55$, $\delta = 0$, and $T = 1500$ Nm 54
Figure 4-9. Feedforward optimal torque distributor architecture 66
Figure 4-10. Driver Input for slalom on wet road: (a) steering wheel angle, (b) total torque 69
Figure 4-11. Optimal torque distribution to the front and rear axles for step steer scenario on dry road 69
Figure 4-12. Effect of optimal torque distribution on lateral acceleration ($\mu = 0.50$, $vx, 0 = 40$ km/h) 69
Figure 4-13. Torque distribution effect on sideslip angle, and yaw rate. ($\mu = 0.50$, $vx, 0 = 40$ km/h) 69
Figure 4-14. Torque distribution effect on vehicle trajectory. ($\mu = 0.50$, $vx, 0 = 40$ km/h) 70
Figure 4-15. Driver Input for double lane change on dry road: (a) steering wheel angle, (b) total torque 71
Figure 4-16. Optimal torque distribution to the front and rear axles for double lane change scenario on dry road 71
Figure 4-17. Effect of optimal torque distribution on lateral acceleration ($\mu = 0.50$, $vx, 0 = 40\ km/h$) 72
Figure 4-18. Torque distribution effect on sideslip angle, and yaw rate. ($\mu = 0.50$, $vx, 0 = 40\ km/h$) 72
Figure 4-19. Torque distribution effect on sideslip angle, and yaw rate. ($\mu = 0.50$, $vx, 0 = 40\ km/h$) 72
Figure 4-20. Driver Input for double lane change on dry road: (a) steering wheel angle, (b) total torque 74
Figure 4-21. Optimal torque distribution to the front and rear axles for double lane change scenario on dry road 74
Figure 4-22. Effect of optimal torque distribution on lateral acceleration ($\mu = 0.85$, $vx, 0 = 40\ km/h$) 74

Figure 4-23. Torque distribution effect on sideslip angle, and yaw rate. ($\mu = 0.85$, $vx, 0 = 40\ km/h$) 74
Figure 4-24. Driver Input for acceleration in turn on dry road: (a) steering wheel angle, (b) total torque 77
Figure 4-25. Optimal torque distribution to the front and rear axles for acceleration in turn on dry road 77
Figure 4-26. Effect of optimal torque distribution on lateral acceleration 77
Figure 4-27. Torque distribution effect on sideslip angle, and yaw rate 77
Figure 4-28. Vehicle trajectory 78
Figure 4-29. Driver Input for lane change on wet road: (a) steering wheel angle, (b) total torque 79
Figure 4-30. Optimal torque distribution to the front and rear axles for lane change scenario on wet road 79
Figure 4-31. Effect of optimal torque distribution on lateral acceleration 80
Figure 4-32. Torque distribution effect on sideslip angle, and yaw rate. 80
Figure 4-33. Feedforward optimal torque distributor architecture 88
Figure 4-34. Driver Input for acceleration in turn on dry road: (a) steering wheel angle, (b) total torque 89
Figure 4-35. Optimal torque distribution to the front and rear axles for acceleration in turn on dry road 89
Figure 4-36. Effect of optimal torque distribution on lateral acceleration 90
Figure 4-37. Torque distribution effect on sideslip angle, and yaw rate 90
Figure 4-38. Vehicle trajectory 90
Figure 4-39. Tires normal load when feedforward is ON 91
Figure 4-40. Tires normal load when feedforward is OFF 91
Figure 4-41. Wheel speeds when feedforward is ON 92
Figure 4-42. Wheel speeds when feedforward is OFF 92
Figure 4-43. Driver Input for lane change on wet road: (a) steering wheel angle, (b) total torque 93
Figure 4-44. Optimal torque distribution to the front and rear axles for lane change scenario on wet road 93
Figure 4-45. Effect of optimal torque distribution on lateral acceleration 93

Figure 4-46. Torque distribution effect on sideslip angle, and yaw rate. 93
Figure 4-47. Vehicle trajectory 94
Figure 5-1. Schematic model of the vehicle with active aerodynamic wings at the front and rear of the vehicle 97
Figure 5-2. Tire lateral force under various normal loads 98
Figure 5-3. Schematic model of the feedforward-feedback MPC controller for active aerodynamic system 101
Figure 5-4. Driver's steering and torque inputs 111
Figure 5-5. Front and rear normal loads created by the feedforward active aero controller 111
Figure 5-6. Front-left tire capacity in force generation 112
Figure 5-7. Front-right tire capacity in force generation 112
Figure 5-8. Rear-left tire capacity in force generation 113
Figure 5-9. Rear-right tire capacity in force generation 113
Figure 5-10. Front and rear tires' slip ratio 113
Figure 5-11. Driver's steering and torque inputs 115
Figure 5-12. Front and rear normal loads created by the feedforward active aero controller 115
Figure 5-13. Vehicle response with and without Active Aero system: (a) longitudinal speed, (b) side slip angle, (c) yaw rate 115
Figure 5-14. Front and rear normal loads created by the feedforward-feedback active aero controller 115
Figure 5-15. Vehicle response with and without feedforward controller: (a) longitudinal speed, (b) side slip angle, (c) yaw rate 116
Figure 5-16. Front and rear normal loads created by the feedback active aero controller 116
Figure 6-1. Schematic model of the vehicle with active aerodynamic wings at the front and rear of the vehicle 128
Figure 6-2. Driver Input for slalom on dry road: (a) steering wheel angle, (b) total torque. 130
Figure 6-3. State response of the vehicle: (a) longitudinal speed, (b) side slip angle, (c) yaw rate .. 130
Figure 6-4. Optimal normal loads generated by front and rear aero surfaces 130
Figure 6-5. Optimal torque command sent to each electric motors 130

Figure 6-6. Driver Input for turn in acceleration on dry road: (a) steering wheel angle, (b) total torque 132
Figure 6-7. Dynamic responses of the vehicle: (a) longitudinal speed, (b) side slip angle, (c) yaw rate 132
Figure 6-8. Optimal normal loads generated by front and rear aero surfaces 133
Figure 6-9. Optimal torque command sent to each electric motors 133
Figure 6-10. Driver Input for turn in acceleration on wet road: (a) steering wheel angle, (b) total torque 134
Figure 6-11. State response of the vehicle: (a) longitudinal speed, (b) side slip angle, (c) yaw rate 134
Figure 6-12. Optimal normal loads generated by front and rear aero surfaces 134
Figure 6-13. Optimal torque command sent to each electric motors 134

List of Tables

Table 3-1. Physical parameters of the vehicle used for open-loop simulation.....36

Table 4-1. Physical parameters of the vehicle used for CarSim® simulations 67

Table 5-1. Aerodynamic characteristic of aero surface at different angles of attack [62].....100

Nomenclatures

A	Vehicle frontal area
A_i	Frontal area of the front/rear aero surface
AWD	All Wheel Drive
$\vec{a}_{inertial}$	Vehicle inertial acceleration
a_x	Longitudinal acceleration
$a_{x,lim}$	Limit of longitudinal acceleration
$a_{x,max}$	Maximum Longitudinal Acceleration
$a_{y,lim}$	Limit of lateral acceleration
$a_{y,max}$	Maximum lateral acceleration
C	Short form of cos function
C_d	Drag force coefficient
C_x	Drag coefficient
C_z	Lift coefficient
C_α	Tire cornering stiffness
$C_{\alpha f}$	Front cornering stiffness
$C_{\alpha r}$	Rear cornering stiffness
$\bar{C}_{\alpha ij}$	Cornering stiffness at operating point
CG	Vehicle Center of Gravity
d	Vehicle track length
F_{aero}	Aerodynamic forces acting on vehicle's body

F_x	Longitudinal tire force
F_x^{req}	Driver's requested longitudinal force
F_{xf}	Longitudinal force of the front axle
F_{xij}	Tire longitudinal force at each corner
F_{xr}	Longitudinal force of the rear axle
F_{xfr}	The front-right tire longitudinal force
F_{xfl}	The front-left tire longitudinal force
F_{xrr}	The rear-right tire longitudinal force
F_{xrl}	The rear-left tire longitudinal force
F_y	Lateral tire force
F_{yf}	Lateral force of the front axle
F_{yfr}	The front-right tire lateral force
F_{yfl}	The front-left tire lateral force
$F_{yf,lim}$	Limit of the front axle lateral force
$F_{yfl,lim}$	Limit of the front-left tire lateral force
$F_{yfr,lim}$	Limit of the front-right tire lateral force
F_{yij}	Tire lateral force at each corner
$\bar{F}_{yij}$	Tire's lateral forces at the operating point
F_{yr}	Lateral force of the rear axle
F_{yrl}	The rear-left tire lateral force
$F_{yr,lim}$	Limit of the rear axle lateral force
$F_{yrr,lim}$	Limit of the rear-right tire lateral force

$F_{yrl,lim}$	Limit of the rear-left tire lateral force
F_z	Normal tire force
F_z^{+AA}	Tire normal load with active-aero effect
F_z^{req}	Requested normal load
F_z^{est}	Estimated normal load
F_{za}^{est}	Estimated aero normal load
F_{zaf}	Front Active-aero normal force
F_{zar}	Rear active-aero normal force
F_{zai}^{max}	Maximum normal force of the active-aero surface
F_{zf}	Normal load acting on front axle
F_{zij}	Tire normal loads at each corner of the vehicle
F_{zr}	Normal load acting on rear axle
FWD	Front Wheel Drive
g	Gravitational acceleration
h	CG height
I_z	Vehicle yaw inertia
k_{us}	Understeer coefficient
l	Distance of the front axle to the rear axle
l_{af}	Distance of front active-aero to the front axle
l_{ar}	Distance of rear active-aero to the rear axle
l_f	Distance from CG to the front axle
l_r	Distance from CG to the rear axle

M_z	Vehicle Yaw moment
$M_{z,lim}$	Limit of the yaw moment of the vehicle
MPC	Model Predictive Controller
m	Vehicle mass
N_p	Number of prediction horizon
R	Radius of the vehicle path
R_{eff}	Effective tire radius
RWD	Rear Wheel Drive
r	Vehicle yaw rate
$\vec{r}$	Vehicle linear displacement
$\dot{\vec{r}}$	Vehicle linear velocity
$\ddot{\vec{r}}$	Vehicle linear acceleration
r_{des}	Desired yaw rate
$r_{max,ss}$	Maximum steady-state yaw rate
$r_{min,ss}$	Minimum steady-state yaw rate
S	Short from of sin function
T	Total torque input
T_f	Front axle torque
$\bar{T}_f$	Front axle torque at operating point
T_{fl}	Torque of the front-left tire
T_{fr}	Torque of the front-right tire
T_r	Rear axle torque

$\bar{T}_r$	Rear axle torque at the operating point
T_{rl}	Torque of the rear-left tire
T_{rr}	Torque of the rear-right tire
T_s	Time step of discretization
t	Time
$\vec{v}_{inertial}$	Vehicle inertial velocity
v_x	Vehicle longitudinal velocity
v_{x0}	Initial longitudinal speed
v_y	Vehicle lateral velocity
v_z	Vehicle vertical velocity

Greek Nomenclatures

α	Tire sideslip angle
α_{ij}	Tire sideslip angle at each corner
$\bar{\alpha}_{ij}$	Corner tire sideslip angle at the operating point
α_{lim}	Tire sideslip angle at the friction limit
α_z	Active-aero surface's angle of attack
α_{zi}^{max}	Maximum active-aero surface angle of attack
α_{zi}^{min}	Minimum active-aero surface angle of attack
β	Vehicle sideslip angle
β_{des}	Desired sideslip angle
β_{max}	Maximum sideslip angle

β_{min}	Minimum sideslip angle
θ_r	Road grade angle
μ	Road friction coefficient
ρ	Air mass density
τ	Electric motor time delay
τ_z	Active-aero surface time delay
ϕ_r	Road bank angle
ψ	Vehicle yaw angle
$\vec{\Omega}$	Vehicle angular velocity
$\dot{\vec{\Omega}}$	Vehicle angular acceleration
ω_x	Vehicle angular velocity around x axis
ω_y	Vehicle angular velocity around y axis
ω_z	Vehicle angular velocity around z axis

Chapter 1
Introduction

Professional drivers have the skills of controlling performance vehicles at the limits of handling by simultaneously using available actuators such as drive/brake torque, steering, active aerodynamics, etc. However, not all drivers are capable enough of using available tools manually at the right time and with the right magnitude. As vehicle control systems are getting smarter, they can either decide instead of the drivers (autonomous vehicles) or adjust the drivers' command (driver assistant systems) to prevent the vehicle from losing stability in dangerous situations or caused by human errors. This has brought the idea of using integrated controllers to improve vehicle handling and stability through various control modules. One of the most common control approaches is torque vectoring which is widely used in current vehicles. Torque distribution in both forms of brake or traction is highly effective in yaw tracking of the vehicle. Since the capability of using torque distribution depends directly on the tires' force generation capacity, adding actuators such as an aerodynamic system that can improve tires' capacity in force generation is of high interest especially in sports cars.

1.1. Motivations

In the past decade, researchers have tried to design integrated controllers by bringing all available control actuators under one control system. Indeed, a big challenge for control engineers is to design an integrated controller with the capability of utilizing the best set of control actuators with optimal actuation magnitudes at any time. Designing such an integrated controller at the limits of handling requires depth knowledge of dynamics and limitations of both vehicle and actuators. It is essential to know the exact effect of each actuator on the vehicle dynamics at any given time to be able to use it optimally on the vehicle.

A vehicle reaches its limits of handling when tires are generating their maximum forces in longitudinal and/or lateral directions. The friction forces available at the contact patch between the tire and ground limit the maximum force that a tire can generate. Tire capacity in force generation also depends highly on the downforces acting on each tire. It is known that the normal forces at each corner of the vehicle change due to the lateral and longitudinal load transfers. In cases that the vehicle is equipped with front/rear aerodynamic surfaces or active aerodynamic systems, the tire normal loads vary with vehicle speed, winds speed, angle of the aero surfaces, etc. Therefore, all these parameters make it too complex to detect maximum tire capacity. This means that defining a set of actuators to guarantee vehicle stability in a harsh situation is highly complex and requires deep knowledge of vehicle system dynamics.

A useful index to detect whether a tire has reached its limits of handling is the tire slip ratio. Tire slip ratio provides good insights about each tire condition and its capacity in force generation. Figure 1-1 shows the tire forces in longitudinal and lateral directions with respect to the slip ratio and tire slip angle. It can be seen that at the slip ratio of around 10% the tire is at its highest force generation capacity. This would allow us to define a range for the vehicle handling limits and use it as a powerful tool to either push the vehicle to this range whenever it is necessary or use available actuators to get the desired response while keeping the vehicle at this range.

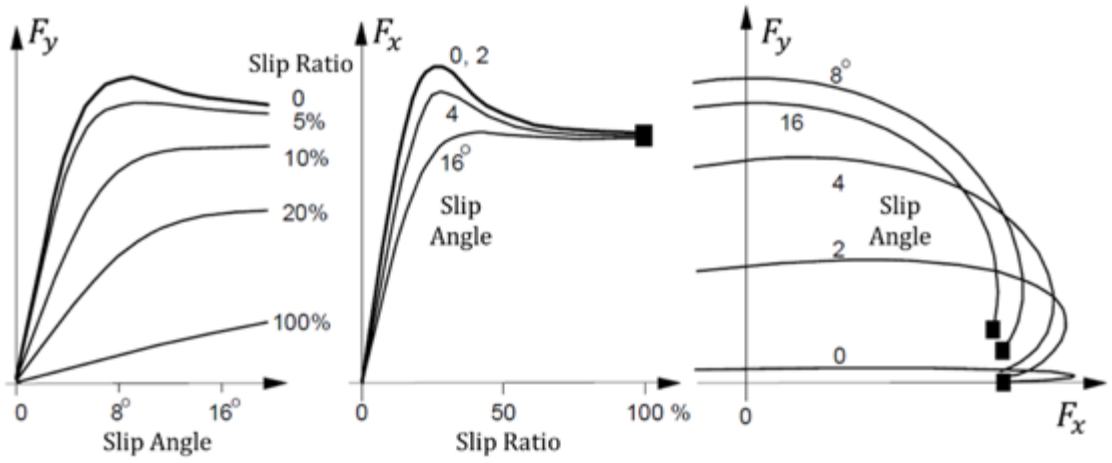

Figure 1-1. Tire Forces with respect to tire slip ratio and slip angle [1]

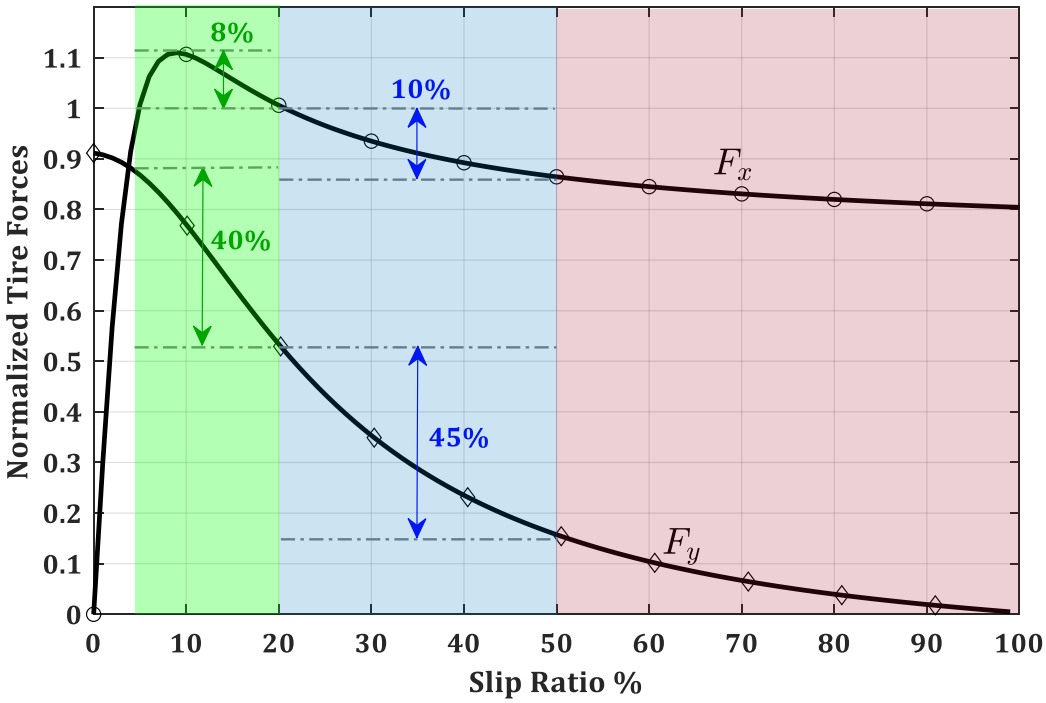

Figure 1-2. Effect of slip ratio on tire capacity.

Figure 1-2 represents the lateral and longitudinal tire forces as functions of the longitudinal slip ratio. As mentioned before, at the slip ratio around 10%, the tire reaches its maximum capacity. An interesting point is that while the slip ratio is in the range of 5 to 20% (green zone), by making small changes in longitudinal force (maximum change of 8%), the vehicle lateral grip which is a function of the lateral forces, can change by 40%. Increasing available lateral grip through maximizing the tire lateral forces would have a huge impact on vehicle handling and stability. In higher ranges of the slip ratio (blue zone), the slip ratio varies between 20 to 50%. Whenever a tire enters this range of slip ratio, the tire lateral capacity will drastically decrease, and hence, can saturate the tire and make the vehicle performance unstable.

Detecting tires' maximum capacity and the vehicle limits of handling are not the only challenges in vehicle control and stability problems. Another challenge is to know the exact effect of actuators on vehicle state at different driving conditions. In addition, when the vehicle is at its limits of handling the problem becomes even more challenging due to the nonlinear behavior of tires in the saturation zone.

The main driver inputs namely steering angle and drive/brake torque would be the key sources for the lateral and longitudinal tire force generations. Therefore, the drive/brake torque fed into the vehicle and more importantly, the distribution of the torque on each wheel has a significant effect on the tires' force generation and vehicle dynamics behavior at the limits of handling. Torque distribution strategy varies depends on the type of vehicle drivetrain configuration. The total drive torque is sent to the front axle in a Front Wheel Drive (FWD) configuration, or it is sent to the rear axle in a Rear Wheel Drive (RWD). It can also be distributed by a ratio to both front and rear axles, All Wheel Drive (AWD) configuration. Since the amount of torque applied to each wheel can significantly affect the slip ratio and longitudinal tire forces, controlling the torque sent to each corner can be very effective in maximizing vehicle handling capacity.

1.2. Objectives

The main objective of this thesis is to develop an integrated control system for performance vehicles equipped with independent electric hub motors in each wheel and active aerodynamic surfaces to maximize stability and maneuverability through an optimal torque distribution and control of aerodynamic systems. To achieve the main objective, a set of sub-objectives are defined and achieved at each step to fulfill the main objective. First, equations of motion of a vehicle moving on road with bank and grade angles are derived. The road angles are considered in the dynamic equations and can be easily replaced by traditional vehicle dynamic models in future works. Next, a thorough dynamic analysis is performed to investigate the torque distribution effect on the main states of the vehicle. Phase portraits of sideslip angle and yaw rate of the vehicle are used as the main tool to find the effect of actuators on the vehicle nonlinear dynamics. The open-loop dynamic analysis performed by phase portraits illustrates the control actions effects and can lead us to find the optimum control actions which would let the vehicle to use its maximum capacities in both longitudinal and lateral directions. Having the opportunity to use the maximum grip of the vehicle would be highly beneficial to prevent it from getting unstable and increase vehicle stability in dangerous situations. The stability criteria of the vehicle are also defined by the phase portraits of the vehicle. The stability boundaries are found based on the envelope control theory and presented on 2-D phase portraits. The 2-D phase portraits would give full insight into the actuator's impact on the main states of the vehicle. This will give control

engineers the required information for the selection of control actions to bring an unstable vehicle back to a stable region. Investigating the effects of optimal torque distribution on the phase portraits and the vehicle stability envelope is another objective of this study.

As the vehicle is being driven at the limits of handling, the drive torque applied to each tire has a direct impact on the slip ratio. Since the longitudinal slip would affect tire capacity in lateral force generation, preventing the tires from getting into the states of high slip ratio and keeping them with the highest rate of lateral force generation would be another important objective in this study. This objective will be fulfilled by developing an algorithm that receives the driver's inputs, steering angle, and drive/brake torque, and would decide about the optimal torque distribution that results in having the maximum longitudinal and lateral grip. The actuators involve in this algorithm would be four electric motors at each corner.

As mentioned, the main objective of this dissertation is to design and evaluate an integrated multi-actuation constrained control system, which can enhance vehicle stability and maneuverability during high-speed maneuvers. The actuations involved in this control structure are four independent electric motors and two aerodynamic surfaces at the front and rear of the vehicle. The proposed algorithms are evaluated first in the CarSim® simulation environment and eventually on the test vehicles available at the Mechatronic Vehicle Systems lab.

1.3. Thesis Outline

In the second chapter of this thesis, available literature on vehicle dynamics and control at the handling limits with various actuation systems are reviewed and summarized. The available methods of dynamic analysis at the limits of handling with the focus of torque distribution are studied. Different approaches to optimal torque distribution for electric vehicles are explored. Active aerodynamic systems (active aero surfaces) are studied and available control strategies for defining optimal aero surfaces' angles are reviewed. Constrained multi-actuator systems and their control structures with yaw tracking and stability objectives are explored and summarized in this chapter.

The third chapter focuses on the dynamic modeling of a vehicle moving on a road with bank and grade angles. This chapter presents the dynamic equations of motion of the vehicle and validation

results of the proposed model. Nonlinear tire models available in the literature are also explored in this chapter and the tire model used in the thesis is introduced in this chapter.

The fourth chapter studies the optimal torque distribution to achieve maximum lateral grip. This chapter includes dynamic analysis based on the phase portrait method. The torque distribution effect on open-loop dynamics and the safe envelopes are investigated in this chapter. Inspired by the dynamic square method, axial-based and wheel-based optimal torque distribution algorithms are developed with the objective of maximizing vehicle lateral grip. Two feedforward optimal torque distribution controllers are designed and evaluated by simulations and experimental studies in this chapter.

In Chapter 5, a control structure is developed to control the active aerodynamic system. Two aerodynamic surfaces are added to the front and rear of the vehicle as the main actuators in this chapter. A feedforward controller and an MPC feedback controller are designed to optimally find the control actions for the objective of yaw tracking. The deigned controller is evaluated in the CarSim high fidelity model.

Chapter 6 presents the integration of the optimal torque distribution control and active aerodynamic control presented in Chapters 4 and 5. A multi-actuator highly constrained MPC controller is designed in this section. The objective of this controller is tracking the desired yaw rate and stabilizing the vehicle by defining stability constraints for the optimization problem. A high-level constraint adjustment module is developed and added to the control structure to observe and adjust actuators' constraints to maximize the controller performance and minimize cost and energy by activating/deactivating the actuators. The proposed controller is simulated and verified in the CarSim simulation environment.

In Chapter 7, the conclusions and contributions of this thesis are summarized. The potential works that can be investigated in the future based on this dissertation are also listed.

Chapter 2
Literature Review and Background

In this chapter, a literature review is performed on vehicle dynamics and control at the limits of handling. The first section of this chapter reviews the available works on the methods of dynamic analysis for a vehicle at its handling limits. Then control strategies for optimal torque distribution and active aerodynamic system are studied. Control strategies for constrained multi-actuator systems are also reviewed. The last section is devoted to the road angles estimation. Although road angle estimation is not part of this dissertation, the lack of dynamic modeling of a vehicle moving on a road with bank and grade angles in the literature, brought the idea of reviewing available studies on vehicles moving on banked or inclined surfaces to understand various approaches for including road angles in dynamic modeling and analysis.

2.1. Vehicle Dynamics at the Limits of Handling

When a vehicle reaches its friction limits, vehicle handling can be highly critical and any small miscalculation in control actions from the controller perspective can lead to a catastrophic incident. When it comes to driving a vehicle at its limits of handling, race car drivers have enough skill to keep the vehicle stable. But when it comes to ordinary drivers or autonomous vehicles, the controller's capacity in handling the situation at the friction limits is of the highest priority [2]. To translate the racecar drivers' skills into a control system, the vehicle dynamics at the friction limit must be carefully rooted in the vehicle control system. Since the vehicle dynamics at the limits of handling is highly nonlinear and function of many different parameters, to decrease the complexity of its concept, graphical methods such as "g-g" diagram, Dynamic Square, and phase portrait diagrams are being used

to give a better insight about it to control engineering researchers. Each of these methods is explained in the following sections.

2.1.1. “g-g” Diagram

One of the most popular methods for designing a controller that can operate at the limits of handling is using the “g-g” diagram [3]–[5]. “g-g “diagram graphically relates the vehicle maximum capacities in force generation with the driver’s actions, road conditions and vehicle dynamics behavior [6]. This method plots the longitudinal acceleration on the vertical axis against the lateral accelerations on the horizontal axis. The border of the “g-g” diagram represents the friction limits of the vehicle. Figure 2-1 shows a “g-g” diagram plotted using real test data of a Formula SAE race car while it had been driven at the limits of handling on the race track [7].

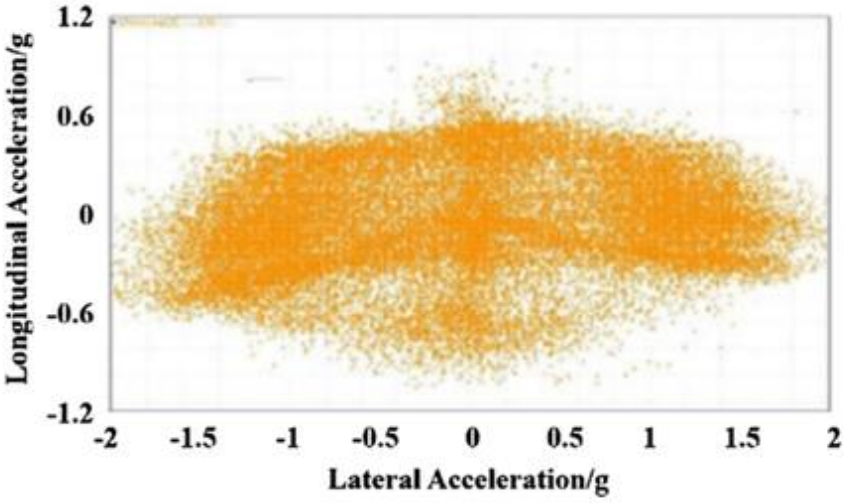

Figure 2-1. Formula SAE racecar g-g diagram at the limits of handling [7]

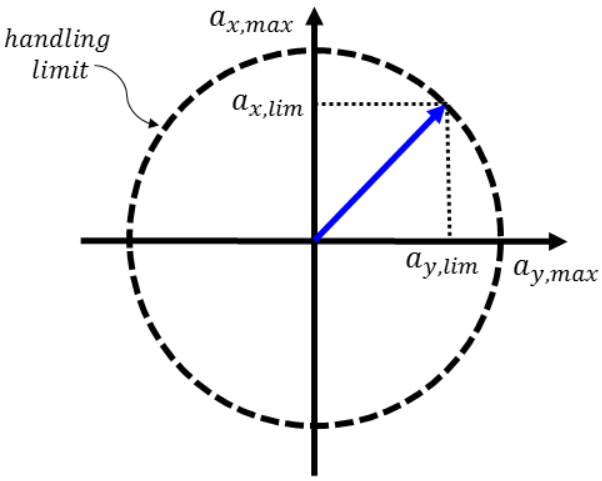

Figure 2-2. Circle model of "g-g" diagram for vehicle limit handling

Many research developments have been founded based on the "g-g" diagram [8]–[11]. However, due to the complexities of the vehicle dynamics at the limits of handling, instead of using an oval model of the "g-g" diagram, a simplified circle version of it has been replaced in many of these researches, see Figure 2-2.

For designing a feedforward longitudinal controller for an autonomous vehicle that could drive the vehicle to its limit of handling during a cornering maneuver, Kritayakirana and Gerdes [8] used the "g-g" diagram. The designed feedforward controller estimated the required brake or throttle command to perform a cornering maneuver on a clothoid map in the same way that a professional race car driver could do it. Knowing the mathematical characteristic of the clothoid track would provide the required information to the controller for finding the lateral acceleration, which is a function of path curvature. When the controller receives the lateral acceleration measurement, the knowledge of the friction limits coming from the "g-g" diagram would let the controller estimate the brake\throttle command to have the desired longitudinal acceleration. Having the desired lateral acceleration combined with an appropriate steering command resulted in tracking the path at the limits of handling.

A dynamic controller consist of longitudinal and lateral controllers was designed by Ni and Hu [7]. The proposed controller was capable of tracking the desired path at the limits of handling. They obtained the driving limits of the vehicle by using the "g-g" diagram, which was obtained from the

phase portrait approach. They also used an estimator and feedback controller to minimize the uncertainties and disturbances due to the road friction condition and tire cornering stiffness. To do so, they estimated the maximum road friction and adjusted the "g-g" diagram with respect to the estimated friction coefficient by getting feedback from the motor torque and wheel speed. They validated the proposed controller by applying it on an autonomous vehicle being driven on an oval race track [7].

2.1.2. Dynamic Square

Although the "g-g" diagram is easy to understand, it just provides information regarding the friction limits and the lateral and longitudinal accelerations. Therefore, it worth introducing the Dynamic Square method which has been developed after the "g-g" diagram by Matsuo et al. [12]. This method plots nominal values of the front and rear axle forces based on the available lateral and longitudinal accelerations. Indeed, the "g-g" diagram is part of the dynamic square [13].

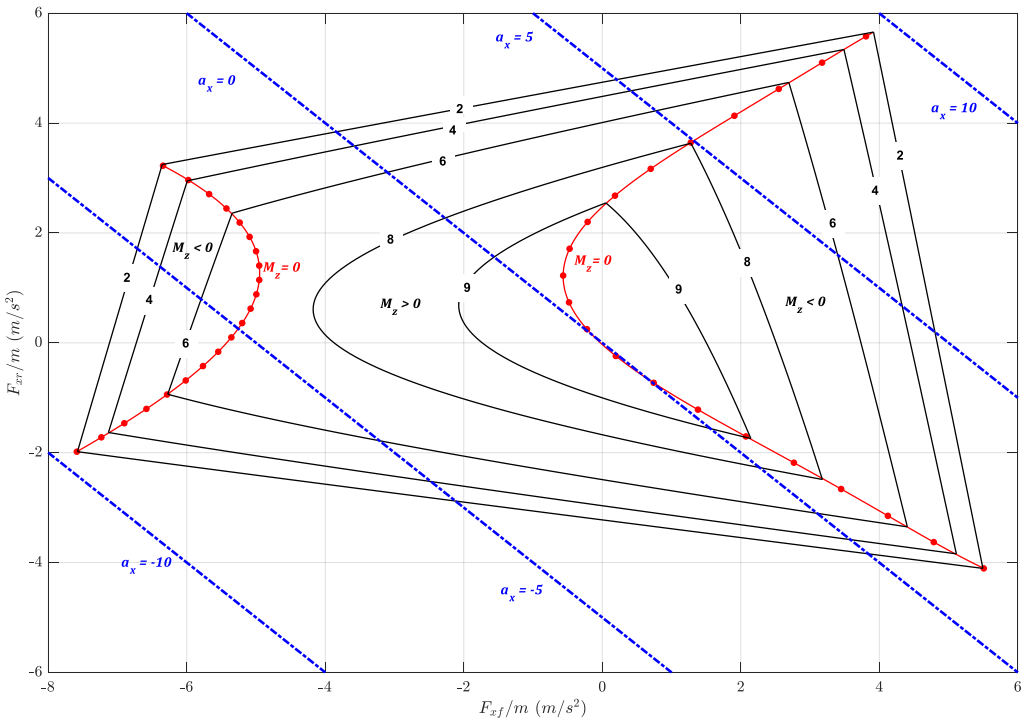

Figure 2-3. Dynamic square

Figure 2-3 shows a dynamic square plotted for a vehicle with oversteer behavior. In a Dynamic Square, each quadrilateral belongs to a specific amount of lateral acceleration, and as the available lateral acceleration increases, the related quadrilateral shrinks to a smaller size compared to the ones belong to lower lateral accelerations. The iso-curves in the middle area of the dynamic square represent the force distributions to the front and rear axles which result in the oversteering behavior of the vehicle. This is when the front axle saturates before the rear axle. Along the sides of the quadrilaterals, the vehicle behavior is understeer, i.e. the rear axle saturates before the front axle. At the vertices, both axles saturate simultaneously which makes the vehicle behavior neutral. The method of the dynamic square has been used in few numbers of researches during the last years [9], [14]–[16]. Among the referred researchers, Matthijs Klomp, Kaoru Sawase, and Yoshiaki Sano can be named as the main authors who have applied the dynamic square method in their research. They all have used the dynamic square method to develop algorithms, which distribute the torque optimally to the axles\corners to maximize the lateral grip and stability during harsh cornering. The dynamic square method is the main inspiration in this dissertation and will be explained in more detail in Chapter 4.

2.1.3. Friction Estimation at the Limits of Handling

In preparation for developing an algorithm, which can push the vehicle into the friction limits, first, the friction coefficient between the tire and the road surface must be known. There are various methods for estimating the road\tire friction coefficient. The available literature on the road\tire friction estimation reveals that there are two main categories in this field: a) estimation of average friction coefficient which assumes all tires have the same friction coefficients, and b) estimation of tire friction coefficients individually [17]. Although in normal situations all tires are subjected to the same road conditions, there happen cases in which, tires may face different road conditions where if the average friction estimation is being calculated, it may cause errors in the controller's performance and create dangerous situations. Therefore, it is highly recommended to use an individual friction estimation at each corner of the vehicle. To estimate the friction coefficient, researchers can either follow approaches that measure longitudinal dynamics or approaches which measure lateral dynamics of the system [18].

In a study performed by Rajmani et al. [19], tire friction is being estimated through three different algorithms depends on the available sensors. All algorithms are based on the longitudinal slip

calculation. In their method, first, the longitudinal forces on each tire are estimated, then the slip ratio will be calculated for each wheel independently, and finally, by using a least-square parameter identification the road\tire friction coefficient is estimated. The authors have reported the evaluations of their algorithm both on CarSim® and on a Volvo XC90 sport car and showed that it could reliably estimate the road friction coefficient.

Hsu et al. [20] have used steering torque to measure aligning moment and estimate road\tire friction coefficient. Aligning moment change significantly just before the tires reach their maximum capacity, and can be detected from steering torque available through steer-by-wire or electric power steering systems. In the model presented by Hsu et al. [20] information derived from steering torque has been used to estimate the tire sideslip angle. Having the tire sideslip angle would lead to the friction limits in the lateral direction. In their modeling, the sensitivity of the tire trail to the tire parameters has played an important role in the early detection of maximum lateral forces before tire saturation happens.

2.2. Vehicle Stability Analysis Based on Phase Portrait Approach

A phase portrait diagram plots the sideslip angle and yaw rate of the vehicle against each other. A phase portrait diagram provides significant information for analyzing nonlinear dynamics systems. Each point of a phase portrait represents the magnitude and direction of the vehicle steady-state responses for sideslip angle and yaw rate. The phase portrait also reveals the location of the equilibrium points of the vehicle dynamic system [21]. Based on the type (stable or saddle) and the location of the equilibrium points, vehicle dynamic behavior at different regions of the phase portrait can be studied.

Figure 2-4 shows a phase portrait obtained from an open-loop dynamic analysis based on a planner vehicle model. The circles represent the equilibrium points which can lead to defining the stable (white) and unstable (gray) regions of the vehicle performance and would be highly beneficial for designing a controller. There is wealthy literature on using phase portrait diagram for designing stability controllers [22]–[27].

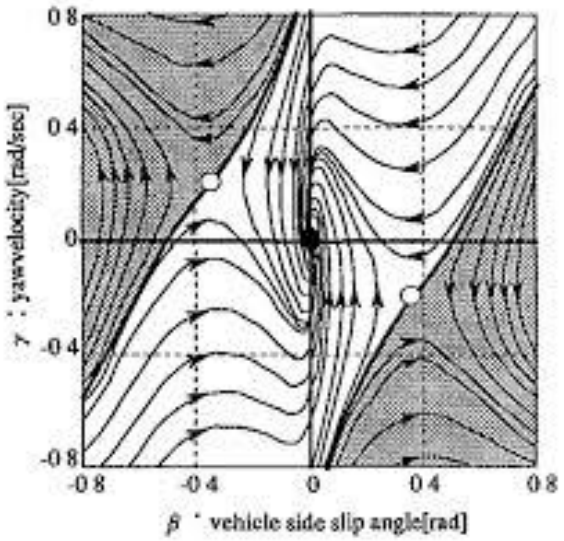

Figure 2-4. Phase portrait of a planner vehicle model with no steering angle effect [28]

Inspired by the phase portrait diagram a safe envelope has been defined where inside its boundaries the vehicle is said to be stable [29], see Figure 2-5. To guarantee that the vehicle is stable, it is necessary to define the vehicle stability region for the control system and make sure the vehicle is always within the boundaries of the stable region. If a vehicle goes out of the safe boundaries, the controller should be able to bring it back to the safe zone as fast as possible [30].

The stable envelope is defined based on the steady-state values of the vehicle yaw rate and sideslip angle. As long as the vehicle is inside the safe envelope it can be assured that it won't spin and remains stable. It should be noted that since the boundaries of the stable envelope are defined based on the steady-state analysis, it is possible to be outside of the boundaries and remains stable. In such situations, the vehicle will go back to the stable region within a short time. It was suggested by Brown et al. [31] that there could be a larger stable envelope that is yet under investigation.

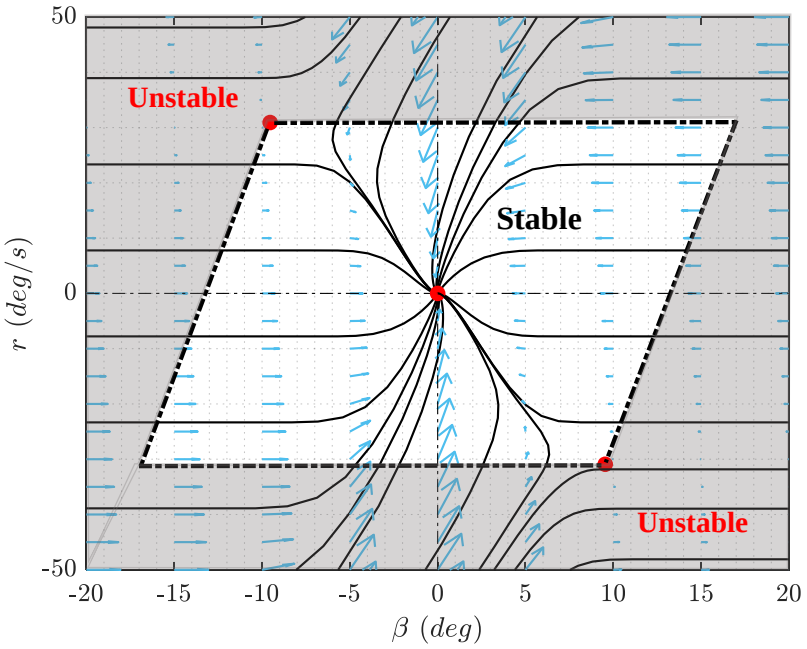

Figure 2-5. A stability envelope that divides stable and unstable regions

As soon as a vehicle goes outside the stable region, it must turn back to the safe envelope as fast as possible. Depends on the state values and vehicle dynamics, it may require various control actions to be applied to bring it back to the safe region. However, the main question is which control action and with what actuation value must be used to bring the vehicle back as fast as possible. This question may rise not only for stability purposes but also for reaching any other control resolutions. Bobier and Gerdes [32] developed a high-performance sliding surface control with a low computational effort that could stabilize the vehicle y keeping it inside the safe envelope. They defined the boundaries of their safe envelope based on the yaw acceleration null-cline. They designed their controller in a way that driver has full control over the vehicle. While, when the vehicle states are outside of the safe envelope, the controller adjusts the control actions to minimize the distance between measured states and the boundaries of the safe envelope. Brown et al. [31] used a phase portrait to develop safe envelopes for stability and obstacle avoidance. By integrating the two controllers, one for path planning and the other for path tracking, they could safely deviate from the desired path within the safe envelope. They implemented the envelope control in a model predictive structure and evaluated their controller experimentally. They could successfully track the desired path even when the vehicle was outside of

the stability safe envelope. Erlien et al. [33] developed a shared control structure to perform obstacle avoidance while stabilizing the vehicle using two different safe envelopes. One of their envelopes limited the boundaries of the tracking line and obstacles, and the other one limited the vehicle states to assure vehicle stability. They successfully tackled the nonconvex nature of the optimal controller by breaking it into a set of convex problems. They evaluated their proposed method by experimental tests. Bobier et al. [34] utilized the phase portrait to integrate the open-loop dynamics into the yaw rate and sideslip angle stable boundaries. They studied the effect of steering and braking as their main control actions on the open-loop dynamics through the phase portrait technique. They implemented the results of their investigation on a sliding surface controller to stabilize the vehicle during drift maneuver. They used the iso-clines and null-clines of the open-loop dynamics to locate the equilibrium points. They studied the effect of the steering and braking commands on the iso-clines and null-clines to have better insight on the control action effect on the drift equilibrium points. They mixed the phase portraits outputs for the extreme cases of each control action to be able to have an integrated form of logics for finding the location of equilibrium points under simultaneous effect of both control actions.

As an extension of the two dimensional (yaw rate - side slip angle) phase portrait, a three-dimensional phase portrait including longitudinal velocity was studied by Beal and Boyd [35]. The 3-D phase portrait would allow investigating the effect of combined longitudinal and lateral tire forces under the applied control actions. The outputs of this approach would make it possible for the control designer to check both state trajectories and system stability of a complex nonlinear system. Each of the trajectories shown in Figure 2-6 represents the steady-state responses of the vehicle starting from initial conditions shown as circles and under the effect of -5% wheel slip braking and 5° of the steering angle of the front tires. Initial conditions covered in this figure are those that happen mainly during harsh maneuvers. The stars represent the equilibrium points which along together as the longitudinal speed changes, create an equilibrium string; All stable trajectories converge to this string [35]. Including longitudinal speed in the phase portrait let one study the nonlinear combined slip effect of the tire force generation using the 3-D phase portrait.

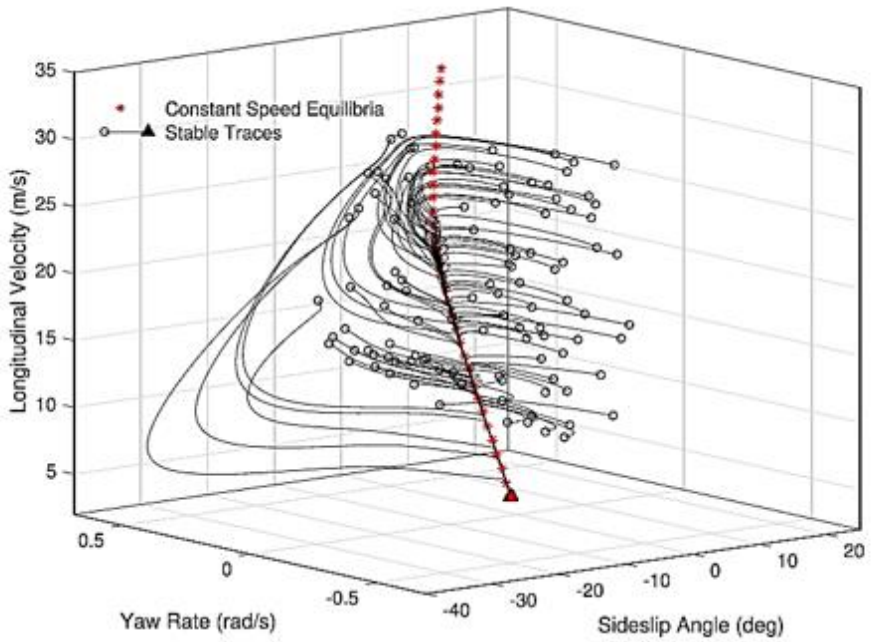

Figure 2-6. 3-D Phase portrait having steering and braking as control actions [35]

2.3. Vehicle Stability and Control with Torque Distribution Method

Torque distribution control or torque vectoring is known as an effective control method among the available control strategies. The main idea of this method is to directly control the yaw moment acting on the vehicle by transferring torque between the front and rear axles and\or left and right wheels. By this method, the vehicle can be stabilized during the cornering maneuver by changing the understeer characteristics of the vehicle and enhancing its steering response. This method has been commonly used in vehicles with electric motors due to the capability of having various torques at each corner of the vehicle [36]–[44]. Esmailzadeh et al. [45] modeled and analyzed the dynamics of an electric vehicle equipped with four motors. They studied the dynamics of the vehicle's motion, wheels, and electric motors. they also designed a yaw moment controller based on the developed model for the motorized wheels electric vehicle [46]. They designed an optimal controller to obtain desired yaw moment by distributing torque into corners. Their multilayer control system included a feedforward steering control

and a feedback yaw tracking control. Goodarzi et al. [47] designed a vehicle dynamic controller for stabilizing the vehicle by optimizing the external yaw moment. They designed a multi-layer control system which in the high-level could calculate the required traction force. In the middle level of the control structure, they used a fuzzy logic controller to control the traction force of each wheel independently. In the last layer, their control system targeted the slip ratio of the wheels. Cao et al. [48] designed an electric stability controller for an electric vehicle with four independent electric motors. They proposed a two-layer structure for their control system. The higher level assured vehicle stability by calculating the required yaw moment. The lower level of the controller distributed the yaw moment requested by the stability controller into each electric motor. They evaluated their controller on a CarSim model integrated with MATLAB Simulink. They assumed the vehicle is traveling straight on a split μ and can remain stable during critical moments when each wheel experiences a different friction coefficient. Zhai et al. [49] designed a stability controller based on a torque distribution algorithm. They used a fuzzy control with a look-up table for their fuzzy sets related to the tire parameters for calculating the tire lateral forces. They compared their algorithm with conventional torque distribution algorithms, which distributes torques evenly or just based on the normal loads' variations. They showed their optimal algorithm has a better stability performance. Her et al. [50] used torque distribution in the form of differential braking and front/rear traction to reach their desired values for longitudinal forces, yaw moment, and roll moment. In their yaw moment modeling, they used a linear tire model with constant values for cornering stiffness. Huang et al. [51] proposed an optimal torque distribution algorithm through a multi-objective optimization problem for an electric vehicle. The first objective of their multi-objective optimization was to detect the efficiency of the drive motor. The second objective was to optimally distribute the torque, and the third objective was to stabilize the vehicle. They used the line weighting method with adaptive weight to convert the last two objective functions into a multi-objective constrained optimization problem. They tackled their multi-objective optimization problem of torque distribution with the second-generation non-dominated sorting genetic algorithm and the hybrid genetic Tabu search algorithm. In another study performed by Lin et al. [52], a multi-objective optimal torque distribution strategy was developed for an electric vehicle with four electric motors. They tried to stabilize the vehicle through optimal torque distribution while maintaining the energy efficiency at its highest performance. They modeled the motor energy loss to develop an energy loss control allocation. To fulfill their second objective, they designed a hybrid model predictive controller to minimize the yaw tracking error. They evaluated their controller by implementing it on a dSPACE platform to

perform a lane change driving scenario and showed that the controller could improve the vehicle stability during the yaw tracking. Tahouni et al. [53] developed a novel control system by integrating active torque vectoring and electric stability controllers. They proposed a nonlinearly constrained controller with a nonlinear prediction model. By restricting the sideslip angle values in the optimization problem, they could enhance both the vehicle stability and steerability. They transformed the yaw moment requested by the controller into distributed drive/brake torque. They compared their achievements with a nonlinear unconstrained MPC with 14-DOF and showed a faster and more accurate solution can be achieved by just using constraints on sideslip angle. Alcantar and Assadian [54] designed a control system which could perform rear torque vectoring on a hybrid electric vehicle to optimize lateral tire forces. Their controller could improve the longitudinal performance of the vehicle while it prevents tries from saturation when driving on a low friction surface. They also enhanced the vehicle yaw tracking during high-speed double lane change maneuver by using a linear tire model for the lateral and longitudinal tire forces. To design the rear torque vectoring, they modeled the rear axle drive as a system with 6-DOF and integrated it with a 3-DOF vehicle dynamics. They tried to obtain minimum tire forces and minimize the yaw tracking error, simultaneously.

Although torque vectoring has been used in many research since 1996, the idea of finding the maximum available torque-vectoring was first introduced by Sawase and Ushiroda in 2008 [9]. They considered the vehicle handling limits to calculate the maximum possible torque vectoring, which would give the best cornering performance to the vehicle. To do so, they used the dynamic square, which was explained in previous sections to find the vehicle handling limits and also, the optimum torque distribution to the front and rear axles. As mentioned in section 2.1.2, the vertices of the quadrilaterals of each dynamic square represent the torque distribution, which saturates both the front and rear axles, simultaneously. As shown in Figure 2-7, following all vertices along with Dynamic Square of various lateral accelerations, the optimal front/rear torque distribution is shown by red line with circle markers.

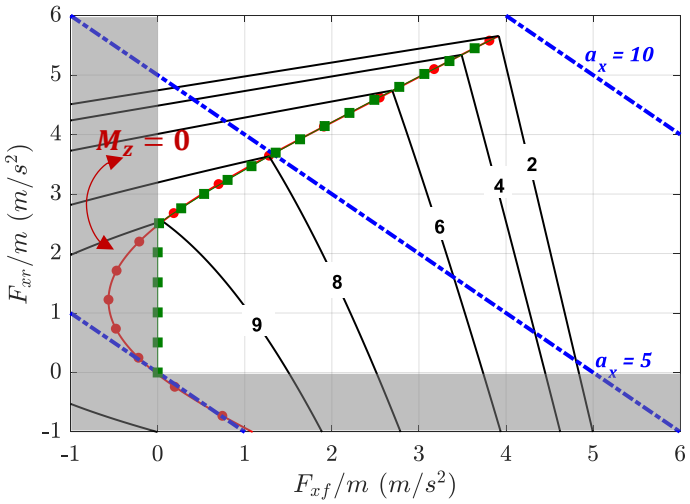

Figure 2-7. Optimal torque distribution based on Dynamic Square

In order to have the best cornering performance, the red line of $M_z = 0$ must be followed for the torque distribution to the front and rear axles. For the case of acceleration, the first quarter of the Dynamic Square must be considered and therefore, the optimal torque distribution would lie on the line that showed by the green line with square markers [13]. It should be noted that Dynamic Square shown in Figure 2-7 has been plotted without considering the effects of normal load transfers and the steering angle input. Therefore, the introduced optimal solution in [13] based on Dynamic Square is not feasible and must be enhanced to be capable of being applicable to a real car.

2.4. Vehicle Stability and Control with Active Aerodynamic Systems

Harvesting aerodynamics forces in favor of improving the handling performance of vehicles have been a very interesting topic for researchers, especially in racecar engineering. Tripled downforce generated by aerodynamic elements in race cars has increased their lateral accelerations up to 3g [55]. The first signs of using aerodynamic to increase vehicle performance appeared on formula one cars in 1968 by adding inverted wings on the front and rear axles [56]. Adding air wings brought a big improvement in cornering, accelerating, and braking performance of race cars. Since then optimization has been used to find the best shape, size, and coordination for the air wings to get the highest downforce

possible [57], [58]. Along with the advances in the vehicle industry, requirements for safety modules have increased, and car companies have been encouraged to use aerodynamic technologies such as active air wings as a safety module on their productions. Adding active aerodynamic wings to a system can compensate for the effect of lift forces caused by the airflow passing through the vehicle body. The extra downforce added through active aerodynamic system increases the available braking/traction capacity and enhances the handling and stability during maneuvers with high deceleration\acceleration [59]. In addition, during sharp maneuvers, the normal load transfers significantly reduce the inner wheels' normal loads. Adding active aerodynamic elements would balance the normal load distribution, which also leads to better traction or braking [60], [61]. The most commonly used aerodynamic elements are fixed spoilers, which are being used in vehicles to increase their performance by increasing the downforce acting on the vehicle. However, a fixed spoiler does not offer any control over the downforce [62]–[66]. An active aerodynamic system can adjust the angles of the front and rear spoilers based on the vehicle dynamics to have optimum values of downforce.

Corno et al. [67], [68] used aerodynamic wings for improving vehicle ride comfort. They used four aerodynamic surfaces to increase the ride quality by minimizing the sprung mass vibrations. They modeled the vehicle by a quarter-car model for their closed-loop controller and validated their model through high-speed simulations. They assumed the angle of the spoiler as the control input and the desired lift coefficient as the control output. They showed that by using the independent aerodynamic wings, the ride comfort improves by up to 30%. In 2014, an adaptive controller was designed and reported by Meder et al. [69] for the Porsche 911 Turbo. Their goal was to increase the downforce in the front axle by changing the front ramp angle around 2.5° to 10°, and reduce the lift on axles about 0.07 to -0.15. To do so, they designed an adaptive aerodynamic system that could be adjusted based on the driving conditions. To cover a wide range of driving scenarios, they defined three different zones for their aerodynamic control system. The tree zones were separated based on the vehicle longitudinal speed. The first zone covered the speed less than 80 km/h, the second zone covered speeds more than 120 km/h, and the third one included speeds over 270 km/h. In the first zone, all elements remained in their start position. In the second zone, the front wing is engaged automatically. The activation of the aerodynamic wings for zone three for the manual operation was designed and could either be started or stopped through a button in the front consul. The spoiler angle in their controller was forced to fixed angles in the third zone for safety reasons. Diba et al. [70] performed an investigation on the use of adjustable air wings on formula one cars. They applied their controller on a small size race car and

controlled the angle of attack on each spoiler separately to improve handling and stability. Their focus was on balancing the normal loads acting on the vehicle and compensating for the negative effect of the normal load transfers caused during high acceleration maneuvers. Ayyagari and He [71] studied the aerodynamic effect of the active rear spoiler. They performed CFD analysis as well as experimental tests in a wind tunnel. They designed a spoiler to improve the lateral stability of vehicles during driving scenarios with high speed and high accelerations. They studied the aerodynamics effect of rear spoiler during different angles of attack and different wind speeds. Chen et al [72] designed an integrated control system including differential braking and active aerodynamic elements. They assumed two air wings attached to the roof of the vehicle and each could be controlled separately. They used two control levels, the upper level included a sliding mode controller to track the desired yaw rate, and the lower level coordinated the aerodynamics control and differential braking control. They showed their designed controller improved the vehicle performance in yaw rate tracking. Ahangarnejad et al. [73] proposed a rule-base integrated controller consist of four different independent chassis control systems. They included an active aerodynamic control, torque vectoring control, active steering control, and the interconnected suspension control in their integrated chassis control system. The active aerodynamic control used in their control structure was based on the event-based lookup tables of required normal loads. They included the vehicle roll dynamic in their modeling but an important missing point in their formulation was to consider the lateral load transfers in their normal load estimations. Hammad [74] designed a sliding mode control system with the objective of yaw tracking and used active aerodynamic as its main control action. He used a lookup table to find required normal loads at each longitudinal speed. The active aerodynamic system he used included a set of inner wings and outer wings. He designed the controller in an event-base form with three different modes for each air wing sets.

2.5. Control and Stability of Multi-Actuation and Constrained Systems

To integrate active aerodynamic elements with different actuators such as active steering, differential braking, torque vectoring, etc., a control system must be capable of handling all nonlinearities and constraints of the system. A method for controlling high-constrained systems with multiple actuators is Model Predictive Controller (MPC). MPC is a well-known control structure for yaw tracking and stability purposes of multi-actuation constrained systems [75]–[80]. Li and Luo [81]

proposed an integrated control structure consist of a yaw tracking MPC and a speed tracking controller. They assumed five control actuators of steering angle and four corner torques. They assumed that the tire slip ratios and tire slip angles are small enough to model lateral tire forces linearly. They considered 3-DOF for their prediction model and developed a linear time-invariant MPC for yaw tracking purposes. They also designed a PID controller for speed tracking with the control actions of corner torques. In the end, they integrated the corner torques obtained from each controller to a unit set of control action and sent it to the vehicle. They validated their control structure performance in the CarSim simulation environment. Unfortunately, their report was deficient in explaining the integration of optimal control actions from each controller. Fnadi et al. [82] designed a constrained MPC for a rover to track the desired trajectory. The prediction horizon of their proposed MPC varied with respect to the rover longitudinal speed to assure enough prediction time. They modeled tire lateral force as a linear tire model, which is acceptable for the rover's tire with small sideslip angles. They defined stability constraints on the rover's sideslip angle and input constraints on the front and rear steering. They showed the importance of having stability constrained by comparing their results with an unconstrained LQR controller. Hashemi et al. [83] designed an MPC that included tire combined slip effects and force nonlinearities in the prediction model. They designed an MPC, which tracked the yaw rate and lateral velocity of the vehicle by optimizing the torque corners. They verified their controller on the low friction surface, experimentally. Yang et al. [84] modeled tire blow-up in extreme driving conditions and designed an MPC to stabilize the vehicle before and after a tire blow-up. They included stability and actuator increment constraints in their MPC structure. Their proposed MPC could track yaw moment and tires' longitudinal forces by redistributing the normal loads acting on the corners after a tire blow-up. Nahidi et al. [85] integrated lateral and longitudinal stability control systems. They used an MPC to find the required yaw moment and longitudinal forces at each corner. Then they incorporated a low-level controller to adjust torque corners according to the required forces obtained by the high-level MPC. Nah and Yim [86] enhanced the stability maneuverability of an electric vehicle by implementing a direct yaw moment multi-actuation control system. They assumed an electric vehicle with independent four-wheel braking, independent four-wheel drive, and independent four-wheel steering. They designed a controller to control total yaw moment created through each wheel brake/drive/steer in a way that the vehicle remained stable in all driving conditions. Zhang et al. [87] integrated yaw rate and side slip control with wheel slip control to enhance vehicle stability in longitudinal and lateral direction. They tried to combine their control objectives in MPC structure with

the control action of torque vectoring. They considered the nonlinearity of tire forces especially in lateral direction due to variation of tire slip ratios. They also considered the combined slip effect of tire on lateral and longitudinal forces by introducing a nonlinear tire model in their prediction model. They defined a linear parameter varying (LPV) MPC structure by linearizing their nonlinear prediction model at each time step. Their LPV-MPC could handle system stability with constraints as an online optimization problem. They claimed that their LPV-MPC could decrease computational time compared to the other LPV-MPCs available in literature.

2.6. Vehicle Dynamics on Non-Flat Road

In order to consider the road angles in the dynamic analysis, it is required to either have the road information in advance or to have an estimation module that can evaluate road properties online as accurately as possible. As mentioned before, considering the road angles in the control system would prevent the inaccurate performance of stability control actuators [88]. There are several types of research performed on road bank estimations. Boada et al. [89] developed an estimation method for vehicle parameters such as roll angle and road bank angles. Their method was a combination of a dual Kalman filter with a probability density function truncation method to consider the parameter physical limitations. Their method was based on the data they obtained from a real vehicle equipped with various types of sensors. Same as many other studies in this field [90]–[93], they faced the challenge of getting global information on the roll angle from sensors. The angle provided by these sensors is a combination of vehicle roll angle and road bank angle. Therefore, separation of the roll angle and road bank angle is a challenge that has been addressed and some solutions are proposed by researchers. Ryu and Gerdes [90] could successfully defeat this problem by developing a disturbance observer. They used the Global Positioning System (GPS) and Inertial Navigation System (INS) sensors to estimate the exact parameters of the vehicle model. Then, by developing a dynamic model that contained vehicle roll as state and road angle as disturbance, they could estimate the road angle by using the disturbance observer.

Chapter 3

Vehicle Dynamics Modeling on Non-flat Roads

In order to perform an accurate analysis of vehicle dynamics, a model that describes the vehicle states and its surrounding interactions is highly essential. There is a wealth of literature on the dynamic analysis of vehicles with planar motion, but the effect of gravity component on the lateral and longitudinal dynamics of a vehicle moving on a non-flat road is mainly ignored in the previous studies. Driving on a non-flat road (a road with bank and/or grade angles) commonly happens in both race tracks and urban/highway driving. Therefore, either for designing a controller for a passenger vehicle or a performance vehicle, the effect of road angles must be considered. Designing a controller without considering the gravity component effects on the vehicle dynamics would results in poor performance of the controller as soon as the vehicle enters a road with the bank and/or grade angles. Therefore, the road condition must be considered in the modeling for the dynamic analysis which gives the control designers the most accurate insight into vehicle behavior.

In this study, a 3-DOF vehicle model on a non-flat road is developed. The vehicle states consist of the yaw rate (r), which describes the vehicle rotation around the z axis, vehicle sideslip angle (β), and the longitudinal velocity (v_x) at the vehicle center of gravity (CG). The road has a bank angle ϕ_r and grade with the angle θ_r . It should be noted that at this stage of the investigation, the roll and pitch dynamics of the vehicle have been neglected due to the complexity of the 3-DOF model.

3.1. Vehicle Motions on Non-Flat Road

In this section, the motion of a vehicle moving on a non-flat road is investigated. The schematic model of the vehicle is shown in Figure 3-1. The (xyz) coordinate system is assumed to be fixed to the vehicle's center of gravity. The right-hand rotation of the coordinate system around z-axis is defined as the vehicle yaw angle (ψ), the right-hand rotation about the x-axis is shown as θ_r, which represents the road grade, and its right-hand rotation about the y-axis represents the road bank and is shown by ϕ_r. As the vehicle moves on the non-flat road, the (xyz) coordinate system rotates with the vehicle. The rotation of the coordinate system with respect to a fixed reference system can be described by the following rotation matrix where c and s are short for cosine and sine, respectively [90]:

$$C_\phi = \begin{bmatrix} 1 & 0 & 0 \\ 0 & \cos\phi_r & \sin\phi_r \\ 0 & -\sin\phi_r & \cos\phi_r \end{bmatrix} \tag{3-1-a}$$

$$C_\theta = \begin{bmatrix} \cos\theta_r & 0 & -\sin\theta_r \\ 0 & 1 & 0 \\ \sin\theta_r & 0 & \cos\theta_r \end{bmatrix} \tag{3-1-b}$$

$$C_\psi = \begin{bmatrix} \cos\psi & \sin\psi & 0 \\ -\sin\psi & \cos\psi & 0 \\ 0 & 0 & 1 \end{bmatrix} \tag{3-1-c}$$

$$C = C_\phi C_\theta C_\psi = \begin{bmatrix} c\theta_r\, c\psi & c\theta_r\, s\psi & -s\theta_r \\ (-c\phi_r\, s\psi + s\phi_r\, s\theta_r\, c\psi) & (c\phi_r\, c\psi + s\phi_r\, s\theta_r\, s\psi) & s\phi_r\, c\theta_r \\ (s\phi_r\, s\psi + c\phi_r\, s\theta_r\, c\psi) & (-s\phi_r\, c\psi + c\phi_r\, s\theta_r\, s\psi) & c\phi_r\, c\theta_r \end{bmatrix} \tag{3-2}$$

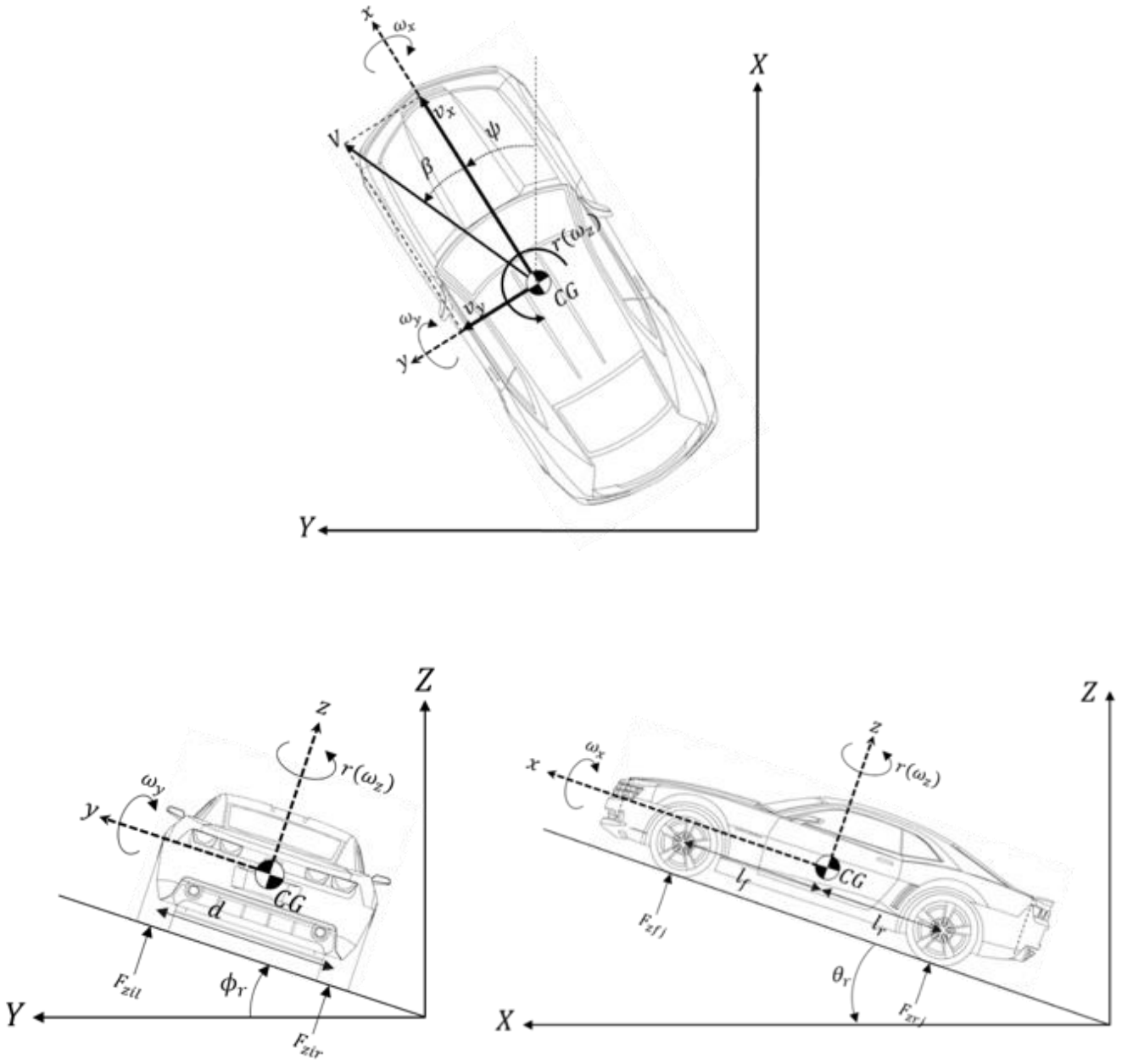

Figure 3-1. Schematic modeling of vehicle on road with bank and grade angles

In order to find the relative angular velocity of the vehicle shown in Figure 3-1, the right-handed rotation matrices of C_ϕ and C_θ must be applied to the reference frame angular velocity as follow [94]:

$$\vec{\Omega} = \begin{bmatrix} \omega_x \\ \omega_y \\ \omega_z \end{bmatrix} = \begin{bmatrix} \dot{\phi}_r \\ 0 \\ 0 \end{bmatrix} + C_\phi \left(\begin{bmatrix} 0 \\ \dot{\theta}_r \\ 0 \end{bmatrix} + C_\theta \begin{bmatrix} 0 \\ 0 \\ \dot{\psi} \end{bmatrix} \right) \tag{3-3}$$

By doing the matrix multiplication, the rotation matrix for calculating the vehicle angular velocities can be found as:

$$\vec{\Omega} = \begin{bmatrix} 1 & 0 & -\sin\theta_r \\ 0 & \cos\phi_r & \sin\phi_r \cos\theta_r \\ 0 & -\sin\phi_r & \cos\phi_r \cos\theta_r \end{bmatrix} \begin{bmatrix} \dot{\phi}_r \\ \dot{\theta}_r \\ \dot{\psi} \end{bmatrix} \tag{3-4}$$

Therefore, the angular velocities of the vehicle can be obtained as follow:

$$\vec{\Omega} = \begin{bmatrix} \omega_x \\ \omega_y \\ \omega_z \end{bmatrix} = \begin{bmatrix} \dot{\phi}_r - sin\theta_r\, \dot{\psi} \\ cos\phi_r\, \dot{\theta}_r + sin\phi_r\, cos\theta_r\, \dot{\psi} \\ -sin\phi_r\, \dot{\theta}_r + cos\phi_r\, cos\theta_r\, \dot{\psi} \end{bmatrix} \tag{3-5}$$

In the next step, the velocity and acceleration of the vehicle must be defined. To do so, first, the coordinate systems must be set. Assuming a fixed coordinate system in the inertial space as (XYZ) and a coordinate system fixed to the vehicle body as (xyz). The rotation of the (xyz) is the same as explained before in Eq. (3-2).

Assuming a fixed point on the vehicle body, the displacement of this point can be expressed as:

$$\vec{r} = \begin{bmatrix} x \\ y \\ z \end{bmatrix} \tag{3-6}$$

A schematic model of the vehicle moving on a road with the bank and grade angles is shown in Figure 3-2. The inertial and the fixed coordinate systems are also shown in this figure.

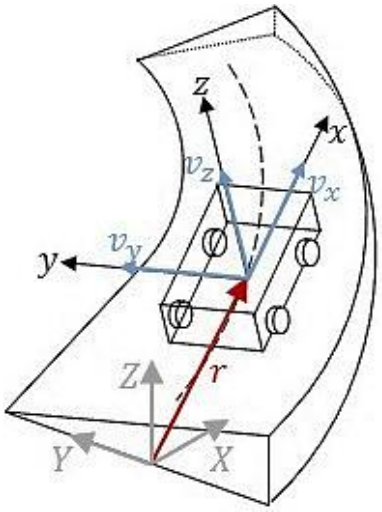

Figure 3-2. Rotation of the coordinate system as the vehicle moves along the inclined road

Therefore, the inertial velocity and acceleration of the vehicle are defined as [95]:

$$\vec{v}_{inertial} = \dot{\vec{r}} + \left(\vec{\Omega} \times \vec{r}\right) \tag{3-7}$$

$$\vec{a}_{inertial} = \ddot{\vec{r}} + \vec{\Omega} \times \left(\vec{\Omega} \times \vec{r}\right) + \left(\dot{\vec{\Omega}} \times \vec{r}\right) + 2\left(\vec{\Omega} \times \dot{\vec{r}}\right) \tag{3-8}$$

where $\dot{\vec{r}}$ and $\ddot{\vec{r}}$ are the respective velocity and acceleration of the vehicle body due to the motion in (xyz). Substituting Eqs. (3-4) and (3-6) into Eqs. (3-7) and (3-8) and by applying derivatives and after

some mathematical simplifications, the relative velocity and acceleration can be rewritten in the following forms:

$$\vec{v}_{inertial} = \begin{bmatrix} v_x \\ v_y \\ v_z \end{bmatrix} = \begin{bmatrix} \dot{x} + z\omega_y - y\omega_z \\ \dot{y} - z\omega_x + x\omega_z \\ \dot{z} + y\omega_x - x\omega_y \end{bmatrix} \tag{3-9}$$

$$\vec{a}_{inertial} = \begin{bmatrix} a_x \\ a_y \\ a_z \end{bmatrix}$$

$$= \begin{bmatrix} \ddot{x} - \dot{y}\omega_z - y\dot{\omega}_y + \dot{z}\omega_y + z\dot{\omega}_y - \omega_z(\dot{y} - z\omega_x + x\omega_z) + \omega_y(\dot{z} + y\omega_x - x\omega_y) \\ \ddot{y} - \dot{z}\omega_x - z\dot{\omega}_x + \dot{x}\omega_z + x\dot{\omega}_x + \omega_z(\dot{x} + z\omega_y - y\omega_z) - \omega_x(\dot{z} + y\omega_x - x\omega_y) \\ \ddot{z} + \dot{y}\omega_x + y\dot{\omega}_x - \dot{x}\omega_y - x\dot{\omega}_y - \omega_y(\dot{x} + z\omega_y - y\omega_z) + \omega_x(\dot{y} - z\omega_x + x\omega_z) \end{bmatrix} \tag{3-10}$$

By separating the time derivative components of the relative velocity, the relative acceleration can be rewritten in a simplified form. The time derivative of the velocity is defined as:

$$\frac{d}{dt} v_{inertial} = \begin{bmatrix} \frac{d}{dt} v_x \\ \frac{d}{dt} v_y \\ \frac{d}{dt} v_z \end{bmatrix} = \begin{bmatrix} \ddot{x} - \dot{y}\omega_z - y\dot{\omega}_y + \dot{z}\omega_y + z\dot{\omega}_y \\ \ddot{y} - \dot{z}\omega_x - z\dot{\omega}_x + \dot{x}\omega_z + x\dot{\omega}_x \\ \ddot{z} + \dot{y}\omega_x + y\dot{\omega}_x - \dot{x}\omega_y - x\dot{\omega}_y \end{bmatrix} \tag{3-11}$$

By replacing Eqs. (3-9) and (3-11) in Eq. (3-10), the acceleration can be simplified as follow:

$$\vec{a}_{inertial} = \begin{bmatrix} \frac{d}{dt}v_x - \omega_z v_y + \omega_y v_z \\ \frac{d}{dt}v_y + \omega_z v_x - \omega_x v_z \\ \frac{d}{dt}v_z - \omega_y v_x + \omega_x v_y \end{bmatrix} \quad (3\text{-}12)$$

3.1.1. Combined Slip Tire Model

Tires are the most important component in terms of controlling vehicle motions and direction during accelerating and braking. The four contact patches between the tires and ground are the main sources of force to the vehicle. Therefore, there are many different tire models developed to capture tire properties and force generations at their most accurate level. Some of the models are based on the experimental data known as the empirical models, such as the Magic Tire Formula, and some others are based on the physical and kinematic characteristics of tires at the contact patch like the Brush Tire Models [96]. The Fiala tire model is one of the common brush tire models, which has been chosen for this study.

In the simplest form of the Fiala tire model, it is assumed that the lateral force generated by the tire has a linear relationship between the tire sideslip angles. The ratio of the tire lateral and longitudinal velocities represents the tire sideslip angle as:

$$\tan \alpha = \frac{v_y}{v_x} \quad (3\text{-}13)$$

The tire sideslip angle is the tire lateral deflection at the contact patch, which provides the required lateral force. The amount of the lateral force at the contact patch, can be found based on the linear brush model as:

$$F_y = C_\alpha \alpha \quad (3\text{-}14)$$

where C_α is the stiffness of the tire brushes, also known as the tire cornering stiffness. The linear brush model can approximate the tire lateral force, accurate enough while the tire side slip is small, but as the tire sideslip angle increases, this linear model cannot capture the correct tire forces anymore. Therefore, the linear brush model has been modified to the lateral brush tire model which considers the tire saturation during high slip situations. Indeed, a more complicated model is required to address the tire behavior when the sideslip angle is high. The Fiala tire model is a nonlinear brush model that can model tire lateral forces both at law and high sideslip angles. In this model, the tire lateral force is a function of the tire normal load F_z, the road friction coefficient μ, cornering stiffness C_α, and tire sideslip angle α as follows:

$$F_y = \begin{cases} -C_\alpha \tan\alpha + \dfrac{C_\alpha^2}{3\,\mu\,F_z}|\tan\alpha\,|\tan\alpha\, - \dfrac{C_\alpha^3}{27\,\mu^2\,F_z^2}\tan^3\alpha & |\alpha\,| \le \alpha_{lim} \\ -\mu\,F_z\,sgn\,\alpha & |\alpha\,| > \alpha_{lim} \end{cases} \tag{3-15}$$

where α_{lim} is the smallest tire slip angle at which, the total contact patch has reached its friction limit as:

$$\alpha_{lim} = \arctan\frac{3\mu F_z}{C_\alpha} \tag{3-16}$$

By using the lateral brush model, the linear behavior of the tire at the small values of sideslip angle will be captured as well as the saturation of the tire when it reaches the friction limits at the higher tire sideslip angles. However, this model does not consider the combined effect of the longitudinal and lateral forces. Therefore, in cases where the longitudinal force exists, the lateral brush model cannot approximate the correct value of the tire lateral forces and can develop errors in simulation and vehicle dynamic modeling. To overcome this problem, the combined slip brush tire model has been introduced, which considers the combined effect of the longitudinal force generation on the lateral tire forces in the presence of either braking or accelerating. In this model, a new parameter ζ is defined which is coming from the tire friction limits and assumes the friction limit to be a circle. It should be mentioned that the

maximum tire capacity in force generation is μF_z and the friction circle defines the relationship between the longitudinal and lateral tire force at the friction limits as:

$$\mu F_z = \sqrt{F_x^2 + F_y^2} \tag{3-17}$$

The combined slip tire model, known as the combined slip Fiala tire model, is defined as:

$$F_y = \begin{cases} -C_\alpha \tan\alpha + \dfrac{C_\alpha^2}{3\,\zeta\,\mu\,F_z}|\tan\alpha\,|\tan\alpha\, - \dfrac{C_\alpha^3}{27\zeta^2\,\mu^2\,F_z^2}\tan^3\alpha & |\alpha\,| \le \alpha_{lim} \\ -\zeta\,\mu\,F_z\,sgn\,\alpha & |\alpha\,| > \alpha_{lim} \end{cases} \tag{3-18}$$

where

$$\zeta = \frac{\sqrt{(\mu F_z)^2 - F_x^2}}{\mu F_z} \tag{3-19}$$

Since the vehicle longitudinal dynamics, i.e., accelerating and braking, is an important part of this study, the tire model should have the capability of modeling the force generation in both the lateral and longitudinal directions. Therefore, the nonlinear combined slip Fiala tire model has been chosen as the tire model in this thesis.

3.2. Vehicle Dynamic Model

A double-track vehicle model is considered to derive the equations of motion of the longitudinal, lateral, and the yaw dynamics. It is assumed that the vehicle is an all-wheel drive with the front-wheel steering.

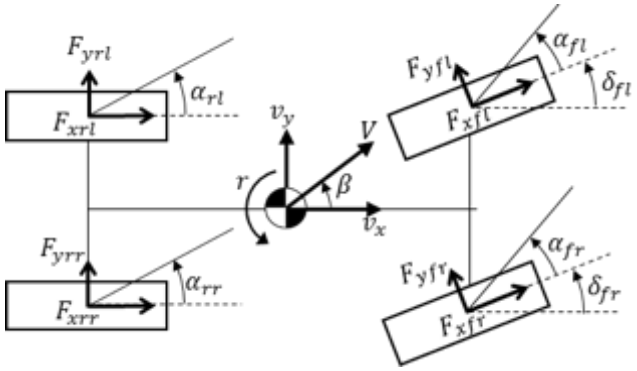

Figure 3-3. A double-track vehicle model

As shown in Figure 3-3, the longitudinal and lateral tire forces acting on the corners are shown as F_{xij} and F_{yij} where i denotes the front and rear axles and j denotes the left and right sides, which the forces are acting on them. The steering angles at the front tires are presented as δ_{fj} and the tire side slip angles are shown by α_{ij} as defined by:

$$\alpha_{fi} = \arctan\frac{v_y + l_f\, r}{v_x} - \delta_{fi} \cong \frac{v_y + l_f\, r}{v_x} - \delta_{fi}, \qquad i = r, l. \tag{3-20}$$

$$\alpha_{ri} = \arctan\frac{v_y - l_r\, r}{v_x} \cong \frac{v_y - l_r\, r}{v_x}, \qquad i = r, l. \tag{3-21}$$

The vehicle has a total mass m, and the yaw moment of inertia I_z. The distances of the front and rear axles to the CG are l_f and l_r, respectively. Since the vehicle is at the limits of the handling, the normal load transfer due to the longitudinal and lateral accelerations must be considered. Therefore, after applying the effect of the road angles, Eq. (3-2), the normal loads at each corner will be defined as:

$$F_{z,fr} = \frac{mg(cos\theta_r\, cos\phi_r)\, l_r - m\, a_x\, h}{2(l_f + l_r)} + \frac{m\, a_y h}{2d} \tag{3-22}$$

$$F_{z,fl} = \frac{mg(cos\theta_r\, cos\phi_r)\, l_r - m\, a_x\, h}{2(l_f + l_r)} - \frac{m\, a_y h}{2d} \tag{3-23}$$

$$F_{z,rr} = \frac{mg(cos\theta_r\, cos\phi_r)\, l_f + m\, a_x\, h}{2(l_f + l_r)} + \frac{m\, a_y h}{2d} \tag{3-24}$$

$$F_{z,rl} = \frac{mg(cos\theta_r\, cos\phi_r)\, l_f + m\, a_x\, h}{2(l_f + l_r)} - \frac{m\, a_y h}{2d} \tag{3-25}$$

By neglecting the wheel speed dynamics, the longitudinal forces can be determined by the torque command at each corner as:

$$F_{xij} = \frac{T_{ij}}{R_{eff}} \tag{3-26}$$

where R_{eff} is the effective tire radius and T_{ij} is the torque applied to the tires at each corner. The lateral forces applied at each corner of the vehicle can be found using the combined slip Fiala tire model introduced in Eq. (3-18).

Therefore, by having the tire forces defined in this section and the acceleration found in the previous section, using Newton's law of dynamics, the equations of motion of the vehicle for the longitudinal, lateral, and the yaw dynamics can be written as:

$$\begin{aligned} m(\dot{v}_x - \omega_z v_y) = {} & F_{xfr}\cos(\delta_{fr}) + F_{xfl}\cos(\delta_{fl}) + F_{xrr} + F_{xrl} - F_{yfr}\sin(\delta_{fr}) \\ & - F_{yfl}\sin(\delta_{fl}) + mg\sin\theta_r - F_{aero} \end{aligned} \tag{3-27}$$

$$m(\dot{v}_y + \omega_z v_x) = F_{yfr}\cos(\delta_{fr}) + F_{yfl}\cos(\delta_{fl}) + F_{yrr} + F_{yrl} + F_{xfr}\sin(\delta_{fr}) + F_{xfl}\sin(\delta_{fl}) - mg\ sin\phi_r\ cos\theta_r \quad (3\text{-}28)$$

$$I_z\dot{r} = l_f(F_{yfr}\cos(\delta_{fr}) + F_{yfl}\cos(\delta_{fl}) + F_{xfr}\sin(\delta_{fr}) + F_{xfl}\sin(\delta_{fl})) - l_r(F_{yrr} + F_{yrl}) \quad (3\text{-}29)$$

The last term of Eq. (3-27), F_{aero} is the aerodynamic drag force and can be calculated as:

$$F_{aero} = \frac{1}{2}\rho A C_d v_x^2 \quad (3\text{-}30)$$

where ρ is the air mass density, A is the vehicle frontal area, and C_d is the drag force coefficient. Since the lateral, longitudinal, and the yaw dynamics of the system are the main concern of this study, the vertical motion of the vehicle has been neglected at this stage and its effect can be examined carefully in future studies.

3.3.Non-flat Road Effect on the Open-Loop Vehicle Dynamics

The open-loop dynamics of a vehicle moving along a path with bank and grade have been studied in this section. The vehicle states are modeled based on the developed equations of motion presented in the previous section as Eqs. (3-27) to (3-29). The numerical values of the model parameters, used in this section, are presented in **Table 3-1**.

It is assumed that the road is dry with a friction coefficient μ and the friction coefficient must be estimated by using the estimation algorithms available but for now, it is assumed to be known. For examining the effect of the road angle effect on the vehicle dynamics, a path with the bank and gradient has been chosen as shown in Figure 3-4. The path has the curvature in the X-Y plane, as shown in

Figure 3-4(b), and its altitude changes from $-5m$ to $+5m$. Also, the road angle variations with time are presented in Figure 3-5 (a) for the road gradient (θ_r) and Figure 3-5 (b) for the bank angle (ϕ_r).

Table 3-1. Physical parameters of the vehicle used for open-loop simulation

Parameter	Value	Parameter	Value
$m\ (kg)$	1530	$R_{eff}\ (m)$	0.325
$I_z\ (kg.m^2)$	2315.3	$h\ (m)$	0.52
$A\ (m^2)$	2.3	$C_{\alpha f}\ (N/rad)$	69,302
$l_f\ (m)$	1.11	$C_{\alpha r}\ (N/rad)$	52,360
$l_r\ (m)$	1.67	C_d	0.30
$d\ (m)$	1.55	μ	0.85

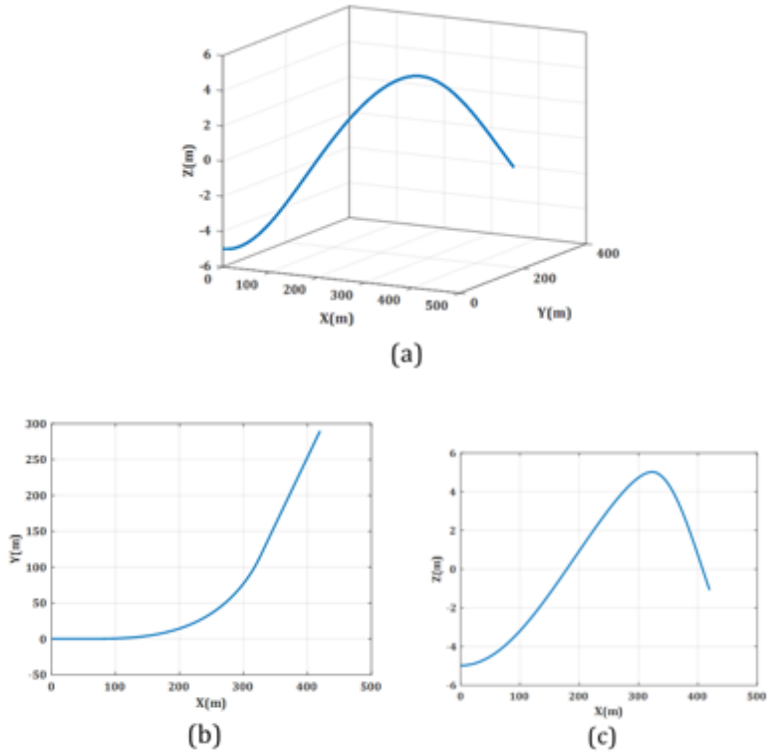

Figure 3-4. The path with gradient and bank angle: (a) 3-D view, (b) X-Y view, (c) X-Z view

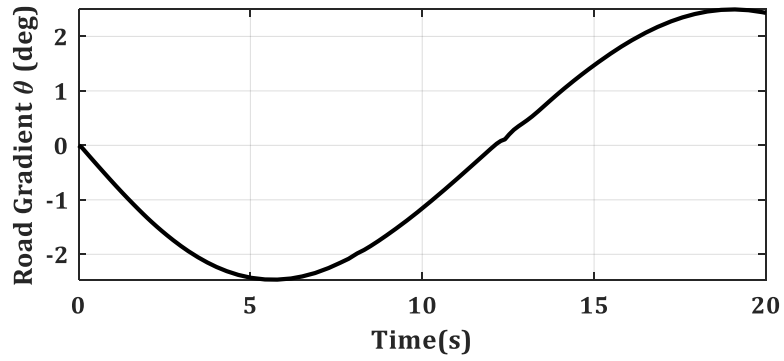

(a)

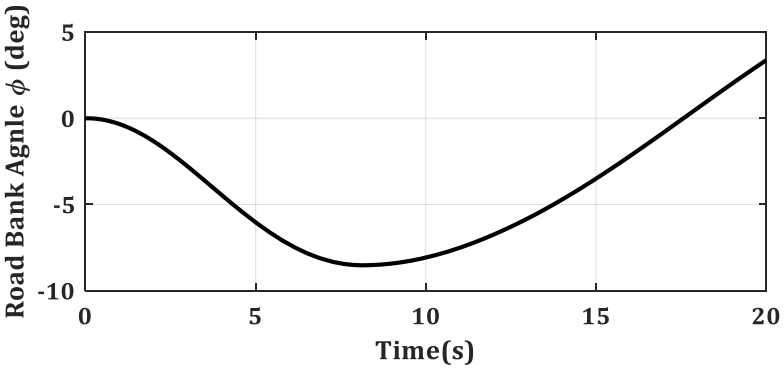

(b)

Figure 3-5. Road angles of the path used in the CarSim simulation

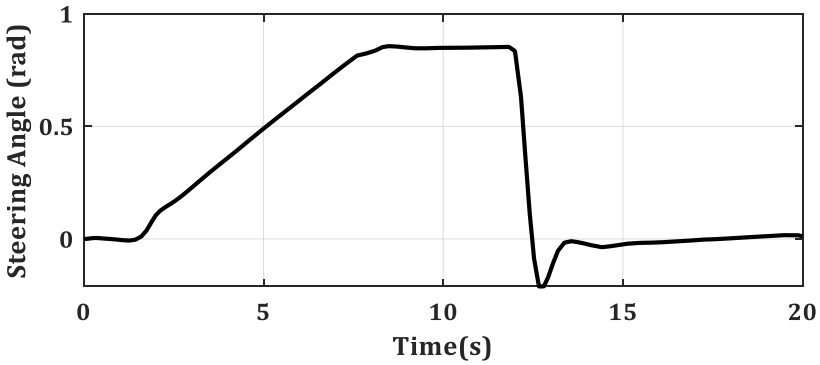

Figure 3-6. Steering command to the vehicle

To complete the path, the steering command shown in Figure 3-6 is applied to the model with zero motor torque. The vehicle has a front-wheel steer and it is assumed that the steering angle transferred to the left and right wheels are the same. The vehicle open-loop dynamics obtained from Eqs. (3-27) to (3-29) is presented in Figure 3-7 with a solid blue line considering the road angles.

The open-loop responses of the same vehicle having the same driver inputs and under the same road conditions are obtained and shown in the figure with CarSim® software (red dash line) and also using Eqs. (3-27) to (3-29) without considering the road angle effects (black dash line).

The comparison performed between the results obtained from CarSim® and those obtained from the developed model shows the importance of considering the road angles in the mathematical modeling. It can be seen from Figure 3-7 that although the road angles do not have a huge effect on the vehicle yaw rate, their impacts on both lateral and longitudinal velocities are considerable. In the case of using the developed model for the vehicle control on non-flat roads, the importance of including the road angles would become evident.

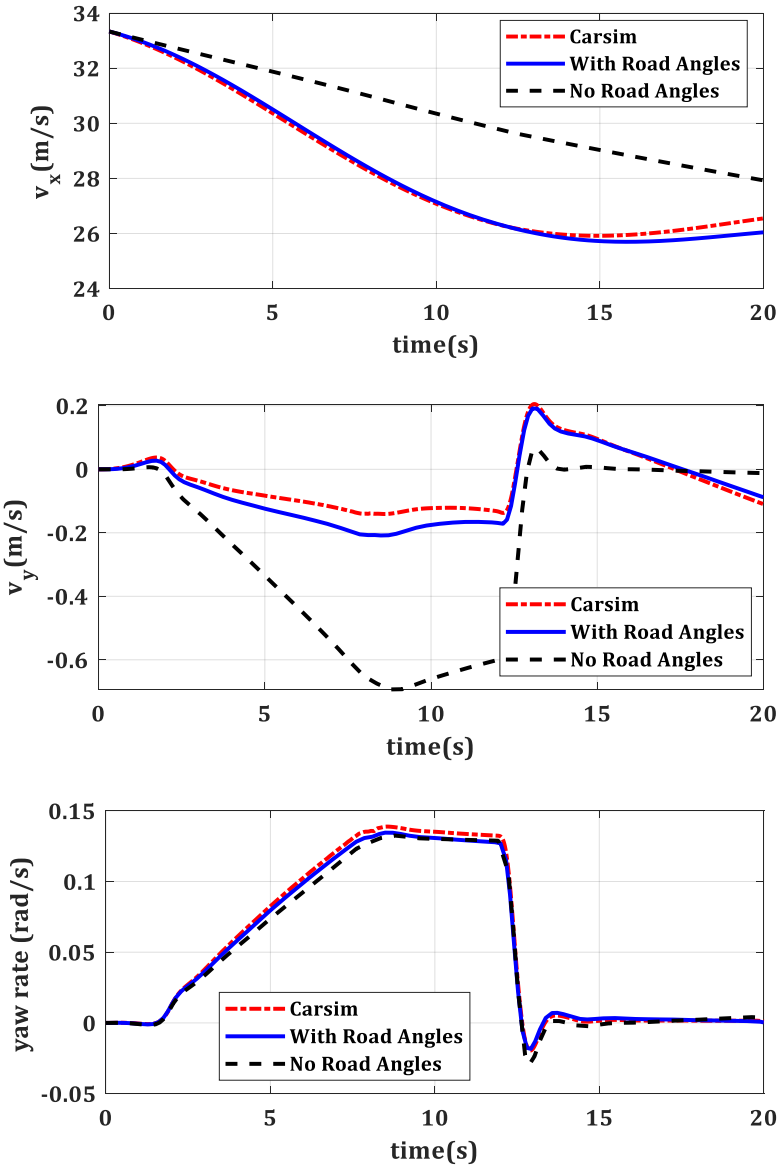

Figure 3-7. Open-loop Vehicle response obtained from CarSim® and mathematical modeling with and without road angles effect: (a) longitudinal velocity, (b) lateral velocity, (c) yaw rate

3.4. Summary

A vehicle dynamic model including the road angles was proposed in this chapter. The road angles including the bank and gradient were analytically considered in the equations of motion of the vehicle. The lateral and longitudinal dynamics were investigated and evaluated with a CarSim high-fidelity model to show the improvement of the proposed model compared to the conventional models available in literature. When the vehicle was assumed to move on a road with the bank and grade, the proposed model could estimate the yaw rate and sideslip angle of the vehicle to be much closer to the CarSim high-fidelity model, while the conventional model had noticeable error values in the modeling of the main states of the vehicle.

Chapter 4

Optimal Torque Distribution at Limits of Handling

The torque distribution either to the front and rear axles or to each corners of the vehicle is an important concept in the vehicle dynamics control, especially while driving at the limits of handling. Torque distribution has a direct impact on the total yaw moment acting on the vehicle, which affects its both handling and stability. When an optimal ratio of torque distribution is applied to the vehicle, each tire can use its maximum capacity of force generation in both lateral and longitudinal directions. When a constant ratio of input torque is sent to the tires, then a tire might not be able to use that amount of torque efficiently. This is a common situation during either a high acceleration/deceleration or a sharp turn maneuver, and it happens due to the normal load transfers. Therefore, when there is a significant amount of normal load transfers, a tire cannot handle too much torque sent to it and instead of creating desired values of lateral\longitudinal forces, the tire spins with a high slip ratio.

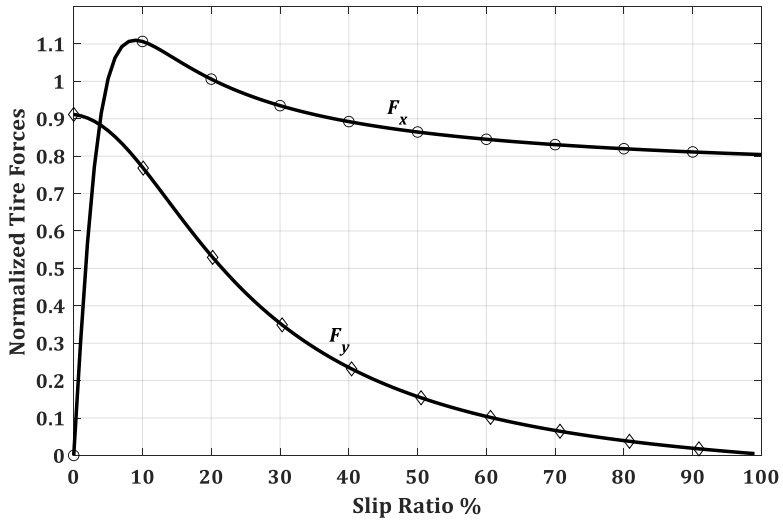

Figure 4-1.Effect of slip ratio on tire capacity

When a tire slip ratio increases and goes above 20%, the tire force capacity drastically drops, especially in the lateral direction. Figure 4-1 shows tire force variations with respect to the slip ratio. As shown in this figure, during high slip ratios, lateral force generation is almost zero. When a high amount of torque is sent to a wheel with a low normal load acting on it, it causes a high slip ratio and therefore, there is no capacity for lateral force generation.

For instance, a driver may decide to accelerate while performing a sharp turn. As the driver presses the gas pedal, the acceleration in longitudinal direction causes normal load transfer from the front axle to the rear axle. This means even when there is no steering angle, just acceleration can affect normal loads acting on the tire. Since the scenario is a turn-in-acceleration, there is also lateral load transfer from the inner tires to outer tires. In other words, the front-inner tire has the minimum tire capacity, and the rear-outer tire has the maximum tire capacity. In this scenario, if the vehicle is a front-wheel-drive (FWD) and the front axle is an open differential, it means 50% of the torque is being sent to a tire with almost no capacity for force generation. Therefore, front tires saturate and cannot generate enough lateral forces and the vehicle travels an understeer trajectory instead of the desired trajectory.

With the recent developments, electric motors can drive each axle or even each wheel independently to produce any desired wheel torque. Having an electric motor on each corner will let the optimal torque being sent to each wheel to keep the slip ratio in a range which can create maximum possible longitudinal and lateral forces. The maximum tire capacities at each corner can be used when the optimal torque is sent to each wheel. Therefore, lateral and longitudinal grips would be maximized. When a vehicle is traveling at its limits of handling, maximization of lateral grip assures the vehicle has the highest capacity for cornering maneuvers. For instance, if a vehicle is traveling a straight path, optimizing the torque allocation would let the driver apply sharp steering and travel the trajectory with no understeering or oversteering behavior. Preventing the vehicle from under\oversteering will also enhance vehicle stability.

4.1. Torque Distribution Based on Dynamic Square

As explained in literature, Dynamic Square plots the nominal values of the front and rear axle forces based on the available lateral and longitudinal grip as shown in Figure 4-2. In this Dynamic Square, the solid black lines show the torque distribution quadrilaterals. Each quadrilateral represents the front\rear

axle torques with the specified amount of lateral acceleration. The numbers on the edges of each quadrilateral show the available lateral accelerations. It can be seen from Figure 4-2 that as the available lateral acceleration increases, the related quadrilateral shrinks to a smaller size compared to the ones belong to the lower lateral accelerations. When the quadrilaterals shrink, the edges bend into arc shapes at the higher values of lateral acceleration. This specifically happens in the middle area of the Dynamic Square. The whole Dynamic Square is divided into three sections: the two side parts shown with red surface color and the middle part shown by blue surface color. The iso-curves in the blue zone represent the force distributions to the front and rear axles, which make the vehicle oversteer with creating a positive yaw moment, i.e. the rear axle saturates before the front axle. The iso-curves in the red zones represent the force distributions to the front and rear axles, which make the vehicle understeer with creating a negative yaw moment, i.e. the rear axle saturates before the front axle. Two lines with red circle markers separate the oversteering and understeering zones. These lines show the force ratios in which the vehicle yaw moment is zero. Zero yaw moment happens at the vertices of each quadrilateral where both axles saturate simultaneously. At the vertices, the lateral and longitudinal grips are at their maximum values. Connecting all vertices would create the lines of $M_z = 0$, (lines with the red circle markers in Figure 4-2).

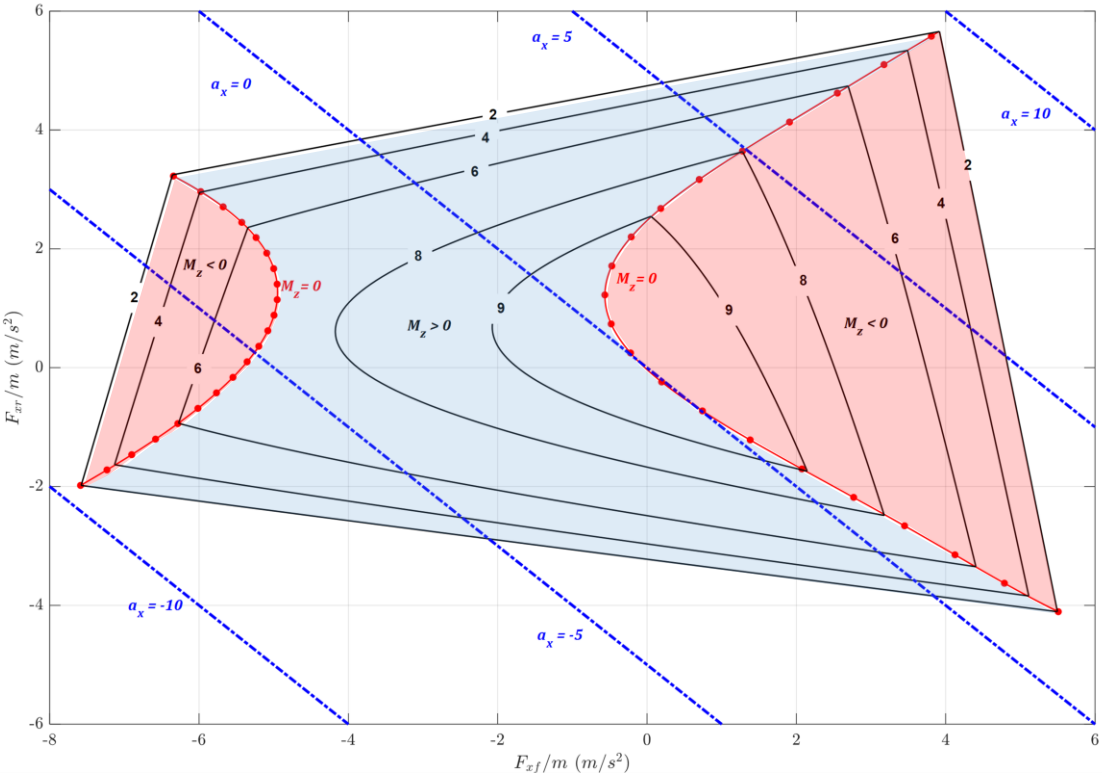

Figure 4-2. Dynamic Square

The Dynamic Square is plotted based on the nominal value of the longitudinal force at the rear axle against the nominal value of the longitudinal force at the front axle. The black solid lines show the maximum lateral acceleration available at each point based on the longitudinal force ratio and the blue dashed lines represent the longitudinal acceleration of each point on the figure space. As mentioned before, the vertices of each quadrilateral are the points where both the longitudinal and lateral accelerations are maximum. Therefore, by moving along the vertices for each quadrilateral with different lateral accelerations, the line of optimal longitudinal force distribution to the front and rear axles can be found, as the lines with red circle markers.

Based on the driver input (brake or gas), the requested longitudinal forces may either be positive or negative. Depending on the requested force on each axle, either positive or negative force, the Dynamic Square divides into four parts: (a) both axles have positive forces, (b) the front axle has a positive force and rear axle has a negative force, (c) both axles have negative forces, and (d) the front

axle has a negative force and rear axle has a positive force. Since having longitudinal forces with opposite directions on the axle are not common and out of the scope of this dissertation, parts (b) and (d) are neglected and the rest of the explanations should focus on parts (a) (acceleration) and (b) (braking).

Let us assume that the driver requests a positive longitudinal force (accelerating), therefore, part (a) the top-right corner of the dynamic square will be considered. In order to find the optimal force ratio for each axle, as mentioned before, the line $M_z = 0$ in the top right corner must be followed. However, as shown in the figure, when we are at part (a), the exact line $M_z = 0$ cannot be followed as a section of this line lays in part (d). In other words, for having the optimal force distribution, during lower longitudinal acceleration, dynamic square askes for negative force on the front axle. Since sending a negative force to the front axle is not of our interest, instead of following the exact line$M_z = 0$, the line is shown with the green square markers in Figure 4-3 has to be followed instead. This line represents the simplest form of an optimal force distribution for a vehicle in acceleration mode, which maximizes the lateral and longitudinal grips.

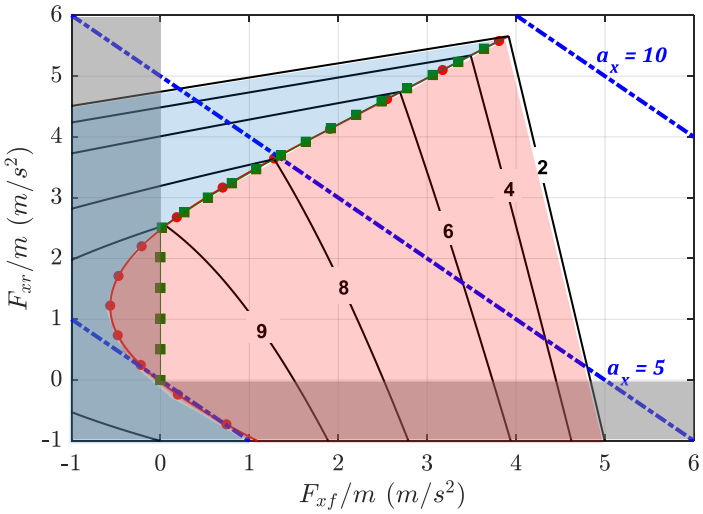

Figure 4-3. Dynamic Square and the optimal torque distribution

The iso-curves of the dynamic square are plotted based on the quasi-steady state cornering condition where $\dot{r} \approx 0$ and $\dot{\beta} \approx 0$ which would result in the following dynamic equations [13]:

$$\begin{cases} F_{xf} + F_{xr} = m\, a_x \\ F_{yf} + F_{yr} = m\, a_y \\ l_f F_{yf} - l_r F_{yr} = 0 \end{cases} \tag{4-1}$$

where the lateral forces are estimated based on the friction circle. Also, considering load transfer caused by longitudinal acceleration, the normal loads are defined as:

$$F_{z,f} = \frac{m}{l}(l_r g - a_x\, h) \tag{4-2}$$

$$F_{z,r} = \frac{m}{l}\left(l_f g + a_x\, h\right) \tag{4-3}$$

Since it is assumed that the vehicle is at the limits of handling, depending on the axle that saturates first, the limit of lateral grip will be defined. For instance, if the front axle saturates first, the front axle lateral force is $F_{yf} = F_{yf,lim}$. Since it is assumed that $\dot{r} \approx 0$, the following relationship can be obtained:

$$l_f F_{yf,lim} - l_r F_{yr} = 0 \tag{4-4}$$

The following equation must be solved for F_{yr} as:

$$F_{yr} = \frac{l_f F_{yf,lim}}{l_r} \tag{4-5}$$

Therefore, the maximum lateral grip, when the front axle saturates first, can be found as:

$$a_{y,lim} = \frac{F_{yf,lim} + F_{yr}}{m} \tag{4-6}$$

By substituting Eq. (4-5) into Eq. (4-6), the maximum lateral grip can be rewritten as:

$$a_{y,lim} = \frac{lF_{yf,lim}}{ml_r} \tag{4-7}$$

Following the same procedure for the cases when either rear axle saturates first, or when both axles saturate, simultaneously, the lateral grip can be defined as [13]:

$$a_{y,lim} = \begin{cases} lF_{yf,lim}/ml_r & ,if\ M_{z,lim} < 0 \quad (a) \\ lF_{yr,lim}/ml_f & ,if\ M_{z,lim} > 0 \quad (b) \\ \left(F_{yf,lim} + F_{yr,lim}\right)/m & ,if\ M_{z,lim} = 0 \quad (c) \end{cases} \tag{4-8}$$

The iso-curves at the red zones in Figure 4-2 are plotted based on Eq. (4-8), the iso-curves at the blue zone are plotted by using Eq. (4-8), and the $M_z = 0$ lines are plotted using Eq. (4-8).

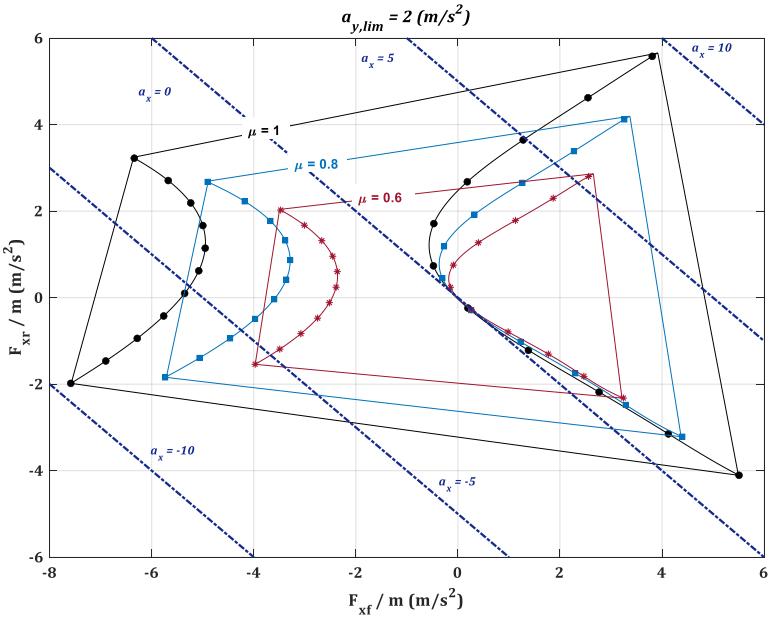

Figure 4-4. Road friction coefficient effect on the Dynamic Square

It should be noted that since the optimal solution is found under the condition of tire saturation at the limits of handling, the friction coefficient between the tire's contact patch and the road is playing a key role in this study. Therefore, it is necessary to know how sensitive the force distribution would be to the road friction coefficient.

Figure 4-4 shows the effect of the friction coefficient on Dynamic Square for the maximum lateral grip of 2 m/s^2. Three different values of the friction coefficient are considered. This figure shows that the longitudinal force distribution is quite sensitive to the friction coefficient and in order to have a precise solution to the optimal torque distribution, it is necessary to estimate the friction coefficient as accurately as possible.

4.2. Phase Portrait Analysis

As explained before, a phase portrait diagram reveals important information about the vehicle dynamics behavior. A 2-D phase portrait plots the steady-state response of the vehicle as iso-curves of yaw rate and sideslip angle. In order to plot a phase portrait diagram, it is assumed that the vehicle starts

from an initial condition of (v_{x0}, v_{y0}, r_0) and then continues either with or without the effect of control actuators. In Figure 4-5, each iso-curve represents open-loop vehicle dynamics with no additional actuation effect starting from different initial conditions.

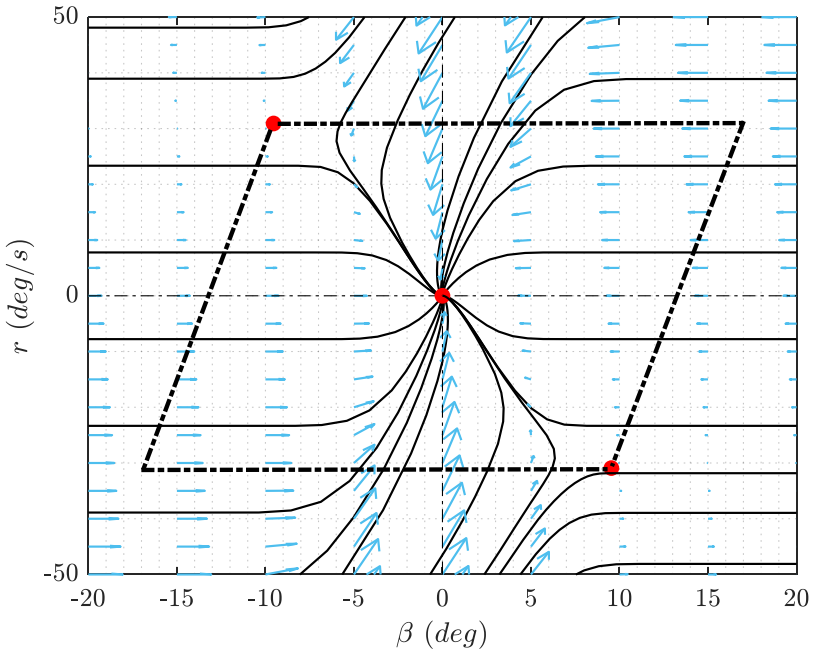

Figure 4-5. Open-loop dynamic and safe envelope, $v_x = 40$ km/h, $\mu = 0.85$, and $\delta = 0$

The plotted parallelogram shows the boundaries of the safe envelope which, separates the stable and unstable regions for the vehicle. The safe envelope is plotted based on the following equations [97]:

$$r_{max,ss} = \frac{\mu g}{v_x} \tag{4-9}$$

$$r_{min,ss} = -\frac{\mu g}{v_x} \tag{4-10}$$

$$\beta_{max,ss} = \frac{l_r r}{v_x} + \tan(\alpha_{lim}) \tag{4-11}$$

$$\beta_{min,ss} = \frac{l_r r}{v_x} - \tan(\alpha_{lim}) \tag{4-12}$$

As long as the vehicle states lay inside the safe envelope, it can be said that the vehicle is stable and when it goes out of the envelope, it becomes unstable. Depending on the vehicle states and condition at each moment, the vehicle may go back naturally to the stable region, but there are cases where the vehicle moves away from the stable area, and correction control actions such as steering or drive/brake torque are required to make it stable again. Since the objective of this thesis is to optimize the torque distribution, it is necessary to know how torque distribution affects the vehicle dynamics as well as safe envelope boundaries. Phase portraits can be a powerful tool to analyze the vehicle state's behavior under different torque distributions.

A sensitivity analysis performed to study the torque distribution effect on the equilibrium points, and isoclines of the phase plane. Various axial torque distributions are applied to the dynamic model introduced in the modeling section. It is assumed that steering input is zero at all times and the road condition is wet with $\mu = 0.55$. The total torque applied to the system is $T = 1500\ N.m$.

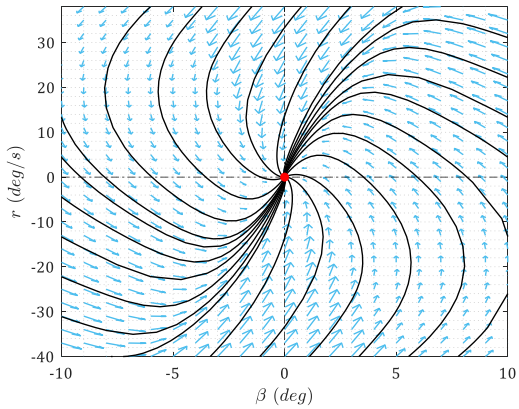

(a). $T_f = T, T_r = 0$

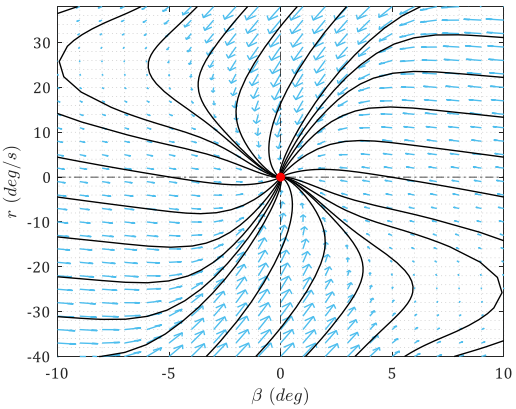

(b). $T_f = 0.7T, T_r = 0.3T$

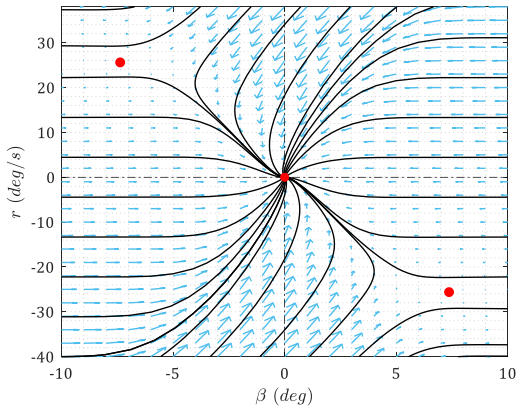

(c). $T_f = 0.6T, T_r = 0.4T$

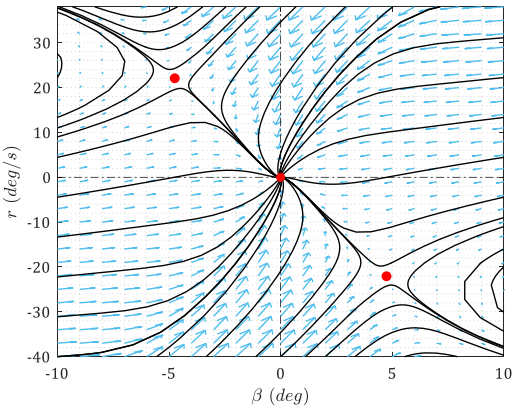

(d). $T_f = 0.5T, T_r = 0.5T$

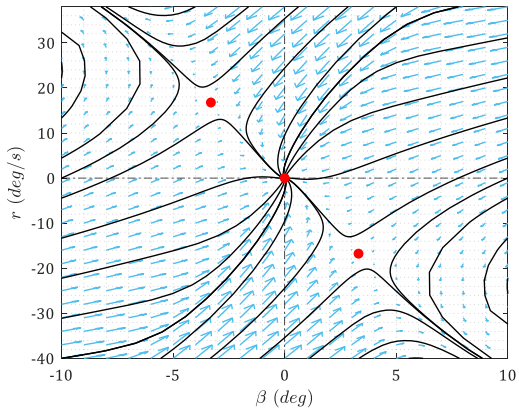

(e). $T_f = 0.4T, T_r = 0.6T$

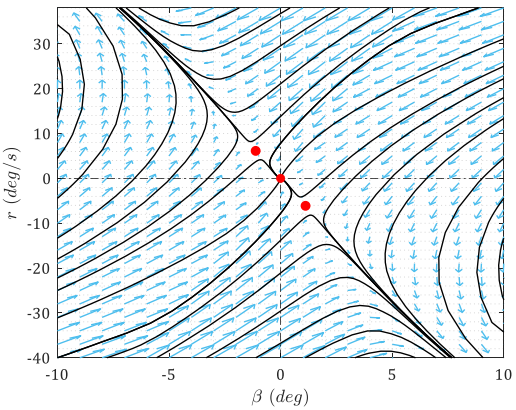

(f). $T_f = 0.3T, T_r = 0.7T$

Figure 4-6. Open-loop dynamic sensitivity to torque distribution, T = 1500 Nm, μ = 0.55, and δ = 0

As mentioned, Figure 4-6 shows a set of phase plane trajectories with various axial torque distribution ratios. For each phase plane, the equilibrium points are calculated and shown by the red dots. Also, the $(\beta - r)$ trajectories are shown along with their isoclines. In Figure 4-6(a), the front torque ratio with respect to the total torque is $T_f/T = 1$ and the rear axle torque is zero. Figure 4-6(b) shows the phase plane with the distribution ratio of $T_f/T = 0.7$ and $T_r/T = 0.3$. Figure 4-6 (c), (d), (e), and (f) have the ratios of $T_f/T = 0.6, 0.5, 0.4, \& \, 0.3$, respectively. Figure 4-6 shows that as the axial torque distribution varies through (a) to (f), the equilibrium points will move closer to the center of the phase plane. In Figure 4-6(a), all the requested torque is sent to the front axle. In this circumstance, there is only one stable equilibrium point and all isoclines starting from all initial conditions travel toward the stable point in the center of the phase plane. In the rest of this figure set, there are three equilibrium points. The equilibrium point in the center is stable and the two others are saddle points. It can be seen that changing the axial torque ratio has a significant effect on the location of the saddle points and as a result of the stability of the isoclines. Sending more torque to the rear axle moves the saddle point closer to the center and more isoclines get unstable. Although, sending more torque to the front axle enhances the stability, at the same time will affect the maneuverability of the vehicle during harsh cornering.

To study the stability margins of the vehicle under various torque distribution, three torque distributions are considered for the sensitivity analysis on the safe envelope. Phase planes with safe envelope boundaries, defined by Eqs. (4-9) to (4-12), are plotted and presented as Figure 4-7 for three different torque distribution of (a) 30% to the front and 70% to the rear axle, (b) 40% to the front axle and 60% to the rear one, and (c) 50% to the front axle and 50% to the rear one. It is assumed that the steering angle is $\delta = 0°$, initial longitudinal speed is $v_{x0} = 10\, m/s$, and the friction surface is $\mu = 0.55$. The total torque input is set as $T = 1500\, Nm$ and the axle torque distributions to the front-rear axles are, as explained before, 30-70, 40-60, and 50-50, respectively.

Sending higher values of input torque to the rear axle shrinks the safe envelope boundaries. This shows that for designing a stability controller to keep the vehicle states inside the safe envelope, the safe envelope boundaries must be updated with any variations of the torque distribution. Designing a stability controller with constant safe envelope boundaries cannot guarantee the stability of an electric vehicle when the torque distribution is being optimized online.

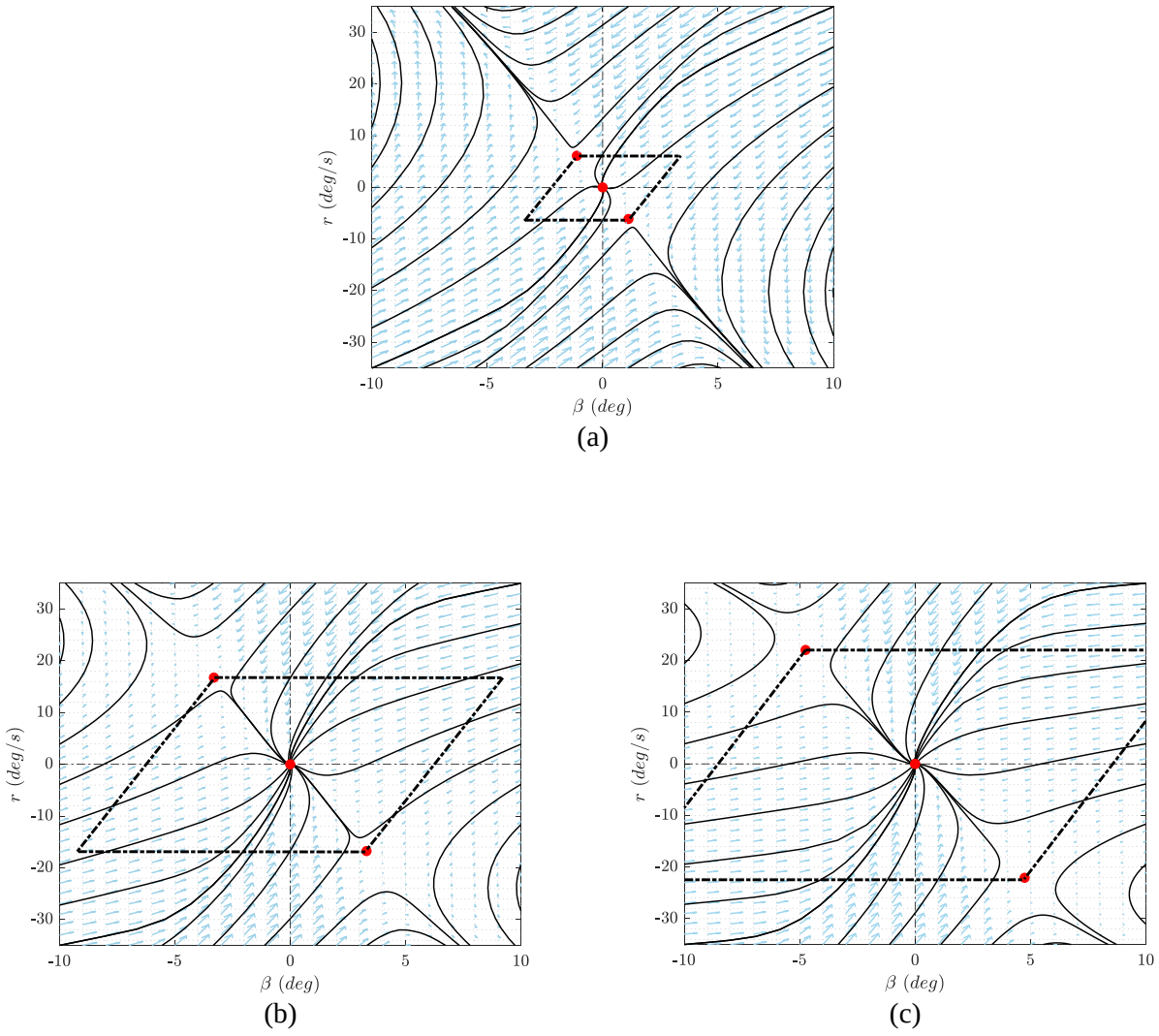

Figure 4-7. Open-loop Dynamics and safe envelop ($\mu = 0.55$, $v_{x0} = 10$ m/s, $\tau = 1500$ Nm, $\delta = 0$) : (a) $T_f = 0.3T$, $T_r = 0.7T$, (b)) $T = 0.4T$, $T_r = 0.6T$, and , (c)) $T_f = 0.5T$, $T_r = 0.5T$

To have a better comparison between different powertrains, a front-wheel drivetrain (FWD), a rear-wheel drivetrain (RWD), and an all-wheel drivetrain (AWD) are compared in all domain of a 2-D phase plane as shown in Figure 4-8. This comparison is performed at identical initial conditions with the initial longitudinal speed $v_{x0} = 10\ m/s$, and the steering angle kept constant with the magnitude $\delta = 0°$. The blue arrows show the velocity vectors of the AWD system with black arrows, velocity vectors of the RWD system with blue arrows, and the velocity vectors of the FWD system with red arrows. Depends on how torque is allocated to the axles, the vehicle dynamic responses change in various ranges. The available range between each pair of the red-blue arrows shows the range of yaw rate and side slip could vary based on the axle torque distribution. This range can define the playfield of torque distribution at that specific point. In case that the desired value for yaw rate and sideslip angle must be reached, the ratio of the torque distribution can be defined based on the available range between FWD and RWD vectors.

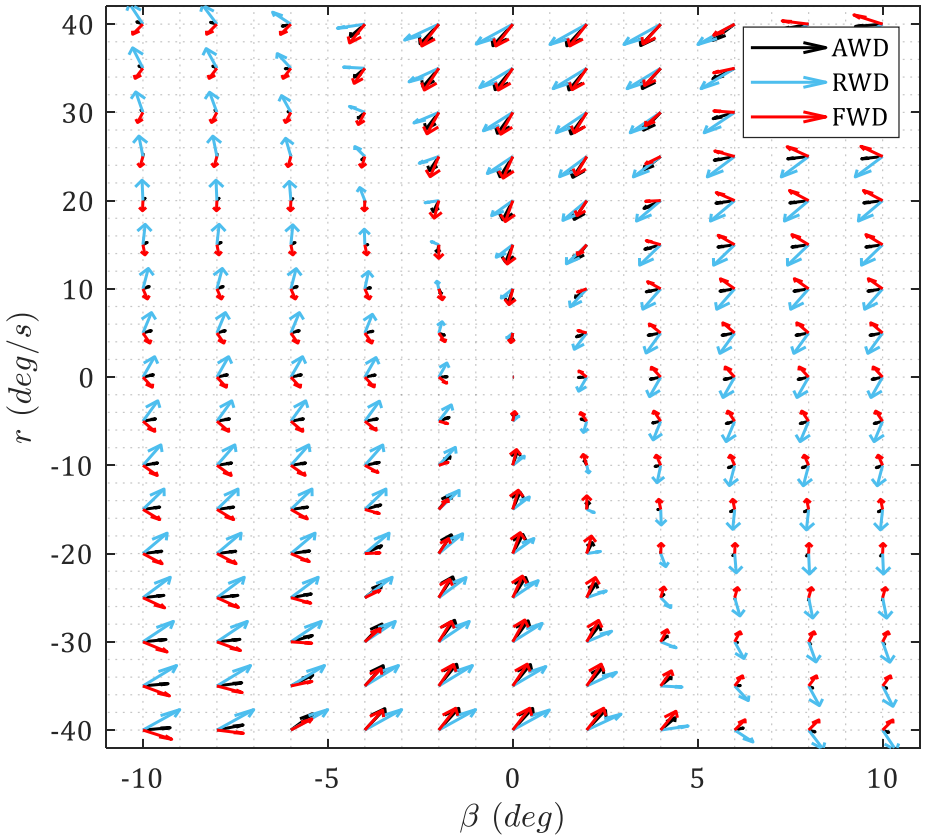

Figure 4-8. Drive torque effect on vector field, $v_{x,0} = 10$ m/s, $\mu = 0.55$, $\delta = 0$, and $T = 1500$ Nm

4.3. Optimal Axial Torque Distribution

The torque distribution presented in section 4.1 was based on the dynamic square. Since in drawing the dynamic square steering angle and lateral normal load transfers were not considered, this method is not an accurate solution. For instance, when a car is cornering at its limits of handling, the steering input should not be neglected. Also, the high lateral acceleration would cause a huge amount of lateral normal load transfer. This can change the normal load transfer balance and the dynamic square assumptions are not valid anymore. Therefore, the optimal torque distribution defined based on the dynamic square must be modified with accurate and realistic assumptions. In the following sections, the modified optimal torque distribution for a system with front and rear open differential axles are presented.

Assuming a quasi-steady state cornering condition, the dynamic equations of motion previously defined in Eqs. (4-6) and (4-7) are rewritten for a vehicle with an AWD drivetrain and front-wheel steering system moving on a flat road and shown as follow:

$$\cos(\delta_f)\left(F_{yfr}+F_{yfl}\right)+\sin(\delta_f)\left(F_{xfr}+F_{xfl}\right)+F_{yrr}+F_{yrl}=m\,a_y \tag{4-13}$$

$$l_f\left(\cos(\delta_f)\left(F_{yfr}+F_{yfl}\right)+\sin(\delta_f)\left(F_{xfr}+F_{xfl}\right)\right)-l_r\left(F_{yrr}+F_{yrl}\right)=0 \tag{4-14}$$

As explained before, the maximum lateral grip can be reached when the yaw moment acting on the vehicle is $M_Z=0$. The maximum lateral grip is redefined as:

$$\begin{aligned} a_{y,lim}=\big(&F_{yfr,lim}\cos(\delta_{fr})+F_{yfl,lim}\cos(\delta_{fl})+F_{xfr}\sin(\delta_{fr})+F_{xfl}\sin(\delta_{fl})\\ &+F_{yrr,lim}+F_{yrl,lim}\big)/m \end{aligned} \tag{4-15}$$

In this equation, the maximum tire capacity in lateral force generation is defined based on the friction circle, and the normal loads are estimated based on Eqs. (3-22) - (3-25) which considers normal load transfer in longitudinal and lateral directions.

To find the precise torque distribution, which considers the combined slip effect of tire forces, steering angle, and load transfers, the Eqs. (4-14) and (4-15) must be solved, simultaneously. In order to find the optimal front and rear torque distributions, the nonlinear Eqs. (4-14) and (4-15) must first be linearized at the operating points. After linearization, the system of equations can be modeled with the state-space representation of a 2-DOF dynamical system with the inputs of the axial torques and the outputs of lateral grip and yaw moment acting on the vehicle.

4.3.1. State-Space Representation

In order to find the optimal solution, the equation of motions of the vehicle as well as lateral grip and yaw moment equations must be linearized at the operating points. The sets of equations used for this optimization are as follow:

$$\dot{\beta} = \frac{1}{mv_x}\left(F_{yfr}cos\delta + F_{yfl}cos\delta + F_{yrr} + F_{yrl} + F_{xfr}sin\delta + F_{xfl}sin\delta\right) - r \tag{4-16}$$

$$\dot{r} = \frac{l_f}{I_z}\left(F_{yfr}cos\delta + F_{yfl}cos\delta + F_{xfr}sin\delta + F_{xfl}sin\delta\right) - \frac{l_r}{I_z}\left(F_{yrr} + F_{yrl}\right) - \frac{d}{2I_z}sin\delta\left(F_{yfr} - F_{rfl}\right) \tag{4-17}$$

$$a_{y,lim} = \frac{1}{m}\left(\cos(\delta)\left(F_{yfr,lim} + F_{yfl,lim}\right) + \sin(\delta)\left(F_{xfr} + F_{xfl}\right) + F_{yrr,lim} + F_{yrl,lim}\right) \tag{4-18}$$

$$M_{z,lim} = l_f\left(\cos(\delta_{fr})\left(F_{yfr,lim} + F_{yfl,lim}\right) + \sin(\delta_{fr})\left(F_{xfr,lim} + F_{xfl,lim}\right)\right) - l_r\left(F_{yrr,lim} + F_{yrl,lim}\right) - \frac{d}{2}sin\delta\left(F_{yfr,lim} - F_{yfl,lim}\right) \quad (4\text{-}19)$$

The above nonlinear sets of equations must be linearized at the operating point. First of all, the main nonlinear elements of the equation set, the lateral forces, are linearized as following [98]:

$$F_{yij}(\alpha_{ij}) = F_{yij}(\bar{\alpha}_{ij}) + \left.\frac{\partial F_{yij}}{\partial \alpha_{ij}}\right|_{\alpha_{ij}=\bar{\alpha}_{ij}} (\alpha_{ij} - \bar{\alpha}_{ij}) \quad (4\text{-}20)$$

where F_{yij} is defined as Eq. (3-18) and $\bar{\alpha}_{ij}$ is the tire side slip angle at each corner of the vehicle at the operating point. The linearized form of the lateral force can be rewritten as:

$$F_{yij} = \bar{C}_{\alpha ij}\alpha_{ij} + \bar{F}_{yij} \quad (4\text{-}21)$$

where $\bar{F}_{yij}$ includes all the constant parts of the Eq. (4-20) and $\bar{C}_{\alpha_{ij}}$ is defined as:

$$\bar{C}_{\alpha_{ij}} = \begin{cases} \left.\frac{\partial F_{yij}}{\partial \alpha_{ij}}\right|_{\alpha_{ij}=\bar{\alpha}_{ij}} & |\alpha_{ij}| < \alpha_{lim} \\ 0 & |\alpha_{ij}| > \alpha_{lim} \end{cases} \quad (4\text{-}22)$$

where α_{lim} is defined as Eq. (3-16). The other nonlinear elements in the set of Eqs. (4-16) to (4-19), are the maximum lateral forces, $F_{yij.lim}$ which are defined based on the friction circle theory as:

$$F_{yij,lim} = \sqrt{\mu^2 F_{zij}^2 - F_{xij}^2} \tag{4-23}$$

The maximum lateral force is linearized at the operating point as:

$$\begin{aligned} F_{yij,lim}(T_f, T_r) = F_{yij,lim}(\bar{T}_f, \bar{T}_r) + \left.\frac{\partial F_{yij.lim}}{\partial T_f}\right|_{\substack{T_f=\bar{T}_f \\ T_r=\bar{T}_r}} (T_f - \bar{T}_f) \\ + \left.\frac{\partial F_{yij.lim}}{\partial T_r}\right|_{\substack{T_f=\bar{T}_f \\ T_r=\bar{T}_r}} (T_r - \bar{T}_r) \end{aligned} \tag{4-24}$$

where $\bar{T}_f$ and $\bar{T}_r$ are the respective front and rear axial torques at the operating point, and T_f and T_r are the corresponding front and rear axle torque inputs of the system that need to be optimized. Eq. (4-24) can be simplified as:

$$F_{yij,lim} = \bar{C}_{fij} T_f + \bar{C}_{rij} T_r + \bar{F}_{yij,lim} \tag{4-25}$$

where $\bar{C}_{fij}$ and $\bar{C}_{rij}$ are the derivatives of maximum lateral force with respect to the front and rear axial torques, respectively. $\bar{F}_{yij,lim}$ contains all the constant parts of the linearized Eq. (4-24).

By substituting Eqs. (4-21) and (4-25) into Eqs. (4-16) to (4-19), the following state-space model can be written:

$$\dot{x} = Ax + Bu + d_x \tag{4-26}$$

$$y = Cx + Du + d_y \tag{4-27}$$

where x is the vector of states defined as:

$$x = [\beta \quad r]^{\mathrm{T}} \tag{4-28}$$

The outputs of the system are the maximum lateral acceleration and total yaw moment acting on the vehicle:

$$y = [a_{y,lim} \quad M_{z,lim}]^{\mathrm{T}} \tag{4-29}$$

and u is the input vector as:

$$u = [T_f \quad T_r]^{\mathrm{T}} \tag{4-30}$$

The matrix A is defined as:

$$A = \begin{bmatrix} A_{11} & A_{12} \\ A_{21} & A_{22} \end{bmatrix} \tag{4-31}$$

where A_{11}, A_{12}, A_{21}, and A_{22} are as follow:

$$A_{11} = \frac{cos\delta\left(\bar{C}_{\alpha fr} + \bar{C}_{\alpha fl}\right) + \bar{C}_{\alpha rr} + \bar{C}_{\alpha rl}}{mv_x} \tag{4-32}$$

$$A_{12} = \frac{l_f cos\delta\left(\bar{C}_{\alpha fr} + \bar{C}_{\alpha fl}\right) - l_r\left(\bar{C}_{\alpha fr} + \bar{C}_{\alpha fl}\right)}{mv_x^2} - 1 \tag{4-33}$$

$$A_{21} = \frac{l_f cos\delta\left(\bar{C}_{\alpha fr} + \bar{C}_{\alpha fl}\right) - l_r\left(\bar{C}_{\alpha fr} + \bar{C}_{\alpha fl}\right) + \frac{d}{2} sin\delta\left(\bar{C}_{\alpha fl} - \bar{C}_{\alpha fr}\right)}{I_z} \tag{4-34}$$

$$A_{22} = \frac{l_f^2 cos\delta\left(\bar{C}_{\alpha fr} + \bar{C}_{\alpha fl}\right) + l_r^2\left(\bar{C}_{\alpha fr} + \bar{C}_{\alpha fl}\right) + \frac{d}{2} l_f sin\delta\left(\bar{C}_{\alpha fl} - \bar{C}_{\alpha fr}\right)}{I_z v_x} \tag{4-35}$$

Also, the two matrices B and C are defined as:

$$B = \begin{bmatrix} \frac{sin\delta}{m v_x R_{eff}} & 0 \\ \frac{l_f sin\delta}{I_z R_{eff}} & 0 \end{bmatrix} \tag{4-36}$$

$$C = \begin{bmatrix} 0 & 0 \\ 0 & 0 \end{bmatrix} \tag{4-37}$$

Furthermore, the matrix D is defined as:

$$D = \begin{bmatrix} D_{11} & D_{12} \\ D_{21} & D_{22} \end{bmatrix} \tag{4-38}$$

where the matrix elements D_{11}, D_{12}, D_{21}, and D_{22} are defined as:

$$D_{11} = \frac{1}{m}\left(cos\delta\left(\bar{C}_{f,fr} + \bar{C}_{f,fl}\right) + \frac{sin\delta}{R_{eff}}\right) \tag{4-39}$$

$$D_{12} = \frac{1}{m}\left(\bar{C}_{r,rr} + \bar{C}_{r,rl}\right) \tag{4-40}$$

$$D_{21} = l_f\left(cos\delta\left(\bar{C}_{f,fr} + \bar{C}_{f,fl}\right) + \frac{sin\delta}{R_{eff}}\right) + \frac{d}{2}sin\delta\left(\bar{C}_{f,fl} - \bar{C}_{f,fr}\right) \tag{4-41}$$

$$D_{22} = -l_r\left(\bar{C}_{f,rr} + \bar{C}_{f,rl}\right) \tag{4-42}$$

It should be noted that the state-space model is a linear parameter varying and the model parameters are updated at each time step.

4.3.2. Actuation Dynamics

The time delay between the actuation torque command and the actual torque applied to the front axle is considered in this study as a first-order dynamic delay as:

$$T_i = \frac{1}{1+\tau s}T_{i,in} \tag{4-43}$$

where $T_{i,in}$ is the actuator command, and τ is the electric motors' time delay. Eq. (4-43) can be rewritten in the following form as:

$$\begin{bmatrix}\dot{T}_f \\ \dot{T}_r\end{bmatrix} = \underbrace{\begin{bmatrix}-\frac{1}{\tau} & 0 \\ 0 & -\frac{1}{\tau}\end{bmatrix}}_{A_u}\begin{bmatrix}T_f \\ T_r\end{bmatrix} + \underbrace{\begin{bmatrix}\frac{1}{\tau} & 0 \\ 0 & \frac{1}{\tau}\end{bmatrix}}_{B_u}\begin{bmatrix}T_{f,in} \\ T_{r,in}\end{bmatrix} \tag{4-44}$$

By considering the actuator dynamic in the state space form of (4-44), one can reformulate the state-space system defined as Eqs. (4-26) and (4-27) in the form of a new state-space form with four states of the yaw rate, sideslip angle, and the actual front and rear axle torques. Therefore, the new state-space model is defined as:

$$\dot{X} = \bar{A}X + \bar{B}U + \bar{d}_x \tag{4-45}$$

$$Y = \bar{C}X + \bar{d}_y \tag{4-46}$$

where

$$\bar{A} = \begin{bmatrix} A & B \\ 0_{2\times2} & A_u \end{bmatrix} \tag{4-47}$$

$$\bar{B} = \begin{bmatrix} 0_{2\times2} \\ B_u \end{bmatrix} \tag{4-48}$$

$$\bar{C} = [C \quad D] \tag{4-49}$$

$$\bar{d}_x = \begin{bmatrix} d_x \\ 0_{2\times1} \end{bmatrix} \tag{4-50}$$

and

$$\bar{d}_y = d_y \tag{4-51}$$

The state-space represented in Eqs. (4-45) and (4-46) is in the continuous-time domain and must be discretized before any optimization progress. The step-invariant method is applied to discretize the continuous-time model. Assuming the discrete-time period as $t_k \leq t < t_{k+1}$, with the sample time ofT_s, the discrete-time state-space model is defined as:

$$X_{k+1} = \bar{A}_d X_k + \bar{B}_d U_k + \bar{d}_{xd} \tag{4-52}$$

$$Y_k = \bar{C}_d X_k + \bar{d}_{yd} \tag{4-53}$$

where the augmented model matrices are $\bar{A}_d = e^{\bar{A}(t)T_s}$, $\bar{B}_d = \int_0^{T_s} e^{\bar{A}(t)\tau}\bar{B}(t)d\tau$, $\bar{d}_d = \int_0^{T_s} e^{\bar{A}(t)\tau}\bar{d}(t)d\tau$, $\bar{C}_d = \bar{C}$, and $\bar{d}_{yd} = \bar{d}_y$.

4.3.3. Performance Index

To find the optimal values of the system inputs, the following objective function is defined:

$$J = \|W_{2\times2}(Y - Y_{des})\|^2 + \|R_{2\times2}U\|^2 \tag{4-54}$$

where, W is the outputs weight matrix and R is the input weight matrix. In addition, desired values shown by Y_{des} should be defined for the optimizer. Based on the optimal torque distribution theory explained in the previous section, the desired yaw moment for maximizing the lateral grip should be zero. Also, the desired value for maximum lateral acceleration is defined based on the friction circle theory as follows:

$$a_{y,max} = \sqrt{\mu^2 g^2 - a_x^2} \tag{4-55}$$

4.3.4. Constraints

The solution to the optimization problem needs to be bounded by the total torque requested by the driver. Also, the torque command to both front and rear axles are assumed to be positive and no negative torque (breaking) is acceptable in this study. In addition to the driver torque command, the tire capacities restrict the optimization problem. Therefore, the optimization must find the optimal front and rear axial torque values such that they satisfy the following constraints:

Input Equality Constraint

$$T_f + T_r = T \tag{4-56}$$

Input Inequality Constraints

$$0 \leq T_f \leq 2\mu R_{eff} \min\left(F_{zfr}, F_{zfl}\right) \tag{4-57}$$

$$0 \leq T_r \leq 2\mu R_{eff} \min(F_{zrr}, F_{zrl}) \tag{4-58}$$

State Variable Constraints:

The other sets of constraints are stability constraints defined based on the safe envelope defined in the previous chapter. The boundaries for the yaw rate of the vehicle are located on the line of maximum and minimum steady-state yaw rate as follows:

$$r_{max} = +\frac{\mu g}{v_x} \tag{4-59}$$

$$r_{min} = -\frac{\mu g}{v_x} \tag{4-60}$$

$$\beta_{max} = \frac{l_r r}{v_x} + tan(\alpha_{lim}) \tag{4-61}$$

$$\beta_{min} = \frac{l_r r}{v_x} - tan(\alpha_{lim}) \tag{4-62}$$

Therefore, the constraints on the state variables are defined as:

$$\begin{bmatrix} \beta_{min} \\ r_{ss,min} \end{bmatrix} \leq \begin{bmatrix} \beta \\ r \end{bmatrix} \leq \begin{bmatrix} \beta_{max} \\ r_{ss,max} \end{bmatrix} \tag{4-63}$$

4.3.5. Quadratic Programing Problem

In order to minimize the performance index introduced in Eq. (4-54), the optimal input values of front and rear axial torques must be found by an optimization solver while satisfying all constraints introduced in Eqs. (4-56) to (4-63). The performance index J and constrains are rewritten in form of a quadratic problem as follow:

$$\begin{aligned} &\min J = \frac{1}{2}\boldsymbol{U}^T H \boldsymbol{U} + f\boldsymbol{U} \\ &subject\ to\ LB \leq \boldsymbol{U} \leq UB \end{aligned} \tag{4-64}$$

where LB and UB are abbreviated as the constraints of the lower bound and the upper bound, respectively. Also, the matrices H and f are defined as:

$$H = 2((\bar{C}_d \bar{B}_d)^T W (\bar{C}_d \bar{B}_d) + R) \tag{4-65}$$

$$f = 2\left(X_k^T(\bar{C}_d\bar{A}_d)^T + (\bar{C}_d\bar{A}_d)^T\bar{d}_{xd}^T + \bar{d}_{dy}^T - Y_{des}\right)W\bar{C}_d\bar{B}_d \tag{4-66}$$

4.3.6. Feedforward Axial Torque Distribution Controller

In this section, a feedforward controller is designed based on the optimal torque distribution algorithm that receives the steering and torque commands from the driver and delivers the optimal torque values to each of the axles. The general structure of the controller is shown in Figure 4-9.

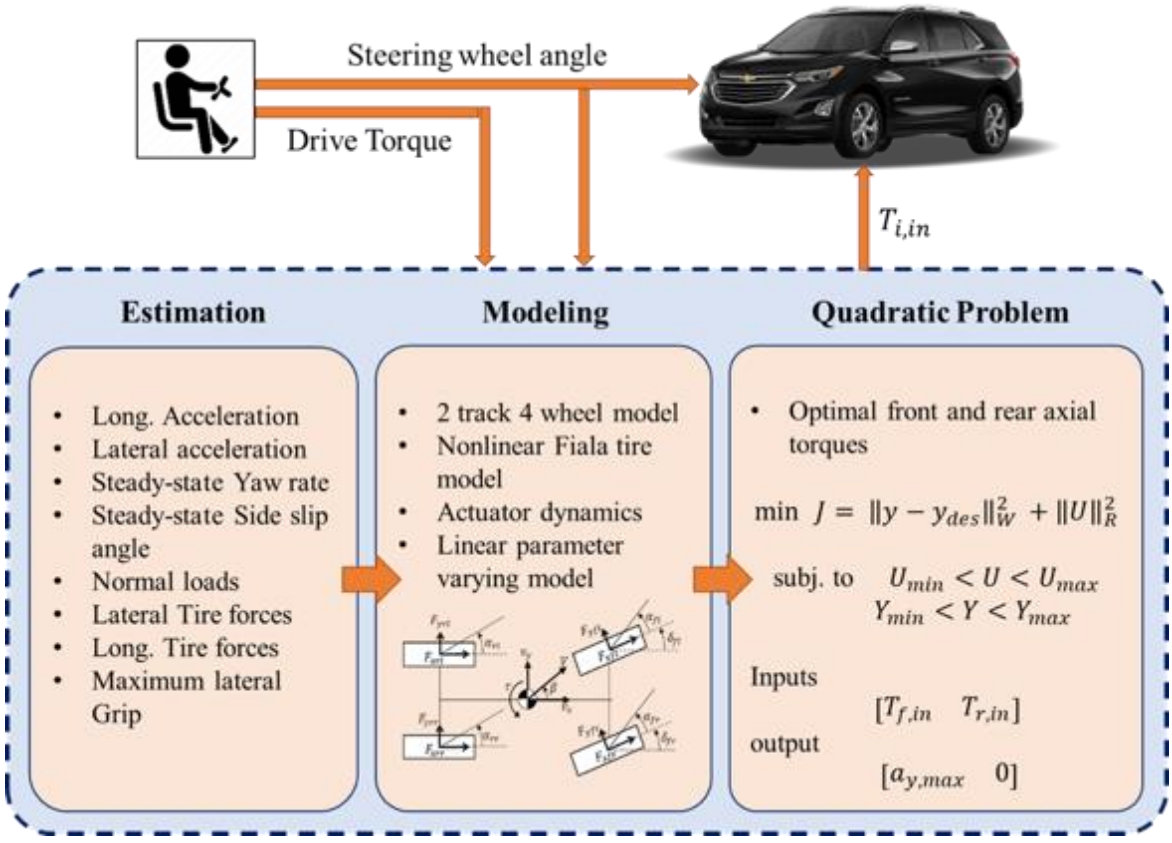

Figure 4-9. Feedforward optimal torque distributor architecture

The algorithm is simulated and verified in a CarSim® simulation environment and tested on a real vehicle for different driving scenarios during different road conditions. The algorithm does not control any yaw rate and sideslip angle due to its feedforward nature. To understand the importance of the feedforward optimal torque distribution, it is necessary to verify it without the interaction of any other controllers. The simulation results are presented and explained in the next section.

4.3.7. Simulation Results

In this section, the feedforward controller is applied to a high-fidelity vehicle model in the CarSim software. A verified high-fidelity CarSim model of a Chevrolet Equinox has been developed in the Mechatronic Vehicle Systems lab at the University of Waterloo and is used for CarSim simulations in this section. The CarSim simulation creates the opportunity of fast tuning, calibrating, and verifying the proposed controller before testing it on the real vehicle. To do so, the Equinox CarSim model is integrated with the proposed algorithm coded in MATLAB. The steering angle and the total torque are fed into the model as the driver inputs and the torque distribution to the front and rear axles are adjusted by the feedforward controller. The CarSim model parameters of the Chevrolet equinox used for the simulations are presented in Table 4-1.

The results obtained based on the optimal torque distribution (OPT TD) are compared with the baseline models with constant torque distribution as well as optimal torque distribution based on the dynamic square (DS). The controller performance is investigated for two different driving scenarios under two different road conditions.

Table 4-1. *Physical parameters of the vehicle used for CarSim® simulations*

Parameter	***Value***	***Parameter***	***Value***
$m\ (kg)$	*2271.62*	$R_{eff}\ (m)$	*0.351*
$I_z\ (kg.m^2)$	*4600*	$h\ (m)$	*0.64*
$l_f\ (m)$	*1.4212*	$d\ (m)$	*1.60*
$l_r\ (m)$	*1.4337*		

4.3.7.1. Acceleration in Turn on Wet Road

An acceleration in turn is performed in this section to study the vehicle performance under the optimal torque distribution. It is assumed that a total torque with a maximum value of $2500\ Nm$ and a steering wheel angle with a profile shown in Figure 4-10 is applied as the driver's inputs. The road is assumed to be wet with a friction coefficient $\mu = 0.50$. Output axle torques obtained from the optimal torque distribution algorithm is presented in Figure 4-11. This optimal torque distribution tries to maximize the vehicle's lateral grip. The lateral accelerations are plotted in Figure 4-12. This figure plots the lateral accelerations of four simulations with different torque distribution strategies. The red line with the circle marker belongs to the simulation with torque distribution defined based on the dynamic square method (DS). This method will distribute the torque based on the parameter ratiol_r/l_f. Since this parameter for the selected vehicle is close to 1, the torque distribution from DS method acts close to an AWD vehicle with constant torque distribution of 50-50.

Another simulation is performed with the total torque sent to the front axle (FWD). The lateral acceleration related to the FWD torque distribution is not even close to the maximum lateral acceleration. Black dashed lines show the maximum lateral acceleration that could ideally be reached during this scenario. This maximum lateral acceleration is calculated based on Eq. (4-55). In the other simulation, all toque is sent to the rear axle (RWD). The lateral acceleration during this scenario is high at the beginning of applying the steering angle, but soon the vehicle becomes unstable. This behavior was previously predicted by the sensitivity analysis performed on the phase plane. Sending the torque to the rear axle makes the safe envelope smaller resulting in vehicle instability. Finally, the simulation with feedforward optimal torque distribution (OPT TD) is performed. The black line with square markers shows the lateral acceleration resulted from optimal torque distribution. The feedforward optimal torque distribution resulted in the highest value of the lateral acceleration compared to the three other simulations.

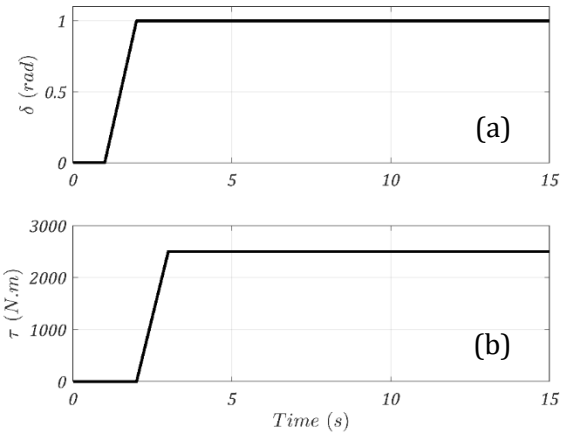

Figure 4-10. Driver Input for slalom on wet road: (a) steering wheel angle, (b) total torque

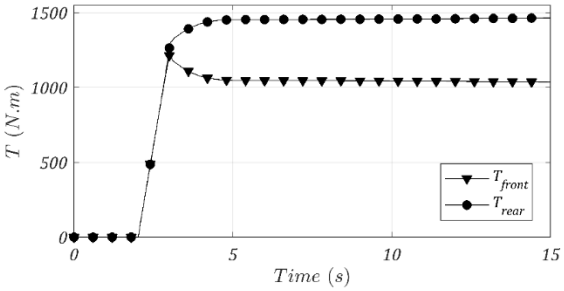

Figure 4-11. Optimal torque distribution to the front and rear axles for step steer scenario on dry road

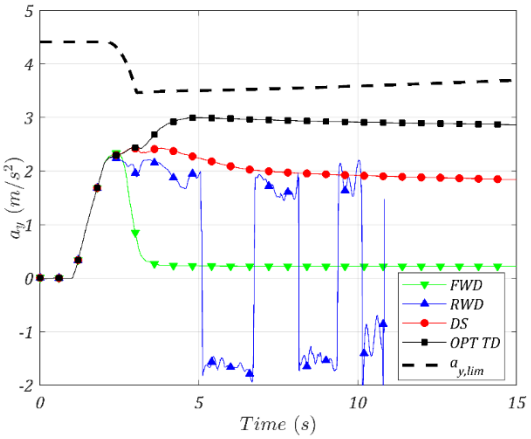

Figure 4-12. Effect of optimal torque distribution on lateral acceleration ($\mu = 0.50$, $v_{x,0} = 40$ km/h)

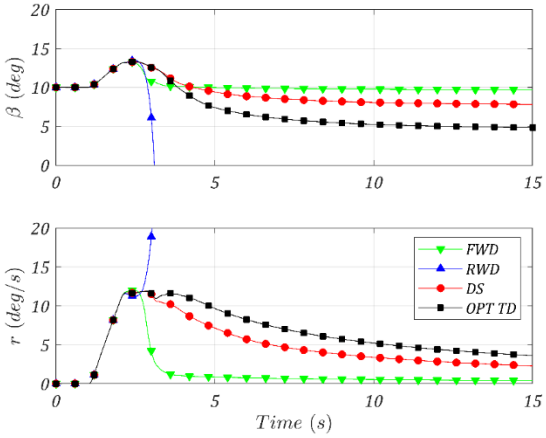

Figure 4-13. Torque distribution effect on sideslip angle, and yaw rate. ($\mu = 0.50$, $v_{x,0} = 40$ km/h)

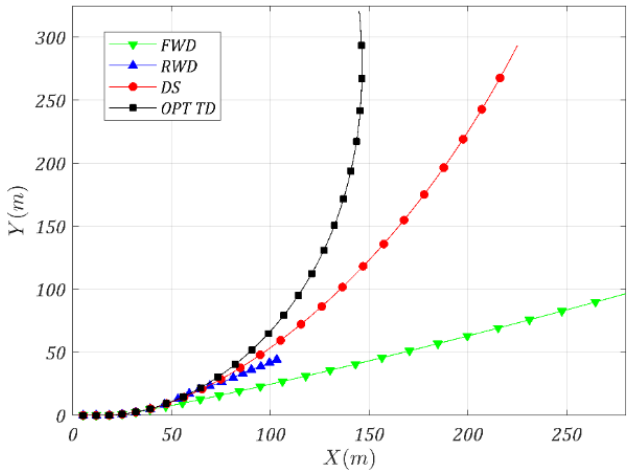

Figure 4-14. Torque distribution effect on vehicle trajectory. ($\mu = 0.50$, $v_{x,0} = 40$ km/h)

Having higher lateral acceleration and using the maximum possible vehicle grip in both longitudinal and lateral directions let the vehicle perform a better turn while accelerating. Figure 4-13 shows the vehicle yaw rate and sideslip angle during the acceleration in turn maneuver on the wet road with four different torque distribution. It can be seen that FWD torque distribution makes the vehicle understeers, while the RWD one makes it extremely oversteer and eventually unstable. The DS method performs a better maneuver compares to the FWD and RWD, but the feedforward OPT TD has the best cornering performance compared to all the three.

To better understand the effect of optimal torque distribution, vehicle trajectories during simulations are plotted in Figure 4-14. It is shown in this figure that FWD torque allocation is extremely understeer while RWD torque allocation makes the vehicle too oversteer. Due to the highly oversteer behavior of the RWD vehicle, it gets unstable as soon as the steering is applied. When the RWD got unstable, the simulation stopped and the maneuver could not be finished. The results of this section clearly showed that the optimal torque distribution performed the best acceleration in turn with sharper turning compared to all other simulations.

4.3.7.2. Lane Change on Dry Wet Road

Another driving scenario simulated on a wet road is a lane change. The steering wheel angle and driver torque input shown in Figure 4-15 are applied in four simulations with different torque allocations. FWD, RWD, torque distribution from Dynamic Square method (DS), and the optimal torque distribution (OPT TD) are applied to the CarSim® high fidelity model. The initial longitudinal speed is chosen as $v_{x,0} = 40\ km/h$, and the friction coefficient as 0.50. The optimal torque distribution to the axles is plotted in Figure 4-16. The comparison between the different toque distribution methods is shown in Figure 4-17 to Figure 4-19. As explained in the previous section, the optimal torque distribution lets the vehicle perform a better turn during acceleration. This scenario performs a lane change during acceleration. As shown in Figure 4-19, the only simulation that was capable of performing the lane change perfectly was the one with the feedforward optimal torque distribution.

Comparing the lateral accelerations in the performed simulations, Figure 4-17, the OPT TD has the highest values during the moments steering angle is maximum. The optimal torque distribution would let the vehicle have its maximum lateral grip at all times. When the steering is applied and a sharp turn is required, the lateral grip available would let the vehicle have enough capacity in lateral force generation to perform the turning with the best performance possible.

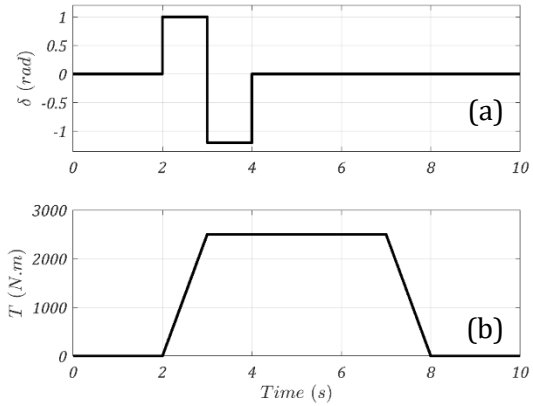

Figure 4-15. Driver Input for double lane change on dry road: (a) steering wheel angle, (b) total torque

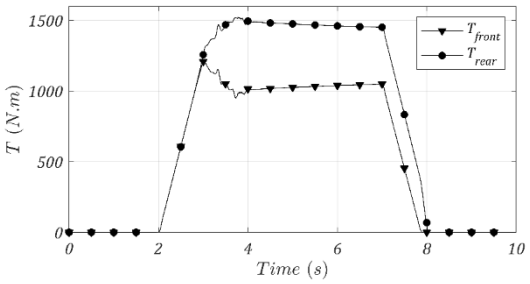

Figure 4-16. Optimal torque distribution to the front and rear axles for double lane change scenario on dry road

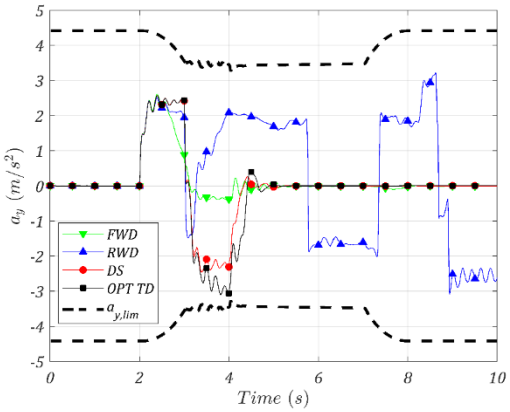

Figure 4-17. Effect of optimal torque distribution on lateral acceleration ($\mu = 0.50$, $v_{x,0} = 40\ km/h$)

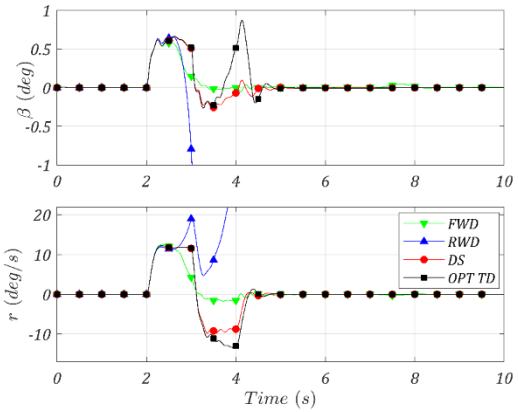

Figure 4-18. Torque distribution effect on sideslip angle, and yaw rate. ($\mu = 0.50$, $v_{x,0} = 40\ km/h$)

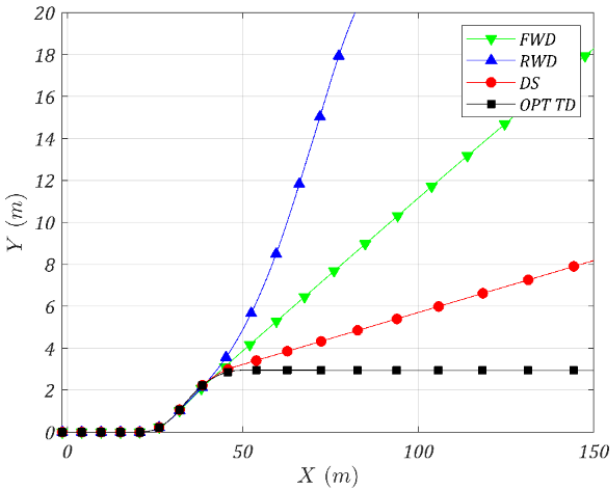

Figure 4-19. Torque distribution effect on sideslip angle, and yaw rate. ($\mu = 0.50$, $v_{x,0} = 40\ km/h$)

4.3.7.3. Sinusoidal Maneuver on Dry Road

The third driving scenario is a sinusoidal maneuver on a dry road. The steering wheel profile and driver's torque input are shown in Figure 4-20. The total torque requested by the driver is $4200\ (N.m)$. The initial speed of the vehicle is $v_{x,0} = 40\ km/h$ and the road friction coefficient is $\mu = 0.85$. The simulation is performed with four different torque distributions. The first simulation is an FWD system. The lateral acceleration related to this simulation is too low and close to 0. The second simulation is performed on an RWD system. This simulation has a high value of lateral acceleration compared to the FWD one but gets unstable. As explained before in the sensitivity analysis on phase plane and previous driving scenarios, the RWD torque distribution increases the chance of instability and needs a stability controller to stabilize it. This is while having an optimal torque distribution enhances the stability of the vehicle. The third simulation distributes the torque according to the dynamic square formulation. This method results in a higher value of lateral acceleration compared to the FWD and better stability compared to the RWD. The lateral acceleration of the dynamic square method is still lower than optimal feedforward torque distribution.

The torque distribution obtained from the feedforward optimal toque distribution is shown in Figure 4-21. A shown, the total optimal torque has a 10% average reduction. This reduction increases the longitudinal force generation capacity of the axles. The advantage of this torque reduction is that it would let the vehicle have a higher lateral grip. This happens due to the combined effect of the slip ratio. By reducing the longitudinal force by 5 to 10%, the lateral grip could increase up to 45% which, would effectively increase the vehicle steerability during harsh maneuvers. In addition, due to the open differential assumption of the axles, the inner tires with higher slip ratio and lower force capacity determines the maximum torque allowable on each axle. Therefore, by applying the steering angle during harsh cornering maneuvers, the total torque allowed by the controller reduces to lower values. The maximum value of this torque reduction is happening at the time of 3s and 4.5 s. This reduction means that both axles were saturated and adding more torque to any of them would result in a high slip ratio and energy loss. A higher slip ratio would drop the tire capacity in lateral force generation and will not let the vehicle use its maximum lateral grip. The feedforward optima torque distributor is designed in a way that not only pushes the axles to the handling limits but also keeps them at the limits. This means that if any of the tires of the axle is reached the handling limit, no more torque will send to

that axle. Therefore, the algorithm has reduced the torque applied to the tries to keep the axles at their limits of handling that would let the vehicle use its maximum lateral grip.

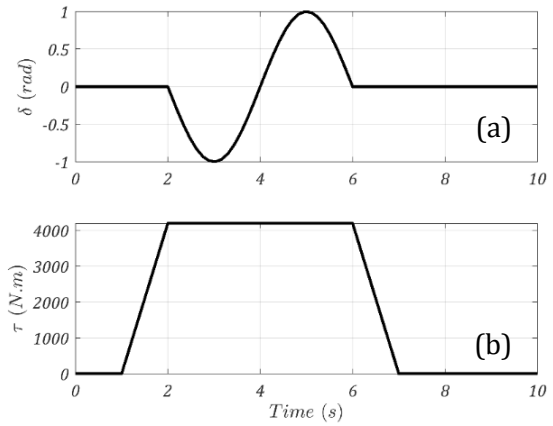

Figure 4-20. Driver Input for double lane change on dry road: (a) steering wheel angle, (b) total torque

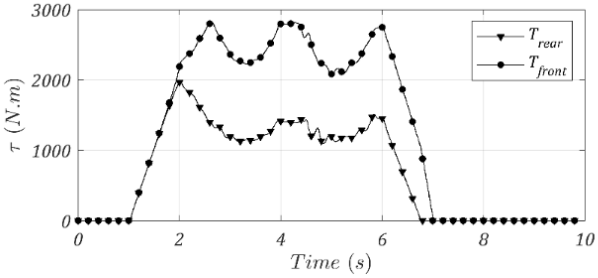

Figure 4-21. Optimal torque distribution to the front and rear axles for double lane change scenario on dry road

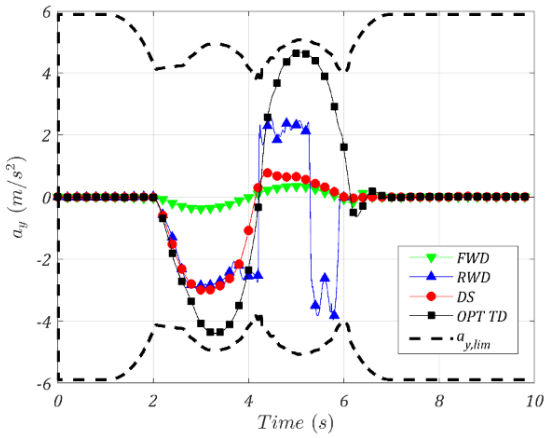

Figure 4-22. Effect of optimal torque distribution on lateral acceleration ($\mu = 0.85$, $v_{x,0} = 40\ km/h$)

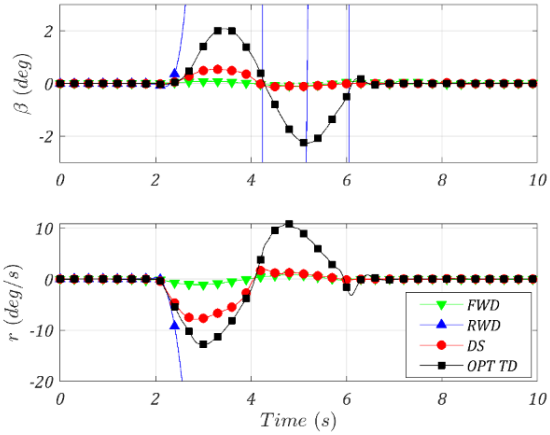

Figure 4-23. Torque distribution effect on sideslip angle, and yaw rate. ($\mu = 0.85$, $v_{x,0} = 40\ km/h$)

The maximum achievable lateral grip is shown with black dashed lines in Figure 4-22. The black line with square markers in this figure shows the measured lateral acceleration while the feedforward controller was on. The red line with circle markers shows the lateral acceleration of the simulation performed with the dynamic square method of torque distribution. Having optimal torque distribution would let the vehicle to use its maximum capacity in both longitudinal and lateral directions and reach higher lateral acceleration during cornering maneuvers.

The effect of torque distribution on the sideslip angle and yaw rate of the vehicle is shown in Figure 4-23. It is clear that while the torque distribution is being optimized, the sideslip angle and yaw rate reach higher values but remain in the stable zone. Having a higher yaw rate and sideslip angle would let the vehicle perform sharper turns. The vehicle is highly understeer when the torque distribution is constant FWD, and RWD torque distribution makes the vehicle highly oversteer and eventually unstable. The vehicle has a better steering response when the optimal torque distribution is applied to the system. Therefore, instead of having understeer or unstable behavior for the vehicle with constant torque distributions, one could have a performance with high steerability and better turning maneuverability while remaining stable.

4.3.8. Experimental Results

In order to evaluate the algorithm performance, the feedforward controller is tested on a vehicle experimentally. Although the proposed controller was successfully verified on the CarSim simulations, the controller must also be verified through experimental tests. When a vehicle is driven on a test track, many disturbances can affect the performance of the control system. Some of the most common disturbances are due to the road uncertainties, such as the variations of the road surface friction coefficient and the tire uncertainties such as the tire erosion, and/or tire pressure variation. Therefore, it is highly necessary to perform tests of the controller experimentally. Experimental road tests can verify the controller performance and its robustness to different disturbances.

An AWD GM Chevrolet Equinox with four independent electric motors at each corner is used for the experimental tests. The algorithm is designed in the MATLAB/Simulink platform and connected to the vehicle through a dSPACE MicroAutobox with the sampling time $5\,ms$. The dSPACE

communicates with the GPS unit, the Internal Measurement Unit (IMU), and the electric motors through the Control Area Network (CAN). The vehicle longitudinal and lateral velocities are measured with the GPS unit. The vehicle lateral acceleration is measured with the IMU sensor. The CAN bus delivers the requested torque command to the electric motors. The vehicle equipped with the feedforward controller is tested on the test track. Two driving scenarios are tested and results are presented in the next sections.

4.3.8.1. Acceleration in turn on dry road

An acceleration in turn driving scenario is performed on a dry road. In the first test, the vehicle was adjusted to an AWD drivetrain configuration with a constant 50-50 torque distribution to each axle. It was assumed that both axles are open differential and the same torque goes to the left and right wheels on each axle. For the second test, the wheel torques were controlled with the optimal torque distribution algorithm. Since it was assumed the axles are open differential, the optimized axle torques were equally divided between left and right wheels. To perform this scenario, the driver applied a constant steering wheel angle and started the engine at full throttle. The steering wheel angle and torque commands are shown in Figure 4-24. The red lines with circle markers show the measurement of the first test with the 50-50 AWD configuration and the black lines with square markers show the measured signals from the second test with optimal torque distribution.

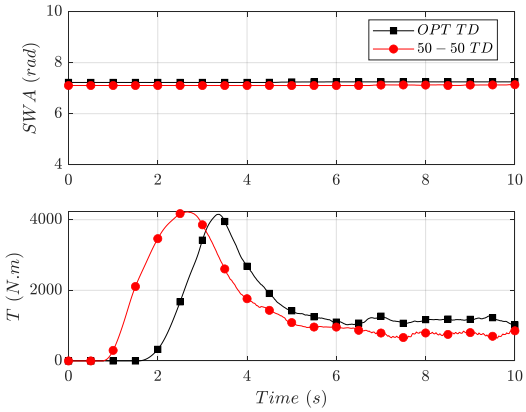

Figure 4-24. Driver Input for acceleration in turn on dry road: (a) steering wheel angle, (b) total torque

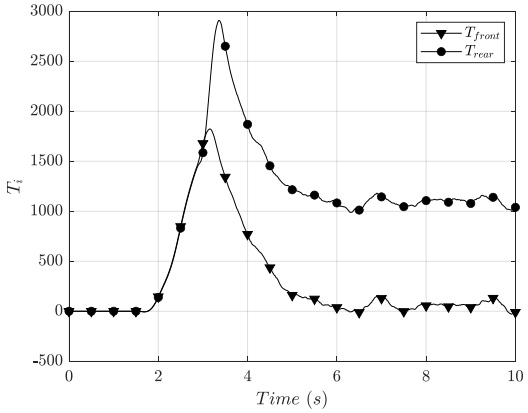

Figure 4-25. Optimal torque distribution to the front and rear axles for acceleration in turn on dry road

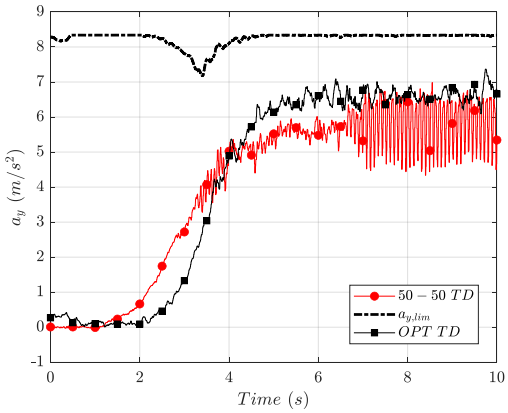

Figure 4-26. Effect of optimal torque distribution on lateral acceleration

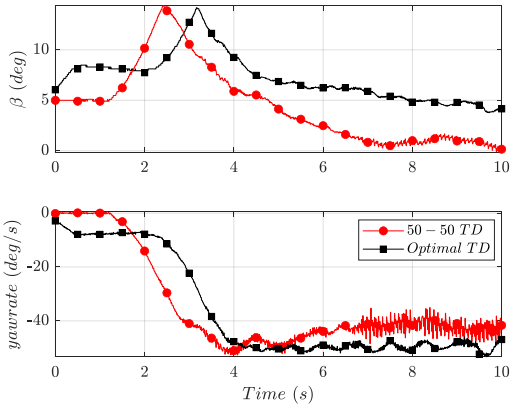

Figure 4-27. Torque distribution effect on sideslip angle, and yaw rate

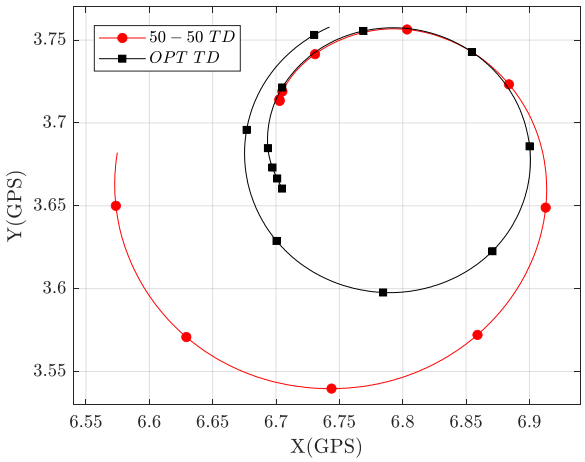

Figure 4-28. Vehicle trajectory

Figure 4-25 shows the optimized axle torques sent to the front and rear axles of the vehicle during the second test. It can be seen the torque sent to the rear axle is higher than the front axle torque. As explained before, due to the normal load transfer during acceleration the estimated normal loads on the front tires are less than normal loads on the rear tires. Therefore, the front tires have less tire capacity compared to the rear ones. Therefore, the feedforward controller sent more torque to the rear axle. Lateral acceleration from both tests are compared in Figure 4-26 and the vehicle yaw rate and sideslip angles are shown in Figure 4-27. As shown in Figure 4-26, optimizing axle torques resulted in higher values of lateral acceleration and the vehicle could perform a better turn in acceleration, as shown in Figure 4-28.

In the AWD configuration, the front axle received torque values more than it can handle. The front inner tire did not have enough normal load acting on it and sending a quarter of the driver requested torque to this wheel resulted in a high slip ratio on this tire. The front inner tire with a high slip ratio started to spin and made the vehicle shaking with high frequency. At the same time, the high slip ratio drastically dropped lateral force acting on the front inner tire. Therefore, the lateral acceleration had a lower value and the vehicle could not perform the desired turn.

4.3.8.2. Lane change on the wet road

The second scenario performed on the Chevrolet Equinox was a lane change on the wet road. Two drivetrains, an RWD powertrain, and the optimized axle torque distribution were tested separately with similar driver's input on the wet road. The driver's inputs are shown in Figure 4-29. The optimized torques to the front and rear axles are presented in Figure 4-30. As can be seen in this figure, the axle torques are reduced as the steering is applied. The feedforward controller considers the tire capacities in force generation to prevent sending any torque more than a tire can handle. Since the axles are open differential, the algorithm considers the tire with minimum force capacity.

Figure 4-32 compares the vehicle yaw rates and sideslip angles of both tests. With the RWD configuration, represented by red lines with circle markers, the vehicle got unstable the moment after applying the steering angle. As the vehicle got unstable, the driver tried to first reduce the input torque and applied a different steering angle than what was desired to bring back the vehicle to the stable zone. This is while wen axle torques were optimized, not only the vehicle remained stable, but also it could reach the maximum lateral acceleration during the test.

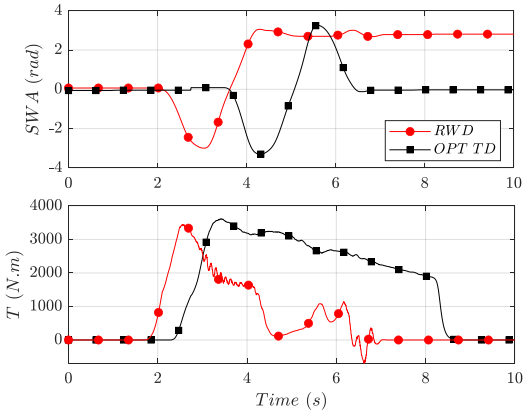

Figure 4-29. Driver Input for lane change on wet road: (a) steering wheel angle, (b) total torque

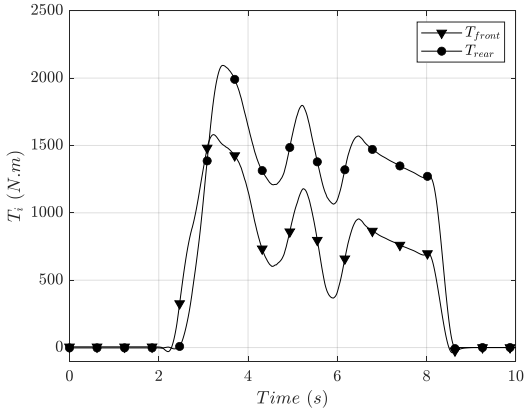

Figure 4-30. Optimal torque distribution to the front and rear axles for lane change scenario on wet road

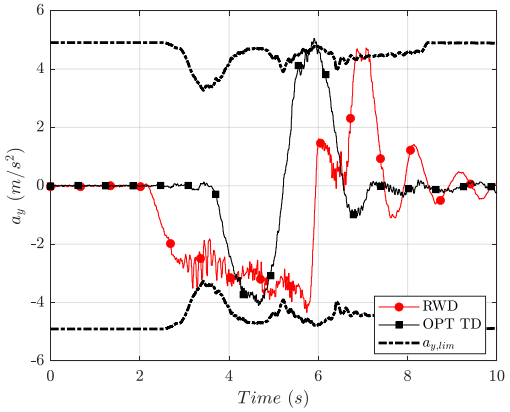

Figure 4-31. Effect of optimal torque distribution on lateral acceleration

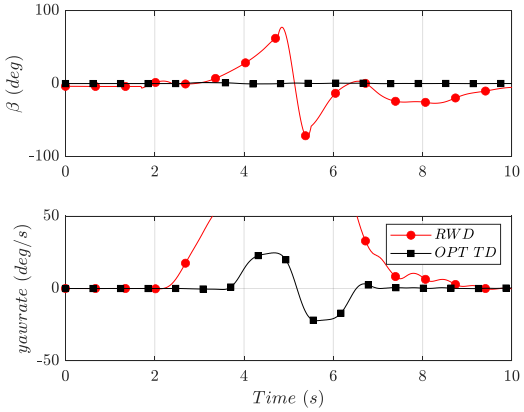

Figure 4-32. Torque distribution effect on sideslip angle, and yaw rate.

4.4. Optimal Corner Torque Distribution

The previous section perfectly cleared the importance of optimizing torque distribution for vehicles with open differential axials at the front and rear. However, when it comes to the electric vehicles with four independent electric motors, the torque distribution problem transforms into a corner-based optimization problem. A corner-base torque distribution problem is presented in this section and has been solved through a quadratic programming optimization solver. The developed optimizer is evaluated first in the MTLAB\CarSim simulation environment and then experimentally on an Electric Chevrolet Equinox.

4.4.1. State-Space Representation

In order to obtain the corner-based optimal torque distribution, a 2DOF vehicle dynamic model is introduced in section 4.3.1 as Eqs. (4-16) and (4-17) are used as the main equations of motion. The outputs of the system are maximum lateral grip and yaw moment of the vehicle at the limits of handling as defined in Eqs. (4-18) as (4-19), respectively. The Fiala tire model defined as Eq. (3-18) is used to capture tire model nonlinearities. To derive the state-space form of the dynamic system with four the

maximum lateral force defined as Eq. (4-23) is linearized with respect to the corner torques at the operating point as follow:

$$F_{yij}^{lim}(T_{ij}) = F_{yij}^{lim}(\bar{T}_{ij}) + \left.\frac{\partial F_{yij}^{lim}}{\partial T_{fr}}\right|_{T_{ij}=\bar{T}_{ij}} (T_{fr} - \bar{T}_{fr}) + \left.\frac{\partial F_{yij}^{lim}}{\partial T_{fl}}\right|_{T_{ij}=\bar{T}_{ij}} (T_{fl} - \bar{T}_{fl}) + \left.\frac{\partial F_{yij}^{lim}}{\partial T_{rr}}\right|_{T_{ij}=\bar{T}_{ij}} (T_{rr} - \bar{T}_{rr}) + \left.\frac{\partial F_{yij}^{lim}}{\partial T_{rl}}\right|_{T_{ij}=\bar{T}_{ij}} (T_{rl} - \bar{T}_{rl}) \tag{4-67}$$

where $\bar{T}_{ij}$ are the corners torque at the operating point and T_{ij} are the variables of the optimization problem. The Eq. (4-67) can be simplified as:

$$F_{yij}^{lim} = \bar{C}_{fr}T_{fr} + \bar{C}_{fl}T_{fl} + \bar{C}_{rr}T_{rr} + \bar{C}_{rl}T_{rl} + \bar{F}_{yij}^{lim} \tag{4-68}$$

where $\bar{C}_{ij}$ being the derivatives of the maximum lateral force with respect to the corner torque, and $\bar{F}_{ij}^{lim}$ contains all constant parts of the linearized Eq. (4-67).

Another nonlinear term is the nonlinear lateral forces defined based on the Fiala tire model. The linearized form of the lateral forces is defined as Eqs. (4-20) to (4-21).

To define the quadratic form of the vehicle dynamic system with four independent electric motors, the linearized system is written in the form of the state-space as follows:

$$\dot{x} = Ax + Bu + d_x \tag{4-69}$$

$$y = Cx + Du + d_y \tag{4-70}$$

where x is the vector of states defined as:

$$x = [\beta \quad r]^{\mathrm{T}} \tag{4-71}$$

The outputs of the system are maximum lateral acceleration and total yaw moment acting on the vehicle:

$$y = [a_{y,lim} \quad M_{z,lim}]^{\mathrm{T}} \tag{4-72}$$

and u is the input vector as:

$$u = [T_{fr} \quad T_{fl} \quad T_{rr} \quad T_{rl}]^{\mathrm{T}} \tag{4-73}$$

The matrix A is defined as:

$$A = \begin{bmatrix} A_{11} & A_{12} \\ A_{21} & A_{22} \end{bmatrix} \tag{4-74}$$

where A_{11}, A_{12}, A_{21}, and A_{22} are defined as Eqs. (4-32) to (4-35).

Also, the matrices B and C are defined as:

$$B = \begin{bmatrix} \dfrac{sin\delta}{mv_x R_{eff}} & \dfrac{sin\delta}{mv_x R_{eff}} & 0 & 0 \\ \dfrac{l_f sin\delta}{I_z R_{eff}} & \dfrac{l_f sin\delta}{I_z R_{eff}} & 0 & 0 \end{bmatrix} \tag{4-75}$$

$$C = \begin{bmatrix} 0 & 0 \\ 0 & 0 \end{bmatrix} \tag{4-76}$$

The matrix D is defined as:

$$D = \begin{bmatrix} \frac{S\delta}{mR_{eff}} + \frac{\bar{C}_{fr}C\delta}{m} & \frac{S\delta}{mR_{eff}} + \frac{\bar{C}_{fr}C\delta}{m} & \frac{\bar{C}_{rr}}{m} & \frac{\bar{C}_{rl}}{m} \\ l_f\left(\frac{S\delta}{R_{eff}} + \bar{C}_{fr}C\delta\right) & l_f\left(\frac{S\delta}{R_{eff}} + \bar{C}_{fl}C\delta\right) & -l_r\bar{C}_{rr} & -l_r\bar{C}_{rl} \end{bmatrix} \tag{4-77}$$

It should be noted that the state-space model is a linear parameter varying and the model parameters are being updated at each time step.

4.4.2. Actuation Dynamics

The time delay between the actuation torque command and the actual torque applied to the front axle is considered in this study as a first-order dynamic delay as follow:

$$T_{ij} = \frac{1}{1+\tau s} T_{ij,in} \tag{4-78}$$

where $T_{ij,in}$ is the actuator command to each electric motor, and τ is the electric motor's time delay. Eq. (4-78) can be rewritten in the following form as:

$$\begin{bmatrix} \dot{T}_{fr} \\ \dot{T}_{fl} \\ \dot{T}_{rr} \\ \dot{T}_{rl} \end{bmatrix} = \underbrace{\begin{bmatrix} -\frac{1}{\tau} & 0 & 0 & 0 \\ 0 & -\frac{1}{\tau} & 0 & 0 \\ 0 & 0 & -\frac{1}{\tau} & 0 \\ 0 & 0 & 0 & -\frac{1}{\tau} \end{bmatrix}}_{A_u} \begin{bmatrix} T_{fr} \\ T_{fl} \\ T_{rr} \\ T_{rl} \end{bmatrix} + \underbrace{\begin{bmatrix} \frac{1}{\tau} & 0 & 0 & 0 \\ 0 & \frac{1}{\tau} & 0 & 0 \\ 0 & 0 & \frac{1}{\tau} & 0 \\ 0 & 0 & 0 & \frac{1}{\tau} \end{bmatrix}}_{B_u} \begin{bmatrix} T_{fr,in} \\ T_{fl,in} \\ T_{rr,in} \\ T_{rl,in} \end{bmatrix} \tag{4-79}$$

By considering the actuator dynamic in the state space form of Eq. (4-79), one can reformulate the state-space system defined as Eqs. (4-69) and (4-70) into an augmented form of state-space model with six states of yaw rate, sideslip angle, and the four corner torques. Therefore, the augmented state-space model is defined as:

$$\dot{X} = \bar{A}X + \bar{B}U + \bar{d}_x \tag{4-80}$$

$$Y = \bar{C}X + \bar{d}_y \tag{4-81}$$

where

$$\bar{A} = \begin{bmatrix} A & B \\ 0_{4\times 2} & A_u \end{bmatrix} \tag{4-82}$$

$$\bar{B} = \begin{bmatrix} 0_{2\times 4} \\ B_u \end{bmatrix} \tag{4-83}$$

$$\bar{C} = [C \quad D] \tag{4-84}$$

$$\bar{d}_x = \begin{bmatrix} d_x \\ 0_{4\times 1} \end{bmatrix} \tag{4-85}$$

and

$$\bar{d}_y = d_y \tag{4-86}$$

The augmented state-space is presented as Eqs. (4-80) and (4-81) is in the continuous-time domain and must be discretized before any optimization progress. The step-invariant method is applied to discretize the continuous-time model. Assuming the discrete-time period $t_k \leq t < t_{k+1}$, with the sample time T_s, the discrete-time state-space model is defined as:

$$X_{k+1} = \bar{A}_d X_k + \bar{B}_d U_k + \bar{d}_{xd} \tag{4-87}$$

$$Y_k = \bar{C}_d X_k + \bar{d}_{yd} \tag{4-88}$$

where the augmented model matrices are $\bar{A}_d = e^{\bar{A}(t)T_s}$, $\bar{B}_d = \int_0^{T_s} e^{\bar{A}(t)\tau}\bar{B}(t)d\tau$, $\bar{d}_d = \int_0^{T_s} e^{\bar{A}(t)\tau}\bar{d}(t)d\tau$, $\bar{C}_d = \bar{C}$, and $\bar{d}_{yd} = \bar{d}_y$.

4.4.3. Performance Index

To find the optimal values of the system inputs, the following objective function is defined:

$$J = \|W_{2\times2}(Y - Y_{des})\|^2 + \|R_{4\times4}U\|^2 \tag{4-89}$$

where W is the outputs weight matrix and R is the input weight matrix.

4.4.4. Constraints

The solution to the optimization problem needs to be bounded by the total torque requested by the driver. Also, the torque command to both front and rear axles are assumed to be positive and no negative torque (breaking) is acceptable in this study. In addition to the driver torque command, the tire

capacities restrict the optimization problem. Therefore, the optimization must find the optimal corner torques values such that they satisfy the following constraints:

Input Equality constraint

$$T_{fr} + T_{fl} + T_{rr} + T_{rl} = T \tag{4-90}$$

Input Inequality constraints

$$0 \leq T_{fr} \leq \mu R_{eff} F_{zfr} \tag{4-91}$$

$$0 \leq T_{fl} \leq \mu R_{eff} F_{zfl} \tag{4-92}$$

$$0 \leq T_{rr} \leq \mu R_{eff} F_{zrr} \tag{4-93}$$

$$0 \leq T_{rl} \leq \mu R_{eff} F_{zrl} \tag{4-94}$$

4.4.5. Quadratic Programing Problem

In order to minimize the performance index introduced in Eq. (4-89), the optimal input values of the corner torques must be found by an optimization solver while satisfying all constraints defined in Eqs. (4-90) to (4-94). The performance index J and constrains are rewritten in form of a quadratic problem as follow:

$$\begin{aligned} &\min J = \frac{1}{2} U^T H U + f U \\ &subject\ to\ LB \leq U \leq UB \end{aligned} \tag{4-95}$$

where LB and UB abbreviate the constraints lower bound and upper bound, respectively. Also, matrices H and f are defined as:

$$H = 2((\bar{C}_d\bar{B}_d)^T W(\bar{C}_d\bar{B}_d) + R) \tag{4-96}$$

$$f = 2\left(X_k^T(\bar{C}_d\bar{A}_d)^T + (\bar{C}_d\bar{A}_d)^T\bar{d}_{xd}^T + \bar{d}_{dy}^T - Y_{des}\right)W\bar{C}_d\bar{B}_d \tag{4-97}$$

4.4.6. Feedforward Corner Torque Distribution Controller

In this section, a feedforward controller is designed based on the optimal corner torque distribution algorithm that receives the steering and torque commands from the driver and delivers the optimal torque commands to each electric motor. The general structure of the controller is shown in Figure **4-33**. The optimal corner torque distribution is experimentally evaluated on a Chevrolet Equinox for different driving scenarios. The results are presented and explained in the next section.

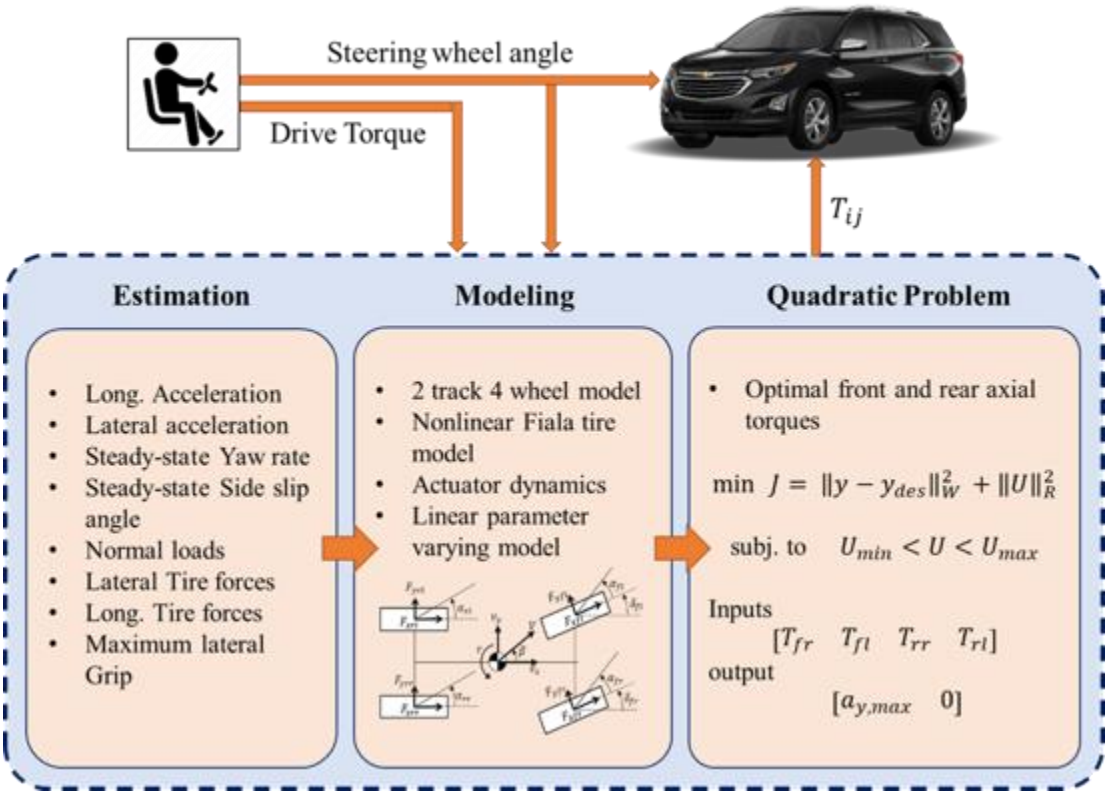

Figure 4-33. Feedforward optimal torque distributor architecture

4.4.7. Experimental Results

The corner base version of the feedforward controller is evaluated experimentally on an AWD GM Chevrolet Equinox with four independent electric motors in this section. The open-loop optimal torque distribution is implemented in MATLAB\Simulink environment and connected to the vehicle through a dSPACE MicroAutobox with a sampling time 5 ms. The dSPACE communicates with the GPS unit, the (IMU), and the electric motors through the CAN. The vehicle longitudinal and lateral velocities are measured with the GPS unit. The vehicle lateral acceleration is measured with the IMU sensor. The CAN bus delivers the requested torque command to the electric motors. Two driving scenarios are tested and results are presented in the next sections.

4.4.7.1. Acceleration in turn on dry road

To perform an acceleration in turn, the driver applied a constant steering wheel angle with the magnitude $\delta_{sw} = 7\ rad$, as shown in Figure 4-34. The vehicle started to accelerate from an initial speed $v_{x0} = 0$ with full throttle and reached the maximum total torque of $5000\ Nm$ in $t = 1s$. This driving scenario is repeated once with the feedforward controller being turned on and another with the feedforward controller is off. When the feedforward controller is off, the vehicle distributes the driver's requested torque equally between all four corners. As the lateral and longitudinal accelerations increased, the normal load transfers in the lateral and longitudinal directions would increase, too. Due to the lateral load transfer effect, the inner tires of the vehicle have a lower normal load. In addition, the longitudinal load transfer reduces the front tires normal loads. As a result, the front inner tire has the minimum normal load and the rear outer tire has the maximum normal load during the scenario. The feedforward controller estimates the normal loads of each tire and optimizes the corner torques such that each tire stays at its limits of force generation and produce maximum possible longitudinal and lateral forces. The optimal torque distribution on each corner are presented in Figure 4-35.

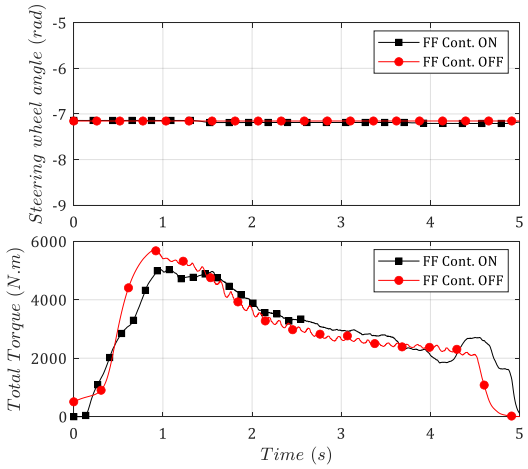

Figure 4-34. Driver Input for acceleration in turn on dry road: (a) steering wheel angle, (b) total torque

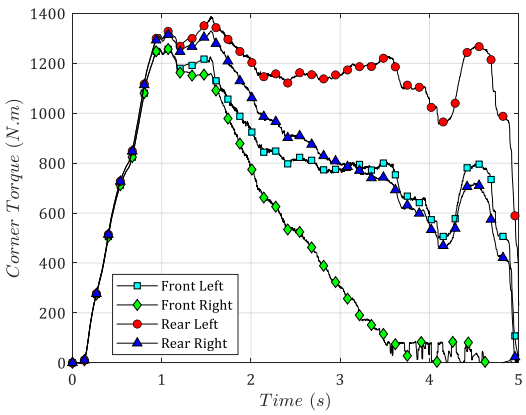

Figure 4-35. Optimal torque distribution to the front and rear axles for acceleration in turn on dry road

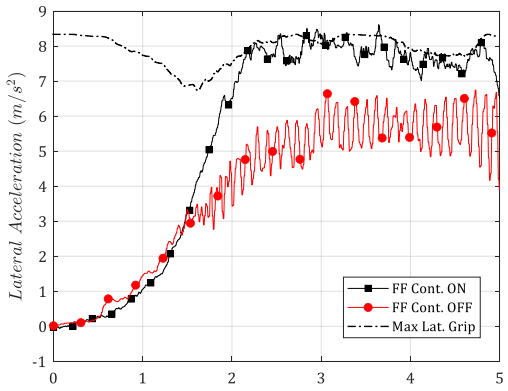

Figure 4-36. Effect of optimal torque distribution on lateral acceleration

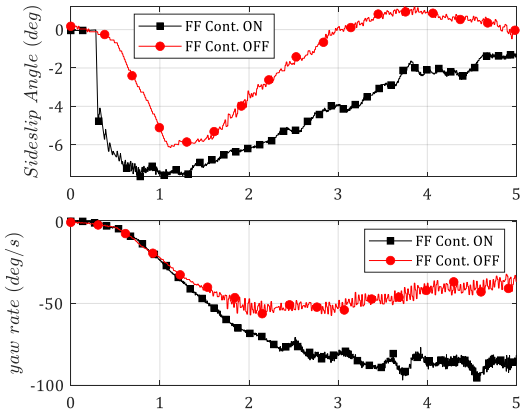

Figure 4-37. Torque distribution effect on sideslip angle, and yaw rate

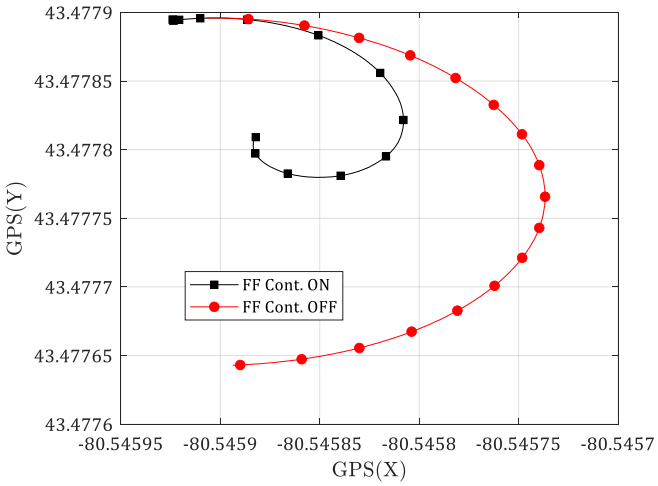

Figure 4-38. Vehicle trajectory

Optimizing the corner torque increases the vehicle's lateral grip, which allows the vehicle to reach higher lateral acceleration, see Figure 4-36. It can be seen in this figure that the lateral acceleration has reached its maximum possible value; maximum lateral acceleration is shown with the black dashed line in Figure 4-36. This is while when the optimal torque distribution is off, the lateral acceleration (red line with circle markers) is approximately 40% less than its maximum limit. Figure 4-36 also shows

huge fluctuations in the lateral acceleration data collected from the experiment with the feedforward controller being off. The high slip ratio at the front right tire contact patch causes fluctuations in the lateral acceleration and making the front axle shakes in high-speed values. The high slip ratio in the front tire, when the feedforward controller is off, has caused by sending 25% of the total torque to this tire while there is almost no normal load acting on this tire. The normal loads acting on each tire are shown for both experiments with the feedforward controller on and off in Figure 4-39 and Figure 4-40.

It can be seen in Figure 4-39 and Figure 4-40 that from $t = 3s$ to $t = 5s$ the estimated normal loads acting on the front right tire are negative. Since having a negative normal load is not possible in reality it means that the actual value of the normal load is either zero or the front tire is lifted from the ground. Therefore, sending 25% of the torque to this tire creates a high slip ratio, and drastically reduces the vehicle lateral grip. It can be seen in Figure 4-35 that during this time, the optimal torque sent to this tire is almost zero to keep the tire lateral grip at its maximum value. The wheel speed of tires during each test are presented in Figure 4-41 and Figure 4-42.

The result of maximizing the lateral grip with optimizing the corner torques can be seen in the vehicle trajectory shown in Figure 4-38. Comparing the vehicle trajectories in both tests, one can see the importance of having a maximum lateral grip during sharp cornering.

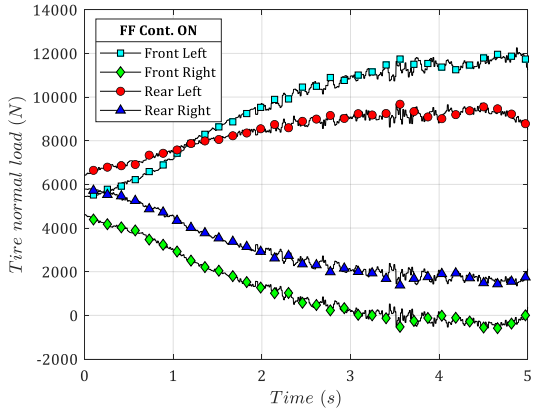

Figure 4-39. Tires normal load when feedforward is ON

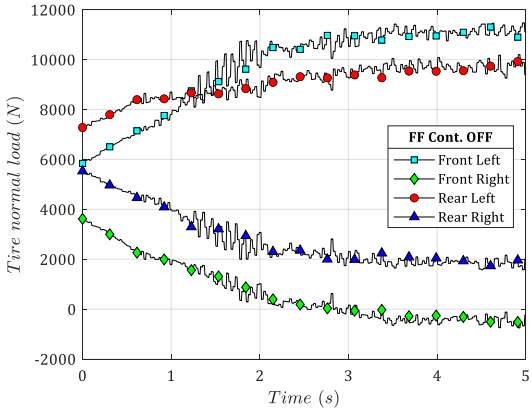

Figure 4-40. Tires normal load when feedforward is OFF

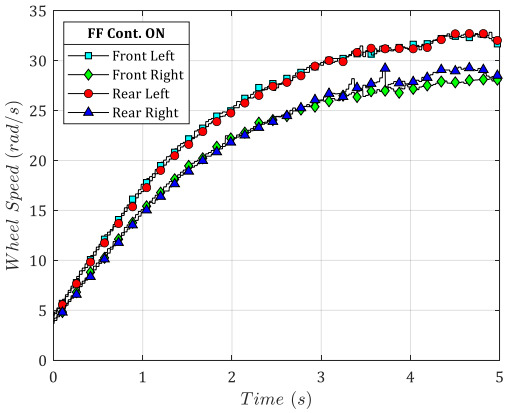

Figure 4-41. Wheel speeds when feedforward is ON

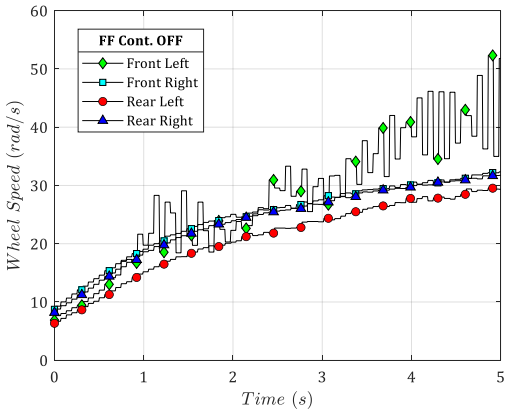

Figure 4-42. Wheel speeds when feedforward is OFF

4.4.7.2. Double Lane change on dry road

The second scenario performed on the Chevrolet Equinox was a double lane change on a dry road. The same scenario is repeated once with the feedforward controller on, and another with the feedforward controller off. The driver's inputs are shown in Figure 4-43. The optimized torques to the corners with the controller on are presented in Figure 4-44. The vehicle has been started from a speed of $v_{x0} = 20\ km/h$ and when the steering angle is applied, the normal load transfers are estimated and the torque corners being optimized with respect to the available tire capacities at each corner.

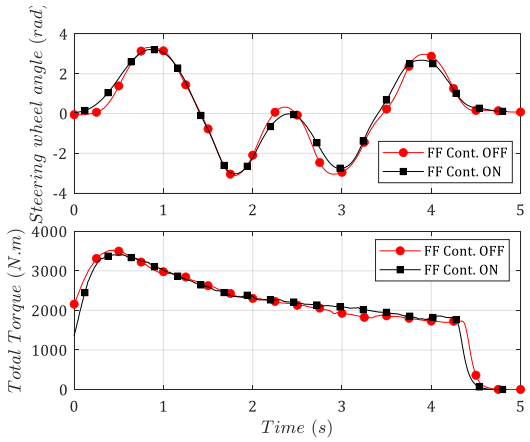

Figure 4-43. Driver Input for lane change on wet road: (a) steering wheel angle, (b) total torque

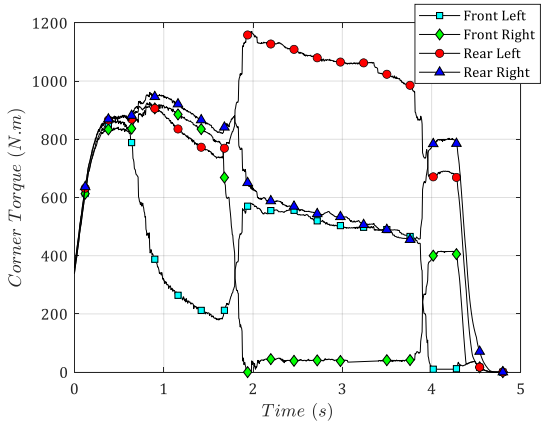

Figure 4-44. Optimal torque distribution to the front and rear axles for lane change scenario on wet road

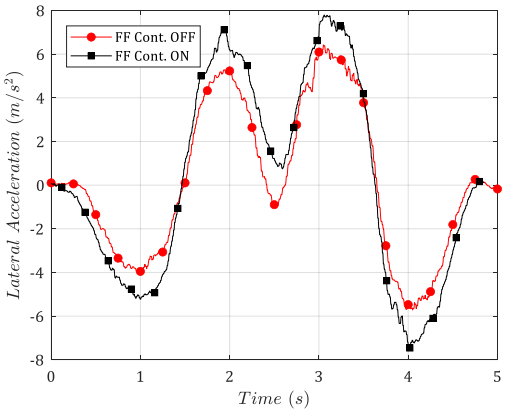

Figure 4-45. Effect of optimal torque distribution on lateral acceleration

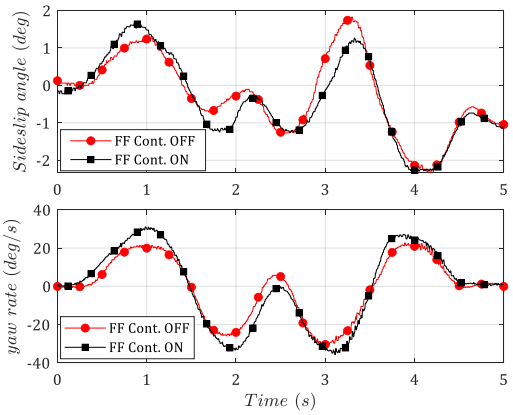

Figure 4-46. Torque distribution effect on sideslip angle, and yaw rate.

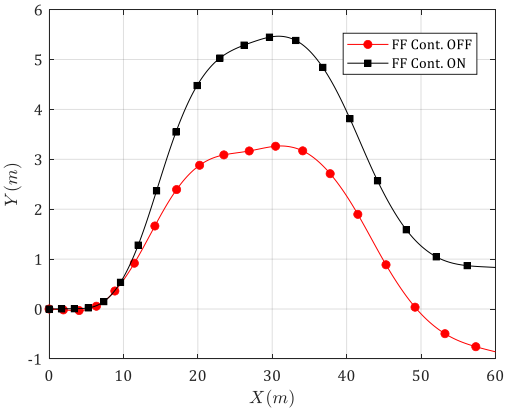

Figure 4-47. Vehicle trajectory

Comparing the vehicle trajectories at each test, it can be seen that feedforward torque control can perform a deeper double lane change. When the controller is off, the lateral displacement is 50% shorter than when the controller is on. This can be highly beneficial during an obstacle avoidance scenario.

4.5. Summary

One of the objectives of this chapter was to perform dynamic analysis of a vehicle driving under different axial torque distribution. The phase portrait of the two main vehicle states, namely, the sideslip angle, and yaw rate, presented the dynamic behavior of the vehicle with different torque distributions. According to the studies conducted in this chapter, the axle torque distribution can impact the vehicle stability, significantly. Depending on the desired trajectories for the vehicle sideslip angle and yaw rate, the optimal axial torque distribution could be used to obtain the best possible result. A parameter sensitivity analysis was performed on $(\beta - r)$ phase plane of the vehicle under various axial torque distribution. The effect of torque distribution on the equilibrium points, safe envelope, and trajectories of the phase plane was studied. It was concluded that when more torque is applied to the rear axle, the location of the saddle equilibria moves closer to the center of the phase plane, and the safe envelope shrinks. The dynamic analysis showed that there should be a torque distribution ratio, which could optimize the vehicle stability as well as steerability. Therefore, the axial-base and the corner-base

optimal torque distribution algorithms were developed to enhance vehicle performance at the limits of handling. The torque distribution algorithms aim to push the vehicle to its handling limits so that the vehicle could reach its maximum possible lateral acceleration. Two feedforward controllers were designed that based on the steering and torque commands from the driver, the torque was optimally distributed to the corners. The feedforward controllers were evaluated numerically as well as experimentally. It was shown that optimal torque distribution maximizes the lateral grip of the vehicle and enhances vehicle performance and maneuverability.

Chapter 5

Active Aerodynamic Control System

An active aerodynamic system consists of aerodynamic surfaces to control the air forces applied to the vehicle at high speeds. The two main force components created by aero surfaces are in longitudinal (drag) and normal (lift\downforce) directions. Designing the aero surfaces with appropriate shapes and angles result in creating mostly downforces. The extra downforce added through the aerodynamic surfaces increases the braking/traction capacity and enhances the handling and stability during maneuvers with high acceleration. In addition, adding active aerodynamic surfaces would balance the normal load distribution, which also leads to better traction or braking.

In an active aerodynamic system, the aero surfaces' angles are not constant. They are mechanically connected to a DC motor that changes the surfaces' angles within a limited range. In this dissertation, it is assumed that the vehicle is equipped with two active aero surfaces at the front and rear. The angles of the aero surfaces are controlled independently through a feedforward-feedback control system. The active aerodynamic control system consists of a feedforward controller and a feedback model predictive controller (MPC). The feedforward controller assigns appropriate angles to the front and rear aero surfaces based on the tire's grip and the driver's requested forces. Then the optimal angles found by the feedforward controller are fed to the vehicle and the feedback MPC. The designed MPC with the main objective of yaw rate and sideslip tracking adjust the aero surfaces' angles. The angle adjustment commands from MPC are combined with the feedforward commands and the final angles are applied to the vehicle. In the next section, the active aerodynamic system modeling, the feedforward control structure, and the MPC structure are explained in detail.

5.1. Active-Aerodynamic System Modeling

As mentioned before, in this section, the active aerodynamic model is explained. As shown in Figure 5-1, it is assumed that the vehicle is equipped with two aero surfaces one at the front of the vehicle and the other one at the rear.

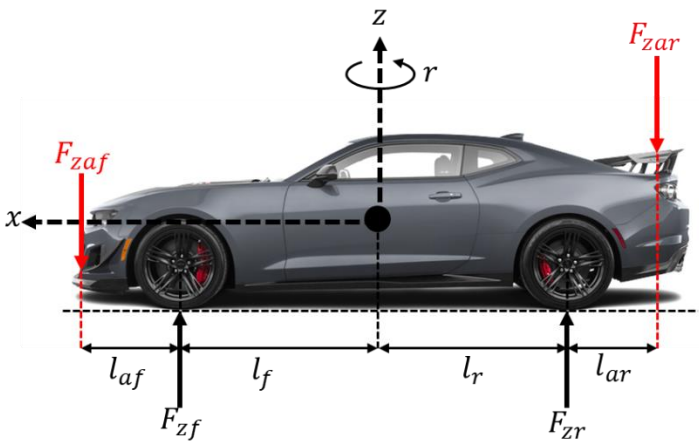

Figure 5-1. Schematic model of the vehicle with active aerodynamic wings at the front and rear of the vehicle

Since the vehicle is assumed to be at its limits of handling, the normal load transfer due to the longitudinal and lateral accelerations must be considered. Also, the effect of active aerodynamic loads is considered in the normal load estimations. The normal loads at each corner are defined as:

$$F_{z,fr}^{+AA} = \frac{1}{2l}\left(mgl_r + F_{zaf}\left(l_{af} + l\right) - F_{zar}l_{ar} - ma_x h\right) + \frac{ma_y h}{2d} \tag{5-1}$$

$$F_{z,fl}^{+AA} = \frac{1}{2l}\left(mgl_r + F_{zaf}\left(l_{af} + l\right) - F_{zar}l_{ar} - ma_x h\right) - \frac{ma_y h}{2d} \tag{5-2}$$

$$F_{z,rr}^{+AA} = \frac{1}{2l}\left(mgl_f - F_{zaf}l_{af} + F_{zar}(l_{ar} + l) + ma_x h\right) + \frac{ma_y h}{2d} \tag{5-3}$$

$$F_{z,rl}^{+AA} = \frac{1}{2l}\left(mgl_f - F_{zaf}l_{af} + F_{zar}(l_{ar} + l) + ma_x h\right) - \frac{ma_y h}{2d} \tag{5-4}$$

where F_{zai} is the normal load created from the active aerodynamic wings, and l_{ai} is the approximate point of application of the normal load of active aerodynamics as shown schematically in Figure 5-1.

As explained in section 3.1.1, the lateral forces are being modeled using the Fiala tire model. In this model, the normal load acting on the tire is one of the main parameters. Therefore, the normal load variations of the vehicle with aero surfaces must be fully addressed in the tire model and the control model. To understand the effect of the normal load in the tire model, the lateral tire force generated under various values of normal loads are plotted in Figure 5-2.

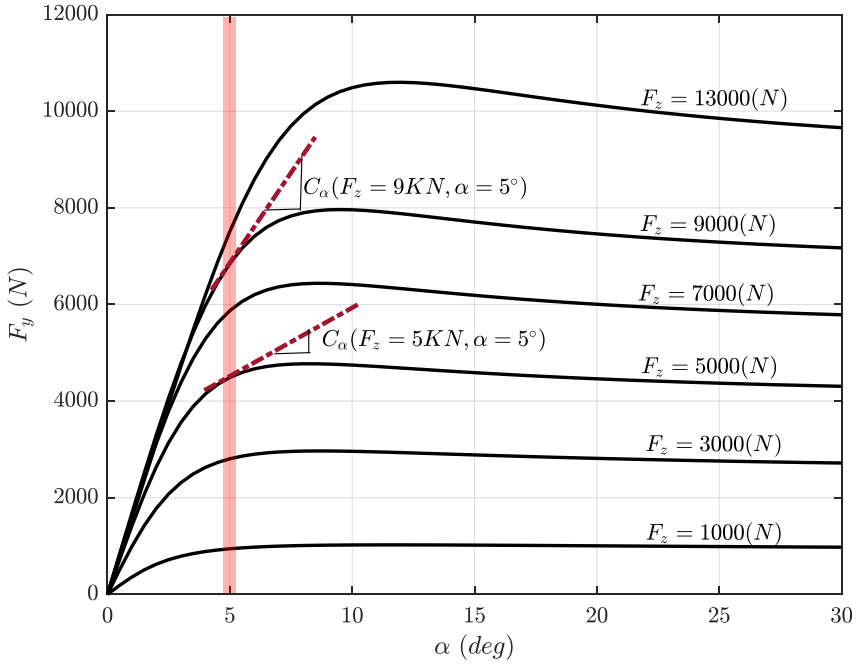

Figure 5-2. Tire lateral force under various normal loads

By defining the tire cornering stiffness C_α , as the derivative of the lateral force with respect to the tire sideslip angle, the effect of the normal load on the tire cornering stiffness can be studied. For instance, as shown in Figure 5-2, at the tire sideslip angle $\alpha = 5°$, the cornering stiffness C_α varies significantly with the variation of the normal load from $F_z = 5000\ N$ to $F_z = 9000\ N$. Therefore, when active aerodynamic wings are added to the system as actuators, the effect of normal load variations must be considered in the tire modeling. To include the active aerodynamic modeling in the system, the Fiala tire model introduced as Eq. (3-18) is rewritten as follow:

$$F_y = \begin{cases} -C_\alpha \tan\alpha + \dfrac{C_\alpha^2}{3\,\mu\,F_z^{+AA}} |\tan\alpha\,| \tan\alpha\ - \dfrac{C_\alpha^3}{27\,\mu^2\,(F_z^{+AA})^2} \tan^3\alpha & |\alpha\,| \le \alpha_{lim} \\ -\mu\,F_z^{+AA}\ sgn\ \alpha & |\alpha\,| > \alpha_{lim} \end{cases} \quad (5\text{-}5)$$

Another important parameter in the active aerodynamic modeling is the aerodynamic characteristics of the aero surface. In order to obtain the aerodynamic characteristics of the aero surfaces such as lift and drag coefficients, advanced aerodynamic analysis is required which is out of the scope of this research. Instead, the results of an investigation performed in [64] are used to identify aerodynamic characteristics of the are wings for this dissertation. The aerodynamic characteristics of the aero surfaces were obtained through experimentally testing the vehicle in a wind tunnel. Different tests were performed with various angles of attack from $-6°$ to $18°$ [64]. The results are presented in Table 5-1.

Table 5-1. *Aerodynamic characteristic of aero surface at different angles of attack* [64]

Angle of attack $\boldsymbol{\alpha_z\ (deg)}$	*Lift Coef.* $\boldsymbol{C_z}$	*Drag Coef.* $\boldsymbol{C_x}$
-6	*-0.142*	*0.0525*
-3	*0.087*	*0.0431*
0	*0.327*	*0.0432*
3	*0.573*	*0.0538*
6	*0.825*	*0.0720*
9	*1.015*	*0.0966*
12	*1.185*	*0.1342*
15	*1.275*	*0.1810*
18	*1.150*	*0.2520*

According to Table 5-1, the lift coefficient for the aero surfaces changes nonlinearly with respect to the aero surfaces' angles of attack. A curve fitting method is used to define the function of $C_z(\alpha_z)$.

By having the lift coefficient, the normal reaction forces from the wing surface are calculated as:

$$F_{zai} = \frac{1}{2}\rho A_i v_x^2 C_{zi}(\alpha_{zi}) \tag{5-6}$$

where ρ is the air density, and A_i is the frontal area of the wing surface.

5.2. Active-Aerodynamic control system

An active-aerodynamic control system is designed to find the optimal aero surfaces' angles of attack and stabilize the vehicle using the active aerodynamic system. The schematic model for the active aerodynamic control system is presented in Figure 5-3. The designed controller consists of two main parts, (a) feedforward controller and (b) feedback MPC. Each of these controllers is explained in detail in the following sections.

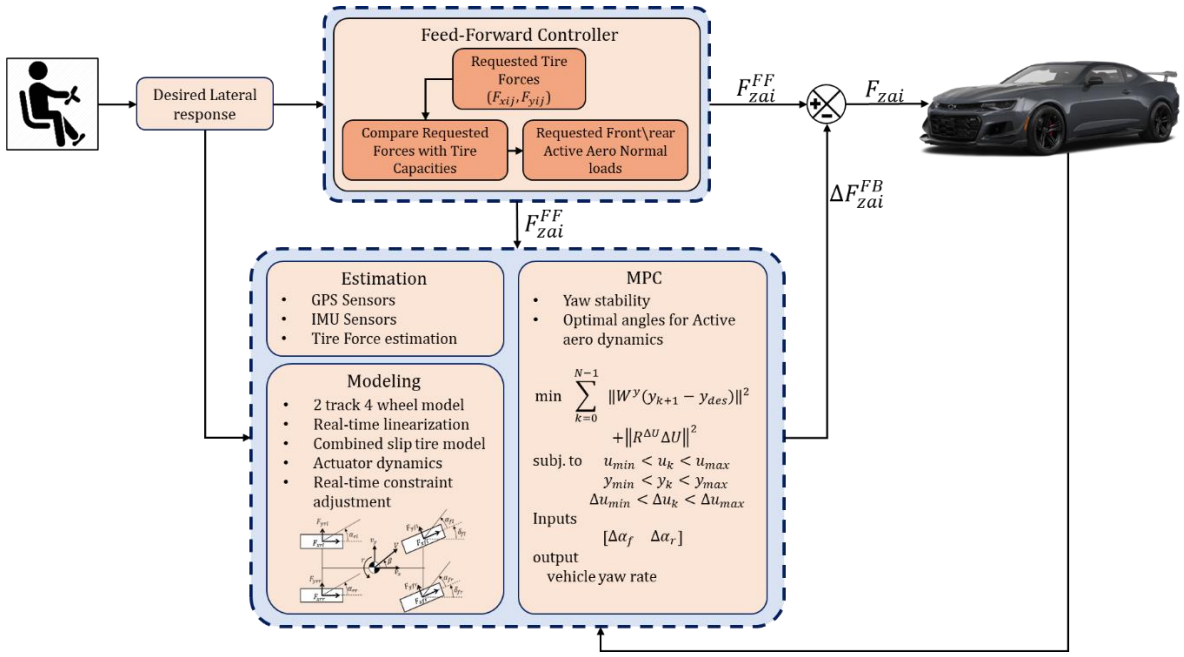

Figure 5-3. Schematic model of the feedforward-feedback MPC controller for active aerodynamic system

5.2.1. Feed-Forward Active Aerodynamic Control

A feed-forward controller is designed in this section to find the aero surfaces' angles of attack according to the available grips on each axle. The feedforward controller receives the driver's steering angle and torque input and the only actuators considered for this controller are the front and rear active aerodynamic wings. By neglecting the wheel dynamics, the requested longitudinal forces are defined as:

$$F_{xij}^{req} = \frac{T_{ij}}{R_{eff}} \tag{5-7}$$

where T_{ij} is brake/drive torque input on each wheel.

To estimate the lateral tire forces, steady-state yaw rate, and sideslip angle of the vehicle are defined as follow:

$$r_{ff} = sign(r_{ss}) \min(|r_{ss}|, |a_{y,max}|) \tag{5-8}$$

$$\beta_{ff} = sign(\beta_{ss}) \min(|\beta_{ss}|, |\beta_{max}|) \tag{5-9}$$

where

$$r_{ss} = \frac{v_x}{l + k_{us} v_x^2} \delta \tag{5-10}$$

and

$$\beta_{ss} = \frac{l_r - \frac{l_f m}{2 l C_{\alpha r}} v_x^2}{l + k_{us} v_x^2} \delta \tag{5-11}$$

where k_{us} is the understeer coefficient of the vehicle response. Also, β_{max} is based on the safe envelope theory defined as Eqs. (4-11) and (4-12). By including the tire grip being added to the vehicle by the active aerodynamic system, the maximum lateral acceleration $a_{y,max}$ is modified as:

$$a_{y,max} = \sqrt{\mu^2 \left(g + \frac{\sum F_{zai}^{max}}{m} \right)^2 - a_x^2} \tag{5-12}$$

where

$$F_{zai}^{max} = \frac{1}{2} \rho A_i v_x^2 C_{zi}(\alpha_{zi}^{max}) \tag{5-13}$$

To estimate normal loads acting on each wheel, lateral and longitudinal normal load transfers must be considered. To obtain the lateral acceleration required for calculation of lateral normal load transfer, a circular motion with a radius of $R = 1/\delta$ is assumed, and lateral acceleration is defined as follow:

$$a_y = \frac{v_x^2}{R} \tag{5-14}$$

Therefore, by having the requested longitudinal and lateral forces, the requested tire normal load can be found as:

$$F_{zij}^{req} = \frac{1}{\mu}\sqrt{\left(F_{xij}^{req}\right)^2 + \left(F_{yij}^{req}\right)^2} \tag{5-15}$$

The above F_{zij}^{req} would be the minimum required normal load on each tire for the vehicle to perform the driver's requested maneuver. If the requested normal load is less than the estimated one, then the active aerodynamic actuators must be activated to compensate for any lack of normal loads on tires. Since the aero surfaces are axial base, the tire with a maximum difference between its estimated normal load and requested one would be the priority for aero surface activation. Therefore, the required normal load from each aero surfaces is found as:

$$F_{zai}^{req} = \max(|\Delta F_{zii}|, |F_{zai}^{max}|) \tag{5-16}$$

where

$$\Delta F_{zij} = F_{zij}^{req} - F_{zij}^{est} \tag{5-17}$$

5.2.2. Feedback MPC Active Aerodynamic Control

The designed feedback MPC is explained in this section. The controller has the objective of tracking the desired yaw rate and sideslip angle with the only available actuators, front and rear active aerodynamic surfaces. The feedback controller receives the output of the feedforward controller F_{zai}^{req}

and apply angle adjustment to the aero surfaces to fulfill the objectives of yaw rate and sideslip angle tracking.

5.2.2.1. Prediction model

The double-track vehicle model is shown in Figure ***3-1*** is used as the prediction model. The vehicle equations of motion are defined as:

$$\dot{\beta} = \frac{1}{mv_x}\left(F_{yfr}cos\delta + F_{yfl}cos\delta + F_{yrr} + F_{yrl} + F_{xfr}sin\delta + F_{xfl}sin\delta\right) - r \tag{5-18}$$

$$\dot{r} = \frac{l_f}{I_z}\left(F_{yfr}cos\delta + F_{yfl}cos\delta + F_{xfr}sin\delta + F_{xfl}sin\delta\right) - \frac{l_r}{I_z}\left(F_{yrr} + F_{yrl}\right) - \frac{d}{2I_z}sin\delta\left(F_{yfr} - F_{rfl}\right) \tag{5-19}$$

The prediction states of the controller are the sideslip angle, and the yaw rate of the vehicle, i.e. $x = [\beta \quad r]^{\mathrm{T}}$. The inputs to the prediction model are the adjustment angle of attack for the front and rear aero surfaces:

$$u = [\Delta\alpha_{zf} \quad \Delta\alpha_{zr}]^T \tag{5-20}$$

The outputs of the feedback MPC are the vehicle yaw rate and the sideslip angle, i.e. $y = [\beta \quad r]^T$. The desired values for the vehicle yaw rate and the sideslip angle are defined as:

$$y_{des} = [\beta_{des} \quad r_{des}]^T \tag{5-21}$$

where

$$r_{des} = sign(r_{ss}) \min(|r_{ss}|, |a_{y,max}|) \tag{5-22}$$

$$\beta_{des} = sign(\beta_{ss}) \min(|\beta_{ss}|, |\beta_{max}|) \tag{5-23}$$

To derive the linear state-space model, the Eqs. (5-18) and (5-19) must be linearized at the operating points with respect to the tire sideslip angle and the angles of attack of the aero surfaces. The main nonlinear part in the Eqs. (5-18) and (5-19) are the lateral tire forces. Therefore, the nonlinear Fiala tire model must be linearized at the operating point as follow:

$$\begin{aligned} F_{y,ij} = F_{y,ij}(\bar{\alpha}_{ij}, \bar{\alpha}_{zi}) + (\alpha_{ij} - \bar{\alpha}_{ij}) \frac{\partial F_{y,ij}}{\partial \alpha_{ij}}\Bigg|_{\substack{\alpha_{ij}=\bar{\alpha}_{ij} \\ \alpha_{zf}=\bar{\alpha}_{zf} \\ \alpha_{zf}=\bar{\alpha}_{zf}}} + (\alpha_{zf} - \bar{\alpha}_{zf}) \frac{\partial F_{y,ij}}{\partial \alpha_{zf}}\Bigg|_{\substack{\alpha_{ij}=\bar{\alpha}_{ij} \\ \alpha_{zf}=\bar{\alpha}_{zf} \\ \alpha_{zf}=\bar{\alpha}_{zf}}} \\ + (\alpha_{zr} - \bar{\alpha}_{zr}) \frac{\partial F_{y,ij}}{\partial \alpha_{zr}}\Bigg|_{\substack{\alpha_{ij}=\bar{\alpha}_{ij} \\ \alpha_{zf}=\bar{\alpha}_{zf} \\ \alpha_{zf}=\bar{\alpha}_{zf}}} + \bar{F}_{y,ij} \end{aligned} \tag{5-24}$$

where $\bar{\alpha}_{ij}$ and $\bar{\alpha}_{zij}$ are the tire sideslip angle and aero surfaces' angles at the operating point. Defining the lateral force derivatives with respect to the tire sideslip angle and aero surfaces' angles as $\bar{C}_{aij}$ and $\bar{C}_{zij}$, the Eq. (5-24) can be rewritten as:

$$F_{y,ij} = \alpha_{ij}\bar{C}_{\alpha ij} + \alpha_{zf}\bar{C}_{zf,ij} + \alpha_{zr}\bar{C}_{zr,ij} + \bar{F}_{ij} \tag{5-25}$$

where $\bar{F}_{ij}$ includes all constant parts of the Eq. (5-24).

By substituting Eq. (5-24) into Eqs. (5-18) and (5-19), and performing mathematical simplification, the following state-space form is derived:

$$\dot{x} = Ax + Bu + d \tag{5-26}$$

$$y = Cx \tag{5-27}$$

The state matrix A is defined as:

$$A = \begin{bmatrix} A_{11} & A_{12} \\ A_{21} & A_{22} \end{bmatrix} \tag{5-28}$$

where A_{11}, A_{12}, A_{21}, and A_{22} are as follow:

$$A_{11} = \frac{cos\delta\left(\bar{C}_{\alpha fr} + \bar{C}_{\alpha fl}\right) + \bar{C}_{\alpha rr} + \bar{C}_{\alpha rl}}{mv_x} \tag{5-29}$$

$$A_{12} = \frac{l_f cos\delta\left(\bar{C}_{\alpha fr} + \bar{C}_{\alpha fl}\right) - l_r\left(\bar{C}_{\alpha fr} + \bar{C}_{\alpha fl}\right)}{mv_x^2} - 1 \tag{5-30}$$

$$A_{21} = \frac{l_f cos\delta\left(\bar{C}_{\alpha fr} + \bar{C}_{\alpha fl}\right) - l_r\left(\bar{C}_{\alpha fr} + \bar{C}_{\alpha fl}\right) + \frac{d}{2} sin\delta\left(\bar{C}_{\alpha fl} - \bar{C}_{\alpha fr}\right)}{I_z} \tag{5-31}$$

$$A_{22} = \frac{l_f^2 cos\delta\left(\bar{C}_{\alpha fr} + \bar{C}_{\alpha fl}\right) + l_r^2\left(\bar{C}_{\alpha fr} + \bar{C}_{\alpha fl}\right) + \frac{d}{2} l_f sin\delta\left(\bar{C}_{\alpha fl} - \bar{C}_{\alpha fr}\right)}{I_z v_x} \tag{5-32}$$

The input matrix B is defined as:

$$B = \begin{bmatrix} B_{11} & B_{12} \\ B_{21} & B_{22} \end{bmatrix} \tag{5-33}$$

$$B_{11} = \frac{cos\delta\left(\bar{C}_{zf,fr} + \bar{C}_{zf,fl}\right) + \bar{C}_{zf,rr} + \bar{C}_{zf,rl}}{mv_x} \tag{5-34}$$

$$B_{12} = \frac{cos\delta\left(\bar{C}_{zr,fr} + \bar{C}_{zr,fl}\right) + \bar{C}_{zr,rr} + \bar{C}_{zr,rl}}{mv_x} \tag{5-35}$$

$$B_{21} = \frac{l_f cos\delta\left(\bar{C}_{zf,fr} + \bar{C}_{zf,fl}\right) - l_r\left(\bar{C}_{zf,rr} + \bar{C}_{zf,rl}\right) + \frac{d}{2} sin\delta\left(\bar{C}_{zf,fl} - \bar{C}_{zf,fr}\right)}{I_z} \tag{5-36}$$

$$B_{22} = \frac{l_f cos\delta\left(\bar{C}_{zr,fr} + \bar{C}_{zr,fl}\right) - l_r\left(\bar{C}_{zr,rr} + \bar{C}_{zr,rl}\right) + \frac{d}{2} sin\delta\left(\bar{C}_{zr,fl} - \bar{C}_{zr,fr}\right)}{I_z} \tag{5-37}$$

5.2.2.2. Actuation Dynamics

In order to consider the time delays of the actuators, as an alternative of using a common method of delay handling with adding a first-order delay block to the control system [99], the dynamics of the actuator are included in the prediction model. The angle of attack for each aero surface is defined by a linear movement converted from the rotational movement of a DC motor. Considering the resistances in the electrical system and inertia of the mechanical system and linkages of the active aerodynamic wings, there would be a time delay from the actuator command to the DC motors and then to the angles of aero surfaces and down forces applied to the vehicle. To model the time delay of the active aerodynamic surfaces, a second-order time delay is assumed as:

$$\dot{\Delta\alpha_{zi}} = -\frac{1}{\tau_z}\Delta\alpha_{zi} + \frac{1}{\tau_z}\Delta\alpha_{zi,in} \tag{5-38}$$

The dynamic equation of actuator delay can be written in the state-space form as:

$$\begin{bmatrix}\dot{\Delta\alpha_{zf}}\\ \dot{\Delta\alpha_{zr}}\end{bmatrix} = \begin{bmatrix}-\frac{1}{\tau_z} & 0\\ 0 & -\frac{1}{\tau_z}\end{bmatrix}\begin{bmatrix}\Delta\alpha_{zf}\\ \Delta\alpha_{zr}\end{bmatrix} + \begin{bmatrix}\frac{1}{\tau_z} & 0\\ 0 & \frac{1}{\tau_z}\end{bmatrix}\begin{bmatrix}\Delta\alpha_{zf,in}\\ \Delta\alpha_{zr,in}\end{bmatrix} \tag{5-39}$$

The above state-space model is rewritten as:

$$\dot{x}_u = A_u x_u + B_u u_{in} \tag{5-40}$$

In order to fully integrate the actuator dynamics in the control system and prediction model, the state-space model of the control system is augmented with Eq. (5-25) as follow:

$$\begin{bmatrix}\dot{x}\\ \dot{x}_u\end{bmatrix} = \begin{bmatrix}A & B\\ 0_{2\times2} & A_u\end{bmatrix}\begin{bmatrix}x\\ x_u\end{bmatrix} + \begin{bmatrix}0_{2\times2}\\ B_u\end{bmatrix}u_{in} + \begin{bmatrix}d\\ 0_{2\times1}\end{bmatrix}$$

$$Y = \begin{bmatrix}C & 0_{2\times2}\end{bmatrix}\begin{bmatrix}x\\ x_u\end{bmatrix} \tag{5-41}$$

The Augmented model defined as Eq. (5-41) can be rewritten as:

$$\dot{X} = \bar{A}X + \bar{B}u_{in} + \bar{d} \tag{5-42}$$

$$Y = \bar{C}X \tag{5-43}$$

The step-invariant method is applied to discretize the continuous-time prediction model. Assuming the discrete-time period $t_k \leq t < t_{k+1}$, with the sample time T_s, the discrete-time prediction model is defined as:

$$X_{k+1} = \bar{A}_d X_k + \bar{B}_d u_{in,k} + \bar{d}_d$$
$$Y_k = \bar{C}_d X_k \tag{5-44}$$

where the augmented model matrices are $\bar{A}_d = e^{\bar{A}(t)T_s}$, $\bar{B}_d = \int_0^{T_s} e^{\bar{A}(t)\tau}\bar{B}(t)d\tau$, $\bar{d}_d = \int_0^{T_s} e^{\bar{A}(t)\tau}\bar{d}(t)d\tau$ and $\bar{C}_d = \bar{C}$.

5.2.2.3. Performance index

The objective of the designed feedback MPC is to track the desired yaw rate and sideslip angle. The desired yaw rate and sideslip angle are defined based on the steady-state responses explained in section 5.2.1. The performance index to optimize the input values for the states to follow the desired values is defined as follow:

$$J = \frac{1}{2}\sum_{k=1}^{N_p}\left(\|(Y_k - Y_{des})\|_W^2 + \left\|u_{in,k}\right\|_R^2\right) \tag{5-45}$$

where N_p is the number of prediction horizon, Y_k is the outputs of the system, and Y_{des} is the desired values for the system output. The notation $\|(Y_k - Y_{des})\|_W^2$ is the short version of $(Y_k - Y_{des})^T W (Y_k - Y_{des})$ where W is the positive semi-definite output weight matrix. The term $\left\|u_{in,k}\right\|_R^2$ in the objective function minimizes the control effort and R is the positive definite input weight matrix.

5.2.2.4. Constraints

The main constraints considered in the design of the feedback MPC is the input variable constraints. The constraints are defined based on the angles of the surface wings. They are defined as the upper bound and lower bounds of the control inputs as follow:

$$u_{in}^{min} \leq u_{in} \leq u_{in}^{max} \tag{5-46}$$

Since the feedback controller adjust the output of the feedforward controller, the values of α_{zi}^{ff} must be considered in the constraints of the feedback controller:

$$\alpha_{zi}^{min} - \alpha_{zi}^{ff} \leq \Delta\alpha_{zi} \leq \alpha_{zi}^{max} - \alpha_{zi}^{ff} \tag{5-47}$$

5.3. Simulation Results

The performance of the designed feedforward-feedback controller for the active aerodynamic system is evaluated in the CarSim simulation environment. The control system is codded in Simulink software, and integrated with a high fidelity CarSim model. The controller is evaluated during straight driving and braking, as well as during lane changes at the limits of handling. The simulation results are presented in the following sections.

5.3.1. Straight Accelerating

In this section, the feedforward control performance is evaluated during straight driving and braking. When a vehicle is moving straight, there is no error in yaw rate and sideslip angle. Therefore, the feedback MPC does not have contribution while driving straight. On the other hand, the torque requested by the driver might be more than tire capacities and an active aero system need to be activated. Since the feedforward controller works based on the tire capacities, as soon as the tires are near saturation, it activates the aerodynamic system and increases tire capacities as needed. A driving scenario where the driver requests a high amount of drive torque while driving straight is simulated in

this section. In this driving scenario, when the vehicle is moving in a straight line with the longitudinal speed $v_{x0} = 100\ km/h$, the driver requests a driving torque with the magnitude $T = 3600\ N.m$ as shown in Figure 5-4.

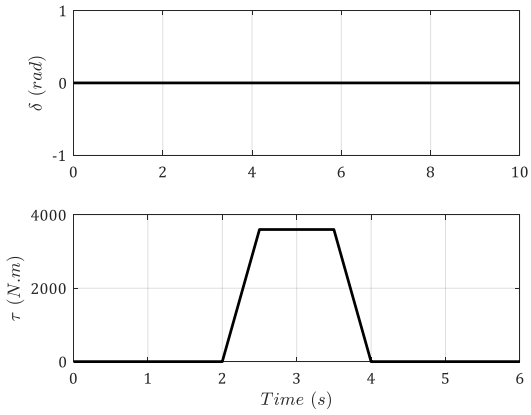

Figure 5-4. Driver's steering and torque inputs

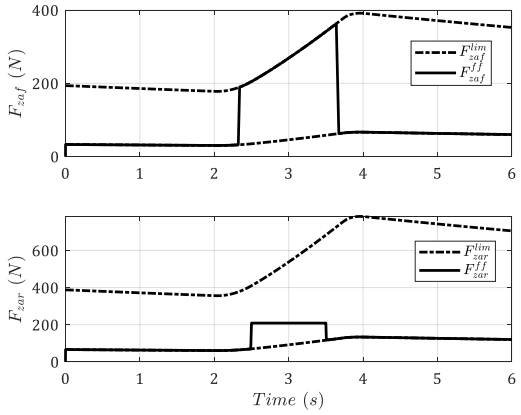

Figure 5-5. Front and rear normal loads created by the feedforward active aero controller

As shown in Figure 5-5, the feedforward controller has activated the front aero surface with maximum capacity and the rear aero surface is creating a 200 Nm normal load. The dashed lines in Figure 5-5 show the maximum and minimum amount of normal forces each aero surfaces can create. The tire capacities in force generation are shown in Figure 5-6 to Figure 5-8. The black solid lines show the total tire forces in longitudinal and lateral directions calculated based on the circle tire model $\left(F_x^2 + F_y^2\right)^{1/2}$. The solid lines with square marker show the maximum tire capacity in force generation when the active aerodynamic system is on and normal load shown in Figure 5-5 are applied to the system. The red dashed lines with circle marker show the tire force capacity when the active aerodynamic system is off. Due to the normal load transfer during accelerating, the front tires have a low capacity in force generation compared to the requested normal forces, red dashed lines with circle marker. Therefore, the feedforward controller activates the front aero surface to compensate for the shortage of tire force capacity in front tires. The rear active aero also activated and created 200 N normal force. It can be seen in Figure 5-8 and Figure 5-9 the rear tire capacities without active aerodynamics being on are more than the requested longitudinal forces. Activating the rear air wing can also affect

the front tires with the coupled effect of the front and rear active aerodynamic system. Therefore, the rear active air wing not only compensates for the rear tire capacities but also helps the front tires to have more capacity in force generation. Therefore, the rear aero surface has been activated more than required tire forces in the rear axle.

The effect of having normal loads increased by the active aerodynamic system can be seen on the tires' slip ratio. The low tire capacity makes the tires' slip ratio increase and tire force capacities decrease even more. The effect of increasing normal loads on the slip ratio of the front and rear tires are shown in Figure 5-10. It can be seen that when the active aerodynamics is on, the slip ratios on both axles are reduced by approximately 50%.

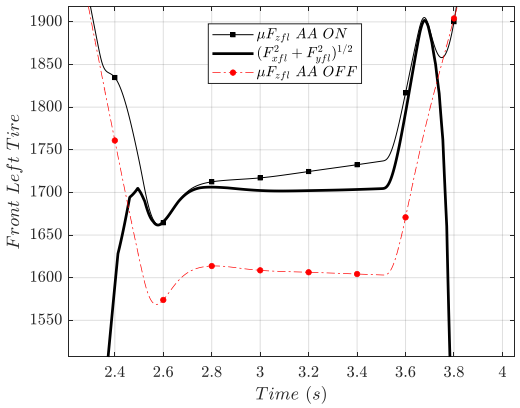

Figure 5-6. Front-left tire capacity in force generation

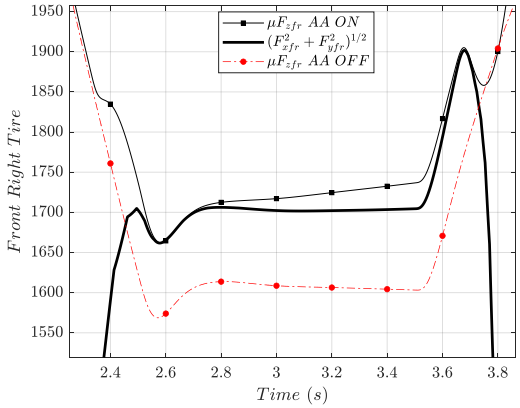

Figure 5-7. Front-right tire capacity in force generation

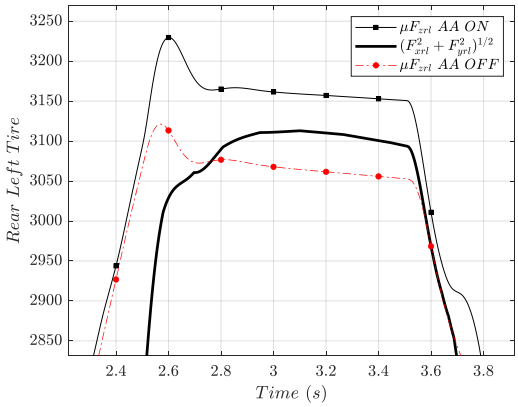

Figure 5-8. Rear-left tire capacity in force generation

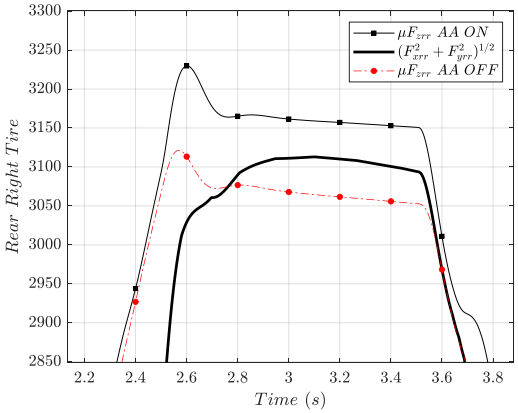

Figure 5-9. Rear-right tire capacity in force generation

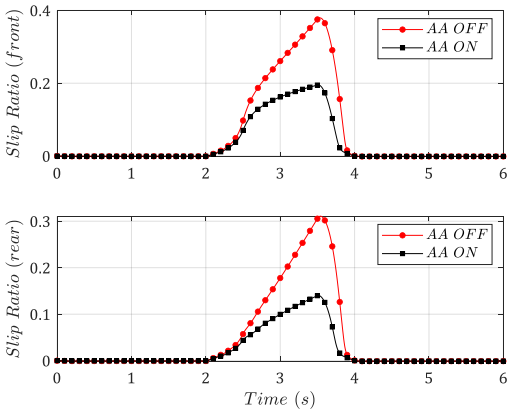

Figure 5-10. Front and rear tires' slip ratio

5.3.2. Double Lane Change

In this driving scenario, a sinusoidal steering input with the amplitude of 0.5 rad is applied to the vehicle. The requested drive torque with the maximum amount of $T = 1500\ N.m$ is shown in Figure 5-11. In this case, it is assumed that the vehicle has a RWD powertrain system with an open differential in the rear axle. Both feedforward and feedback controllers are contributing to keep the vehicle stable and track the desired yaw rate and sideslip angle. The feedforward controller has activated the rear air

wing as shown in Figure 5-12. Due to the RWD drivetrain system, there is no requested force on the front axle. On the other hand, as the steering magnitude increases, the lateral force requested by the driver increase. Therefore, the magnitude of the total forces estimated by the feedforward controller goes above the rear tires' capacities. Therefore, when the steering angle is applied, the feedforward controller activates the rear air wing and keeps the front air wing off.

Figure 5-13 shows the feedforward-feedback controller performance in tracking the desired yaw rate and sideslip angle. The air wing angles calculated by the feedforward controller are sent to the feedback MPC as initial angles for each air wing. Then the feedforward angles are being adjusted according to the feedback MPC objectives of tracking the desired yaw rate and sideslip angle.

Figure 5-14 shows the angles of the front and rear active aerodynamic surfaces during the simulation. It can be seen that the feedback MPC activates the front air when the vehicle is understeer. An example of the vehicle being understeer is from $t = 2.2\ s$ to $t = 3.8\ s$ when the vehicle yaw rate (black solid line) has not reached the desired yaw rate (blue solid line). When the front active aerodynamic is activated, normal loads acting on the front tires increases, and front tires can generate higher values of lateral forces. Creating more lateral forces will increase the oversteering yaw moment acting on the vehicle and helps the vehicle to reach higher yaw rates. At the same time, the feedback MPC decreases the angle of the rear active aerodynamic surface. Decreasing the normal loads acting on the rear tires can decrease the understeering yaw moment to let the vehicle to reach the desired yaw rate. Even though reducing the rear wing angle can help the vehicle reach the reach higher values of yaw rate, but it cannot be reduced to zero. This would affect both rear tire capacities and the stability of the vehicle. Therefore, the feedback MPC optimizes the rear wing angle to keep the vehicle stable, follow the desired yaw rate with minimum error, and keep the tire at its handling limits to create maximum possible lateral and longitudinal forces.

In Figure 5-13, the result of the system equipped with the feedforward-feedback controller is compared with a case that the active aerodynamic system is off (solid red line). It can be seen when the active aerodynamic system is turned off the vehicle gets oversteer and unstable. Since the vehicle is RWD, applying the steering angle creates a huge amount of lateral forces on the front tires and make the vehicle highly oversteer. Therefore, when the active aerodynamic increases the rear normal loads on the rear tires, it can balance the yaw moment of the vehicle with creating an understeer yaw moment.

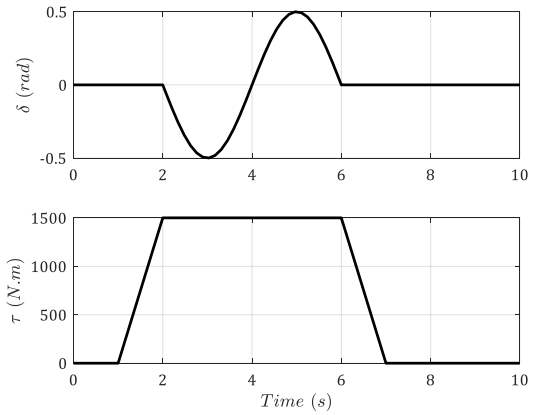

Figure 5-11. Driver's steering and torque inputs

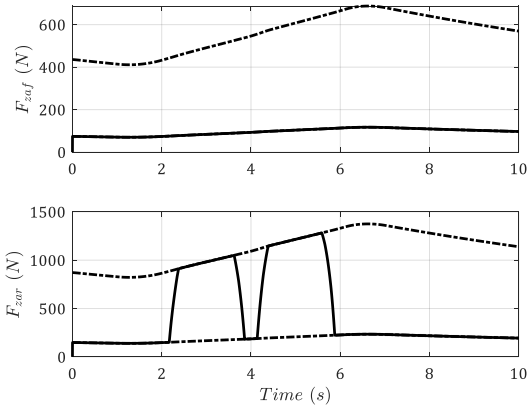

Figure 5-12. Front and rear normal loads created by the feedforward active aero controller

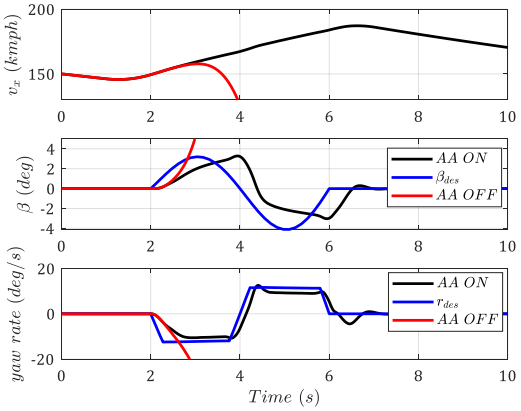

Figure 5-13. Vehicle response with and without Active Aero system: (a) longitudinal speed, (b) side slip angle, (c) yaw rate

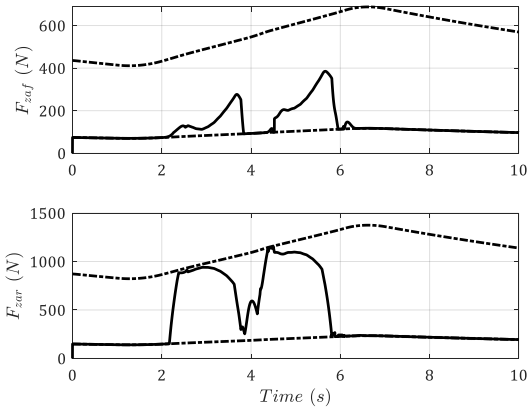

Figure 5-14. Front and rear normal loads created by the feedforward-feedback active aero controller

It should be noted that creating an understeering yaw moment can be effective only if it happens before the vehicle gets oversteer. When the vehicle is oversteer, the understeering yaw moment created by the rear aero surface cannot bring the vehicle back to the stable zone and the vehicle gets unstable. This is why having a feedforward controller is very important. The feedforward controller does not wait for the yaw error to get big enough to contribute. It activated the rear aero surface as soon as it

sees the vehicle requires a higher value of lateral forces to reach the desired yaw rate and increases the tire capacity by activating the rear wing. The effect of having a feedforward controller is shown in the next figures. In the same driving scenario, as explained before, the vehicle is simulated when the feedforward controller is off. Figure 5-15 shows the vehicle states and red lines belong to the scenario with the feedforward controller off. It can be seen that turning off the feedforward vehicle makes the vehicle unstable. The blue line is the results from the previous simulation with active aerodynamic angles, shown in Figure 5-14, and the air wing angles calculated by the feedback MPC are shown in Figure 5-16. It can be seen that the feedback MPC is doing its job as perfectly as it should. It has activated the front aero surface during the time vehicle is understeer ($t = 2s$ to $t = 2.6$), and as soon as the vehicle gets oversteer at $t = 2.6$, it stops the front aero surface and activates the rear aero surface to create understeer yaw moment. But at this time, the rear active aerodynamic actuator is not strong enough to create a sufficient amount of understeer yaw moment and cannot stabilize the vehicle.

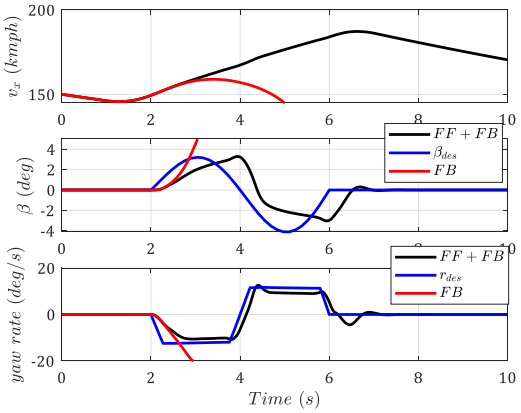

Figure 5-15. Vehicle response with and without feedforward controller: (a) longitudinal speed, (b) side slip angle, (c) yaw rate

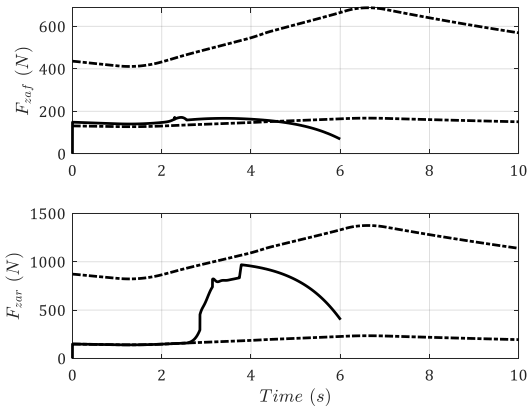

Figure 5-16. Front and rear normal loads created by the feedback active aero controller

5.4. Summary

In this chapter, active aerodynamic surfaces with the ability to changing their angles of attack in real-time were added as the vehicle actuation system. A control structure consists of a feedforward controller and a feedback MPC with the objective of yaw tracking was developed. The tire

nonlinearities and actuator dynamics were included in the prediction model. In order to increase the accuracy of the prediction model, a parameter varying prediction model was used instead of traditional linear time-invariant prediction models. The feedforward controller's main contribution was activating aerodynamic surfaces while the vehicle was moving straight and the yaw rate error was zero. The feedforward controller activated the front/rear aerodynamic surface whenever the wheel was approaching the saturation or the brake/drive torque sent to the wheels was more than their handling capacity. The feedforward controller was also highly essential during harsh maneuvers where the feedback MPC could not stabilize the vehicle. The feedforward controller could start the aerodynamic surface activation as soon as it estimated any lack of normal load, while the MPC had to wait for the yaw error to activate aerodynamic surfaces. Adding the feedforward controller improved the performance and stabilized the vehicle in harsh driving scenarios.

Chapter 6
Optimal Torque Distribution and Active Aerodynamics Control Integration

Although optimal torque distribution strategy has been very effective in improving the stability of the vehicle, there are situations that the requested torque is more than tire force capacities. In such conditions, the torque distribution strategy is not enough, and either the driver must reduce the total torque request or the controller should be smart enough to cut the extra torque commanded by the driver. In a performance car in which high-speed maneuvers are expected, cutting the torque requested by the driver may not be acceptable. In these cases, active aerodynamic surfaces can increase the normal load acting on the wheels to increase tire force capacities. Considering such situations, integrating the optimal torque distribution strategy with active aerodynamic control in the form of a multi-actuation control system becomes vital. In the present study, a multi-actuation Model Predictive Controller (MPC) is designed with the objectives of yaw tracking and stabilizing the vehicle lateral dynamics. Active aerodynamic surfaces in the front and rear of the vehicle and electric motors at the corners are the actuators of the designed MPC. In addition, a high-level constraint adjustment module is developed to observe the constraints of the MPC and prevent any unnecessary activation of the active aerodynamic surfaces. The high-level constraint adjustment module not only optimizes the actuation cost but also improves the MPC performance in stabilizing the system.

6.1. Control System Design

A model predictive controller is designed and explained in this section. The controller includes six actuators as four electric motors at each corner and two active aero surfaces at the front and rear of the vehicle. The main objective of the controller is tracking the desired yaw rate and optimizing the torque corners and angle of attack of each aero surfaces. A constraint adjustment model that observes tire

nonlinearities and constraints is designed and added to the control structure. The details of the control structure proposed in this chapter are explained in the following sections.

6.1.1. Prediction Model

A double-track vehicle model shown in **Figure 3-3** is used as the prediction model. The prediction states of the controller are the sideslip angle, and yaw rate of the vehicle $x = [\beta \quad r]^{\mathrm{T}}$. The inputs to the prediction model are corner torques and front\rear aero surfaces' angles of attack:

$$u = [T_{fr} \quad T_{fl} \quad T_{rr} \quad T_{rl} \quad \alpha_{zf} \quad \alpha_{zr}] \tag{6-1}$$

The output of the control system is the vehicle yaw rate, $y = [r]$. The desired value for the vehicle yaw rate is defined as $y_{des} = r_{des}$ and calculated based on the steady-state yaw response:

$$r_{des} = sign(r_s)\min(|r_s|, |a_{y,max}/v_x|) \tag{6-2}$$

where $a_{y,max}$ is the maximum lateral acceleration achievable and is estimated as:

$$a_{y.max} = ((\mu g)^2 - a_x^2)^{1/2} \tag{6-3}$$

Also r_{ss} is defined as:

$$r_{ss} = \frac{\delta_f v_x}{l + k_{us} v_x^2} \tag{6-4}$$

where k_{us} is the understeer coefficient of the vehicle response.

To derive the linear state-space form of the prediction model, the nonlinear tire model is linearized with respect to the tire sideslip angle and aero surfaces' angles of attack. It is assumed that the steering

angle and longitudinal speed is constant during the prediction horizon. Therefore, the lateral tire forces are expanded as:

$$F_{y,ij} = \left(\alpha_{ij} - \bar{\alpha}_{ij}\right)\frac{\partial F_{y,ij}}{\partial \alpha_{ij}}\bigg|_{\bar{\alpha}_{ij}} + \left(\alpha_{zi} - \bar{\alpha}_{zi}\right)\frac{\partial F_{y,ij}}{\partial \alpha_{zi}}\bigg|_{\bar{\alpha}_{zi}} + F_{y,ij}(\bar{\alpha}_{ij}, \bar{\alpha}_{zi}) \tag{6-5}$$

where $\bar{\alpha}_{ij}$ and $\bar{\alpha}_{zij}$ are the tire sideslip angle and aero surfaces' angles at the operating point. Defining the lateral force derivatives with respect to the tire sideslip angle and aero surfaces' angles as $\bar{C}_{aij}$ and $\bar{C}_{zij}$, the Eq. (6-5) can be rewritten as:

$$F_{y,ij} = \alpha_{ij}\bar{C}_{\alpha ij} + \alpha_{zi}\bar{C}_{zij} + \bar{F}_{ij} \tag{6-6}$$

where $\bar{F}_{ij}$ includes all the constant parts of Eq. (6-5). Substituting Eq. (6-6) into Eqs. (5-18) and (5-19), the prediction model can be written as $\dot{x} = Ax + Bu + d$ and $y = Cx$, where matrices A, B, and C are presented as:

$$A = \begin{bmatrix} a_{11} & a_{12} \\ a_{21} & a_{22} \end{bmatrix} \tag{6-7}$$

$$a_{11} = \frac{\bar{C}_{\alpha rl} + \bar{C}_{\alpha rl} + C\delta\left(\bar{C}_{\alpha fl} + \bar{C}_{\alpha fr}\right)}{mv_x} \tag{6-8}$$

$$a_{12} = \frac{C\delta\left(\bar{C}_{\alpha fr} + \bar{C}_{\alpha fl}\right)l_f - (\bar{C}_{\alpha rr} + \bar{C}_{\alpha rl})l_r}{mv_x^2} - 1 \tag{6-9}$$

$$a_{21} = \frac{1}{I_z}\left(C\delta\left(\bar{C}_{\alpha fr} + \bar{C}_{\alpha fl}\right)l_f - (\bar{C}_{\alpha rr} + \bar{C}_{\alpha rl})l_r - \frac{d}{2}S\delta\left(\bar{C}_{\alpha fr} - \bar{C}_{\alpha fl}\right)\right) \tag{6-10}$$

$$a_{22} = \frac{1}{I_z v_x}\left(C\delta\left(\bar{C}_{\alpha fr} + \bar{C}_{\alpha fl}\right)l_f^2 + (\bar{C}_{\alpha rl} + \bar{C}_{\alpha rr})l_r^2 - \frac{d}{2}S\delta\left(\bar{C}_{\alpha fr} - \bar{C}_{\alpha fl}\right)l_f\right) \tag{6-11}$$

$$a_{22} = \frac{1}{I_z v_x}\left(C\delta\left(\bar{C}_{\alpha fr} + \bar{C}_{\alpha fl}\right)l_f^2 + (\bar{C}_{\alpha rl} + \bar{C}_{\alpha rr})l_r^2 - \frac{d}{2}S\delta\left(\bar{C}_{\alpha fr} - \bar{C}_{\alpha fl}\right)l_f\right) \tag{6-12}$$

$$B = \begin{bmatrix} b_{11} & b_{12} & b_{13} & b_{14} & b_{15} & b_{16} \\ b_{21} & b_{22} & b_{23} & b_{24} & b_{25} & b_{26} \end{bmatrix} \tag{6-13}$$

where $b_{11} = b_{21} = \frac{S\delta}{R_{eff} m v_x}$, $b_{13} = b_{14} = 0$, $b_{15} = \frac{C\delta\left(\bar{C}_{zfr} + \bar{C}_{zfl}\right)}{m v_x}$, $b_{16} = \frac{\bar{C}_{zrr} + \bar{C}_{zrl}}{m v_x}$, and

$$b_{21} = \frac{\frac{d}{2}C\delta + l_f S\delta}{R_{eff} I_z} \tag{6-14}$$

$$b_{22} = \frac{-\frac{d}{2}C\delta + l_f S\delta}{R_{eff} I_z} \tag{6-15}$$

$$b_{23} = \frac{d}{2R_{eff} I_z} \tag{6-16}$$

$$b_{24} = -\frac{d}{2R_{eff} I_z} \tag{6-17}$$

$$b_{25} = \frac{C\delta\left(\bar{C}_{zfr} + \bar{C}_{zfl}\right)l_f - \frac{d}{2}S\delta\left(\bar{C}_{zfr} - \bar{C}_{zfl}\right)}{I_z} \tag{6-18}$$

and

$$C = \begin{bmatrix} 1 & 0 \\ 0 & 0 \end{bmatrix} \tag{6-19}$$

In order to consider the time delays of the actuators, as an alternative to using a traditional method of delay handling with adding a first-order delay block to the control system [99], the dynamics of the actuator are included in the prediction model. To do so, for the electric motors at each corner, a first-order dynamic delay is assumed as $T_{ij} = (1 + \tau s)^{-1} T_{ij,in}$ where τ is the electric motor delay time constant, and $T_{ij,in}$ is the actuator command for the electric motors. Considering this time delay, the electric motors dynamics can be written as:

$$\dot{T}_{ij} = -\frac{1}{\tau} T_{ij} + \frac{1}{\tau} T_{ij,in} \tag{6-20}$$

To model the time delay of the aero surfaces, it was assumed that the angle of attack for each aero surface was controlled through the rotational movement of a DC motor. The resistances in the electrical system and inertia of the mechanical system and linkages of the active aerodynamic wings are the main sources of the time delay of the active aerodynamic system. To simplify the modeling of the time delay for the active aerodynamic surfaces, instead of including the DC motor and mechanical linkage mathematical equations, the following first-order time delay is considered:

$$\dot{\alpha}_{zi} = -\frac{1}{\tau_z} \alpha_{zi} + \frac{1}{\tau_z} \alpha_{zi,in} \tag{6-21}$$

where τ_z is the time constant for the time delay between the requested angle of attack by the system, $\alpha_{zi,in}$, and the actual angles of the aero surfaces.

Considering the Eqs. (6-20) and (6-21), the dynamics of the actuators can be rewritten as:

$$\dot{x}_u = A_u x_u + B_u u_{in} \tag{6-22}$$

where

$$x_u = [T_{fr} \quad T_{fl} \quad T_{rr} \quad T_{rl} \quad \alpha_{zf} \quad \alpha_{zr}]^{\mathrm{T}} \tag{6-23}$$

$$u_{in} = [T_{fr,in} \quad T_{fl,in} \quad T_{rr,in} \quad T_{rl,in} \quad \alpha_{f,in} \quad \alpha_{r,in}]^{\mathrm{T}} \tag{6-24}$$

$$A_u = -diag(\tau^{-1}, \tau^{-1}, \tau^{-1}, \tau^{-1}, \tau_z^{-1}, \tau_z^{-1}) \tag{6-25}$$

$$B_u = diag(\tau^{-1}, \tau^{-1}, \tau^{-1}, \tau^{-1}, \tau_z^{-1}, \tau_z^{-1}) \tag{6-26}$$

where τ and τ_z are the time constant for modeling time delays of electric motors and active aerodynamic systems, respectively. To integrate the actuator dynamics in the control system and prediction model, the state-space model of the control system is combined with Eq. (6-22) as follow:

$$\begin{gathered}\begin{bmatrix}\dot{x}\\ \dot{x}_u\end{bmatrix} = \underbrace{\begin{bmatrix}A & B\\ 0 & A_u\end{bmatrix}}_{\bar{A}}\begin{bmatrix}x\\ x_u\end{bmatrix} + \underbrace{\begin{bmatrix}0\\ B_u\end{bmatrix}}_{\bar{B}} u_{in} + \underbrace{\begin{bmatrix}d\\ 0\end{bmatrix}}_{\bar{d}}\\ Y = \underbrace{[C \quad 0]}_{\bar{C}}\begin{bmatrix}x\\ x_u\end{bmatrix}\end{gathered} \tag{6-27}$$

The Augmented model defined as Eq. (6-27) can be rewritten in the following form:

$$\begin{gathered}\dot{X} = \bar{A}X + \bar{B}u_{in} + \bar{d}\\ Y = \bar{C}X\end{gathered} \tag{6-28}$$

where $X = [x, x_u]^{\mathrm{T}}$ and the augmented matrices $\bar{A}$, $\bar{B}$, $\bar{C}$, and $\bar{d}$ are defined as Eq. (6-27). The step-invariant method is applied to discretize the continuous-time prediction model. Assuming the discrete-time period $t_k \leq t < t_{k+1}$, with the sample time T_s, the discrete-time prediction model is defined as:

$$\begin{aligned} X_{k+1} &= \bar{A}_d X_k + \bar{B}_d u_{in,k} + \bar{d}_d \\ Y_k &= \bar{C}_d X_k \end{aligned} \tag{6-29}$$

where the augmented model matrices are $\bar{A}_d = e^{\bar{A}(t)T_s}$, $\bar{B}_d = \int_0^{T_s} e^{\bar{A}(t)\tau}\bar{B}(t)d\tau$, $\bar{d}_d = \int_0^{T_s} e^{\bar{A}(t)\tau}\bar{d}(t)d\tau$ and $\bar{C}_d = C$.

Remark 1. The presented prediction model is a linear parameter-varying model in which all the parameters in the matrices $\bar{A}$, $\bar{B}$, $\bar{C}$, and $\bar{d}$ are being updated at each operating time according to the available measurements from the vehicle sensors.

The next step is to parametrize the state-space model using the input increments. To do so, the difference of the control inputs are defined as following [100]:

$$\Delta u_{in,k} = u_{in,k} - u_{in,k-1} \tag{6-30}$$

Defining the input as a new state to the state-space model as $X_{u,k} = u_{in,k-1}$, Eq. (6-30) can be written as:

$$X_{u,k+1} = X_{u,k} + \Delta u_{in,k} \tag{6-31}$$

By integrating Eq. (6-31) and Eq. (6-29) the incremental form of the model can be written as:

$$\begin{aligned} \begin{bmatrix} X_{k+1} \\ X_{u,k+1} \end{bmatrix} &= \begin{bmatrix} \bar{A}_d & \bar{B}_d \\ 0 & I \end{bmatrix} \begin{bmatrix} X_k \\ X_{u,k} \end{bmatrix} + \begin{bmatrix} \bar{B}_d \\ 0 \end{bmatrix} \Delta u_{in,k} + \begin{bmatrix} \bar{d}_d \\ 0 \end{bmatrix} \\ Y_k &= [\bar{C}_d \quad 0] \begin{bmatrix} X_k \\ X_{u,k} \end{bmatrix} \end{aligned} \tag{6-32}$$

The augmented model in Eq. (6-32) is the prediction model used in the proposed MPC.

Remark 2. Using input incremental $\Delta u_{in,k}$ as the inputs to the controller has the benefits of simplifying the implementation procedure. It also does not need any steady-state information of the control inputs or state variables [100].

6.1.2. Constraints

In the present study, the two main constraints considered in the design of MPC are input variable constraints and state variable constraints. For the input variables, two types of constraints are included in the system: the constraints on the input increments Δu_{in}, and constraints on the amplitude of the control variables u_{in}.

Input rate constraints:

The constraints defined on the rate of variations of input variables are defined as:

$$\Delta u_{in}^{min} \leq \Delta u_{in} \leq \Delta u_{in}^{max} \tag{6-33}$$

Depending on the nature of the actuator, the value of the maximum and minimum of the input increment changes. For the set of actuators used in this study, the following maximum and minimum values are defined for the optimization problem:

$$\Delta u_{in}^{min} = [\Delta T_{fr,min} \quad \Delta T_{fl,min} \quad \Delta T_{rr,min} \quad \Delta T_{rl,min} \quad \Delta \alpha_{f,min} \quad \Delta \alpha_{r,min}]^{\mathrm{T}} \tag{6-34}$$

$$\Delta u_{in}^{max} = [\Delta T_{fr,max} \quad \Delta T_{fl,max} \quad \Delta T_{rr,max} \quad \Delta T_{rl,max} \quad \Delta \alpha_{f,max} \quad \Delta \alpha_{r,max}]^{\mathrm{T}} \tag{6-35}$$

Input saturation constraints:

Another set of constraints are defined on the amplitude of the control inputs. They are assumed as the upper bound and lower bound of the control inputs as follow:

$$u_{in}^{min} \leq u_{in} \leq u_{in}^{max} \tag{6-36}$$

Considering the actuator capacities, there would be different values for the upper and lower bounds of each actuator. For the first four input variables, the torques to each corner of the vehicle, depends on the variation of the road friction coefficient, the variation of the normal loads acting on the tire, and the combined slip effect of the tire forces, the following constraints are defined for each corner torque:

$$0 \leq T_{ij} \leq \mu g R_{eff} F_{z,ij} \tag{6-37}$$

Remark 3. The normal loads used for constraints are being estimated based on the available measurements at each operating point.

Also, an equality constraint must be defined for the corner torques to guarantee their summation is equal to the total torque requested by the driver:

$$T_{fr} + T_{fl} + T_{rr} + T_{rl} = T_{total} \tag{6-38}$$

The constraints on the other two input variables, the angles of the surface wings, are defined based on the physical limitations of the aero surfaces on changing their angles as follows:

$$\alpha_{zi}^{min} \leq \alpha_{zi} \leq \alpha_{zi}^{max} \tag{6-39}$$

where α_{zi}^{max} is the maximum angle of the front\rear aero surface, and α_{zi}^{min} is the smallest angle.

State variable constraints:

The last set of constraints are defined on the state variables of the vehicle, yaw rate, and sideslip angle. Safe boundaries for the yaw rate and sideslip angle are defined according to the safe envelope

theory [101]. The boundaries for the yaw rate of the vehicle are located on the line of maximum and minimum steady-state yaw rate as follow:

$$r_{ss} = \pm \frac{\mu g}{v_x} \tag{6-40}$$

$$\beta_{max} = \frac{l_r r}{v_x} + \tan(\alpha_{lim}) \tag{6-41}$$

$$\beta_{min} = \frac{l_r r}{v_x} - \tan(\alpha_{lim}) \tag{6-42}$$

Therefore, the constraints on the state variables are defined as:

$$\begin{bmatrix} \beta_{min} \\ r_{ss,min} \end{bmatrix} \leq \begin{bmatrix} \beta \\ r \end{bmatrix} \leq \begin{bmatrix} \beta_{max} \\ r_{ss,max} \end{bmatrix} \tag{6-43}$$

Remark 4. All constraints are being updated in each operating point according to the available measurements and estimations.

6.1.3. High-Level Constraint Adjustment Module

To assure active aerodynamics are actuated only when they are truly necessary, a constraint adjustment module is added to the control system. This module receives the tire force estimation data and calculates the available tire capacity (ATC). A safe margin is defined for activation of the aerodynamic wings that allow them to activate as soon as ATC is less than 20%. In addition, whenever the ATC is more than 20%, the angles of attack changes to zero and deactivate the aero surfaces. The ATC is defined for each tire and whenever each of the tires on the front or rear axles require additional capacity, the active aerodynamic wings related to that axle will be activated. This module will increase the efficiency of the active aerodynamic system, reduce the costs of actuator systems, and improve the performance of the optimization system.

6.1.4. Objective Function

The MPC is designed to track the desired vehicle lateral response. To find the optimal input variables, the following quadratic objective function is defined:

$$J = \frac{1}{2}\sum_{k=1}^{N_p}(\|(Y_k - Y_{des})\|_W^2 + \|\Delta U_k\|_R^2)$$

where W is the outputs weight matrix and R is the input weight matrix. N_p is the number of prediction horizon where in this research set for 15. Considering the sample time $T_s = 10\ ms$, the total length of the predication horizon would be $150\ ms$ which is enough time to see future dynamic behavior of the vehicle. y_{des} is the desired output value which must be tracked by the controller and was defined as Eq. (6-2) in Section 3.1. The schematic structure of the controller is shown in Figure 6-1.

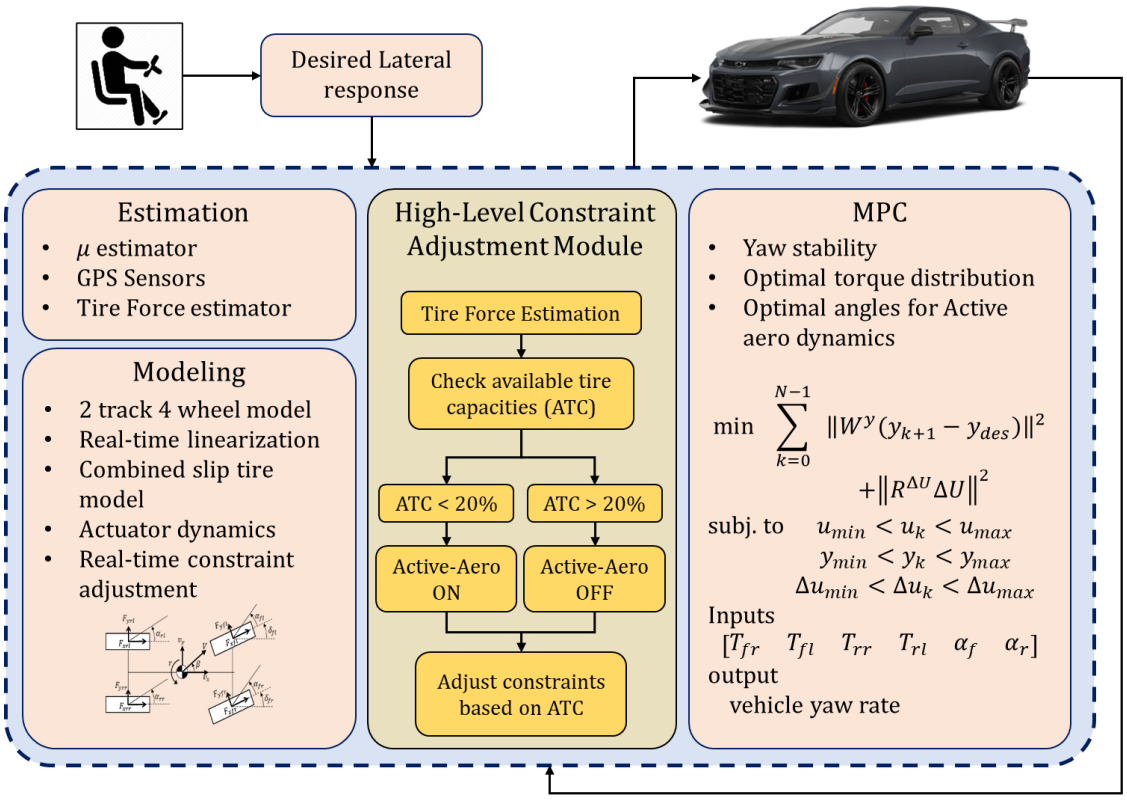

Figure 6-1. Schematic model of the vehicle with active aerodynamic wings at the front and rear of the vehicle

6.2. Simulation Results

In this section, the proposed controller is applied to a high fidelity vehicle model in the CarSim simulation environment. The CarSim model is integrated with the proposed algorithm coded in MATLAB software. The steering angle and the torque command are fed into the model as the driver inputs and the designed controller finds the optimal values of the aero surfaces' angle of attack and corner torques of the vehicle. The physical parameters of the high-fidelity CarSim model used for the simulations are presented in Table 4-1. The results obtained with the proposed controller, which is referred to as Controller B in the figures, are compared with another MPC, which only optimizes the corner torques and does not support the active aerodynamics (Controller A). The designed controller performance is investigated under two different driving scenarios and two different road conditions presented in the following sections.

6.2.1. Sinusoidal Steering Input on Dry Road

The performance of the designed controller is investigated in this section for a driving scenario with sinusoidal steering and constant torque input as shown in Figure 4-10. The vehicle state responses are shown in Figure 6-3 under the effect of two different controllers. The solid black lines shown in this figure represent the state responses of the vehicle with Controller B and the red ones belong to controller A. As shown in Figure 6-3, Controller A is not capable of stabilizing the vehicle and cannot track the desire yaw rate shown as a dashed blue line.

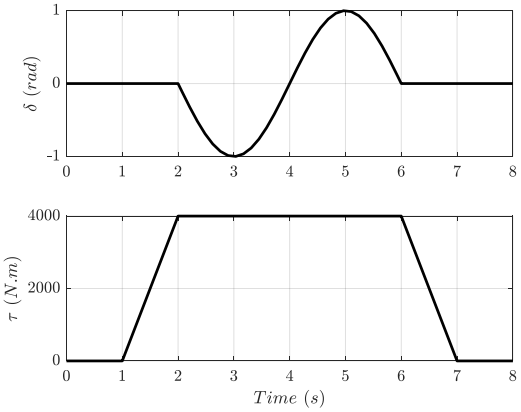

Figure 6-2. Driver Input for slalom on dry road: (a) steering wheel angle, (b) total torque.

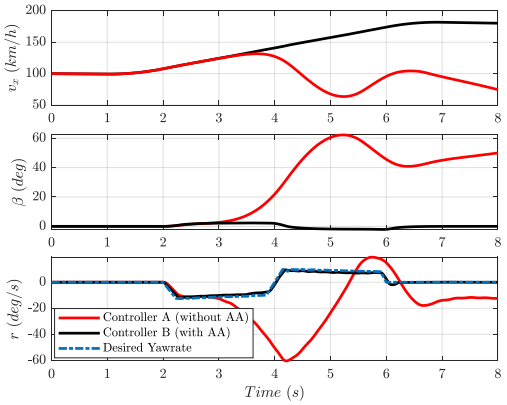

Figure 6-3. State response of the vehicle: (a) longitudinal speed, (b) side slip angle, (c) yaw rate

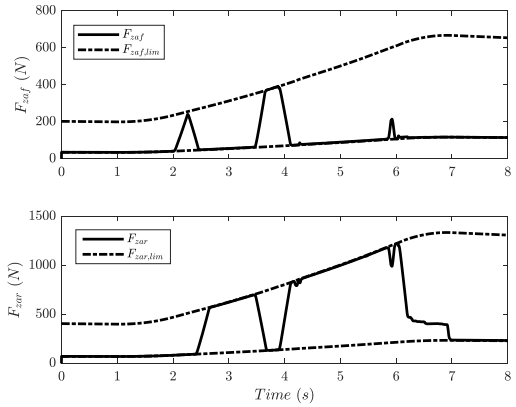

Figure 6-4. Optimal normal loads generated by front and rear aero surfaces

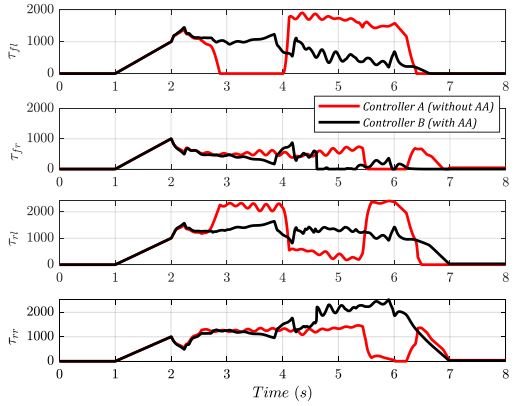

Figure 6-5. Optimal torque command sent to each electric motors

The input variables obtained from Controller B are shown in Figure 6-4 and Figure 6-5. The optimal front and rear normal loads created by the aero surfaces are shown in Figure 6-4. The solid lines show the normal loads and the dashed lines show the boundaries for maximum and minimum normal loads that could be generated with each aero surface. The optimal values of aerodynamic normal loads are calculated based on the optimal angles of attack calculated by controller B and Eq. (5-6). Adding normal loads to the front and rear axles would increase tire capacities in force generation. Depending on the

tire situation, a tire may need extra capacity in either lateral or longitudinal directions. During driving scenarios with high longitudinal accelerations, the normal load transfer from the front axle to the rear axle highly affects the force generation capacities of the front tires. This is where we expect the controller to activate the front aero surface. Since the objective of the controller is to track the desired yaw rate, the controller needs to generate understeer or oversteer yaw moments. The extra yaw moment acting on the vehicle would let the vehicle track the desired yaw rate and remain stable. In this simulation, the activation of the rear aero surface helps to generate an understeer yaw moment, while activating the front aero surface would generate oversteer yaw moment. As can be seen in Figure 6-3, when the acceleration starts, at least one of the tires is getting close to saturation. Therefore, the front active aero starts at time 2 to 2.4 s, Figure 6-4. Then, after $Time = 2.5\ s$, the vehicle body is getting close to oversteering and becoming unstable, as it happens in the vehicle with controller A. At this moment, the controller must create an understeering yaw moment to bring the vehicle back to the stable region.

Consequently, when the vehicle is getting oversteer, Controller A tries to create an understeering yaw moment by transferring the torque from the front-left tire to the rear-left one. Although this torque transfer creates an understeering yaw moment from ΔF_f on the front axle, but decreases the lateral force capacities on the rear axle, which is in contrast with the understeer yaw moment requirement. It also cannot send torque to the rear-right tire to create more understeering yaw moment, there is no more capacity left on the rear-right tire. The reason is the lateral normal load transfer and the fact that the inner tires have less normal loads acting on them during the turning maneuvers. At the same time, controller B starts to activate the rear aero surface to increase rear tire capacities. It also tries to keep the torques on each corner constant, and therefore all extra capacity on rear tires could be used for generating extra lateral forces. Meanwhile, the front wing angle is changing to zero, and then the lateral forces on the front axle decrease. Increasing lateral forces on the rear axle and decreasing lateral forces on the front axle create an adequate amount of understeering yaw moment that can successfully stabilize the vehicle.

6.2.2. Acceleration in Turn on Dry Road

Another driving scenario is designed and simulated on the CarSim high-fidelity model with two controllers A and B. This driving scenario is happening on a dry road with a friction coefficient $\mu = 0.85$. The total torque requested by the driver is $T = 4000\ Nm$ and $1\ rad$ of steering wheel angle is constantly applied 1 second after acceleration is started, Figure 6-6.

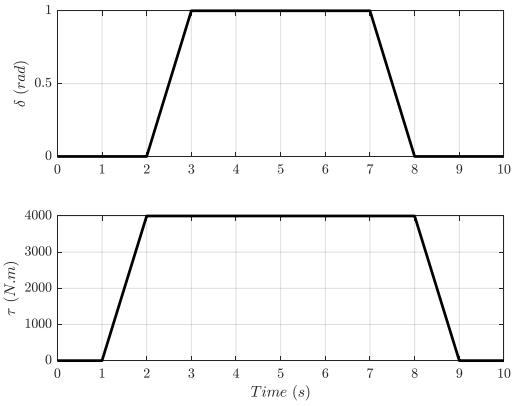

Figure 6-6. Driver Input for turn in acceleration on dry road: (a) steering wheel angle, (b) total torque

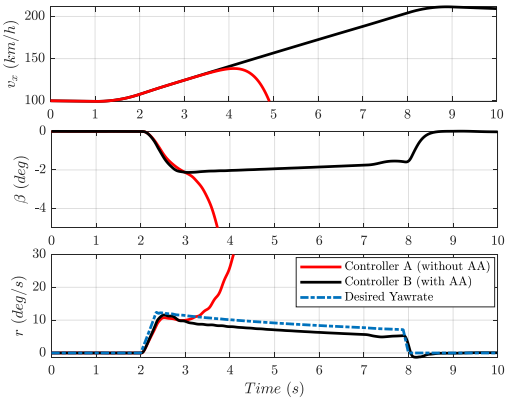

Figure 6-7. Dynamic responses of the vehicle: (a) longitudinal speed, (b) side slip angle, (c) yaw rate

As shown in Figure 6-7, Controller A was not capable of stabilizing the vehicle and after 5 seconds, the simulation stopped. To stabilize the vehicle, Controller A tries to decrease the torque acting on the front-right tire and increases the torques acting on the rear tires, shown in Figure 6-9. Decreasing torque of the front-right tire generates an understeering yaw moment from the longitudinal force differences on the front axle, but increases the lateral force generated by the front-right tire, which is in the fight with the understeer yaw moment generated. At the rear axles, the rear-left tire is saturated and cannot handle any more torque, while the rear-right one is the outer wheel in the turning and have a higher capacity due to the higher normal load acting on it. Therefore, sending torque to the rear cannot be helpful in this situation since it creates an oversteering yaw moment.

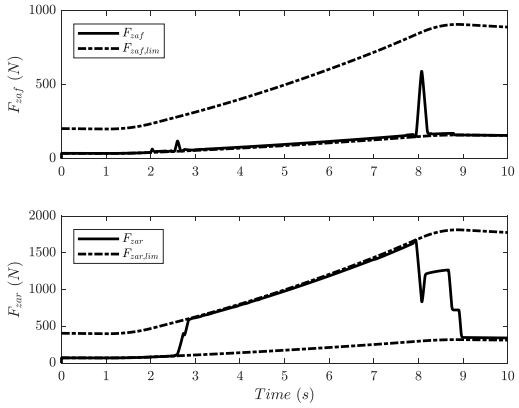

Figure 6-8. Optimal normal loads generated by front and rear aero surfaces

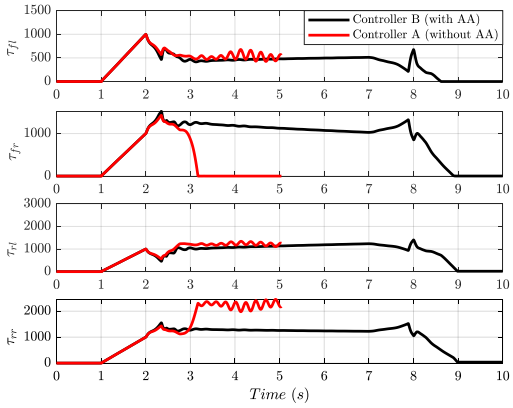

Figure 6-9. Optimal torque command sent to each electric motors

Figure 6-8 shows the way Controller B prevents the front aero surface from activation as soon as it sees the vehicle becomes unstable $t = 2.5s$. Therefore, instead of transferring too much torque from the front axle to the rear one, it activates the rear active aero wing. By activating the rear aero surface and avoiding any huge torque transfer, Controller B increases lateral forces acting on the rear axles, which creates an understeering yaw moment and prevents the vehicle from getting oversteer.

6.2.3. Acceleration in Turn on Wet Road

While driving in wet road conditions, active aerodynamic systems are highly beneficial especially when the vehicle is working at the limits of handling. A good example of such situations is turning in acceleration when the vehicle is being pushed to the limits of handling. Figure 6-10 shows driver torque and steering input for this driving scenario. The total torque of $T = 2800\ Nm$ is applied to the CarSim model with the initial speed $v_x = 70\ kmph$ on a road with friction coefficient $\mu = 0.5$. Although the amount of normal loads created by aero surfaces in this situation is not as high as in previous scenarios, Figure 6-12, they have been very helpful in coordination with optimal torque distribution. As explained before, Controller A could not create enough understeering yaw moment by only transferring torques between corners. Controller B was able to track the desired yaw rate and keep the vehicle in the stable region, Figure 6-11.

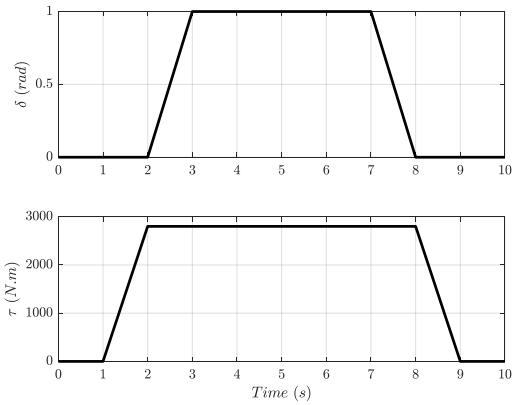

Figure 6-10. Driver Input for turn in acceleration on wet road: (a) steering wheel angle, (b) total torque

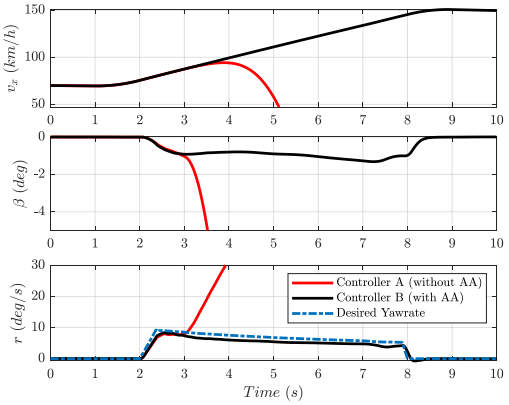

Figure 6-11. State response of the vehicle: (a) longitudinal speed, (b) side slip angle, (c) yaw rate

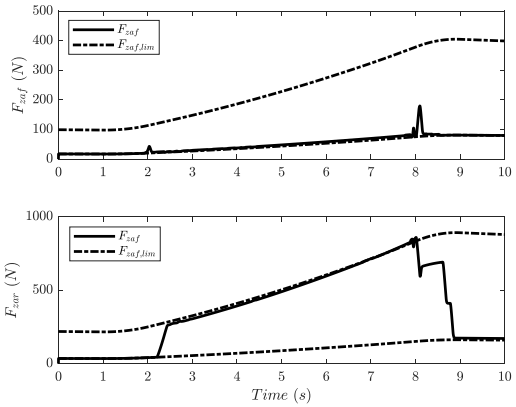

Figure 6-12. Optimal normal loads generated by front and rear aero surfaces

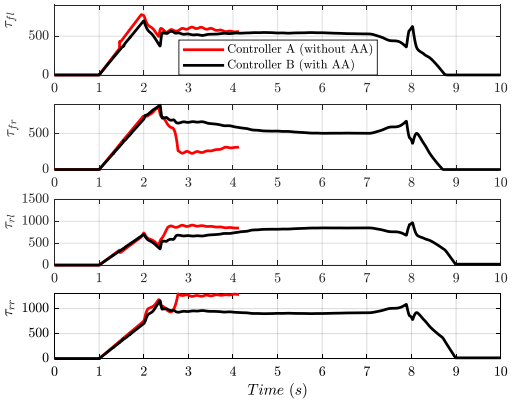

Figure 6-13. Optimal torque command sent to each electric motors

6.3. Summary

In this chapter, a multi-actuation MPC was designed with the objectives of yaw tracking and stabilizing the vehicle lateral dynamics. Active aerodynamic surfaces in the front and rear of the vehicle were added to the vehicle. The MPC optimized the torques allocated to each corner of the vehicle as

well as the active aero surfaces' angles of attack. A high-level constraint adjustment module was designed to observe the tire behavior and the requirement of the active aerodynamic system. The constraint adjustment module enhanced the MPC performance by preventing any unnecessary activation of the aero surfaces. It does not allow the MPC to activate aero surfaces except when one of the axles is close to the force saturation. The performance of the designed predictive controller was evaluated through numerical simulations. It was shown that including the active aerodynamic surfaces as actuators to the control system could increase the stability of the vehicle during harsh maneuvers. Compared to a controller without active aerodynamic elements, the proposed multi-actuation controller showed a much better performance in both yaw tracking and stabilizing the vehicle. Active aero surfaces in the front and rear axle were highly beneficial in creating understeering yaw moments when the vehicle was about to become oversteer. Such benefits are due to the increased tire force capacities resulting from higher normal forces on the tires when active wings are activated.

Chapter 7

Conclusions and Future Work

7.1. Conclusions

In this thesis, an integrated multi-actuation control structure was designed for a performance vehicle. The control structure includes a feedforward controller and a constrained feedback MPC.

The feedforward controller with the objective of maximizing the lateral grip receives the driver command and desired lateral dynamics through the driver command interpreter and optimizes the corner torques and the aero surfaces' angles. Maximizing the lateral grip improved the steerability of the vehicle by preventing the vehicle from getting oversteer or understeer in cornering maneuvers. Having a feedforward controller also improves the aerodynamic system performance by activating the aero surfaces with respect to the driver's command. Due to the open-loop nature of the feedforward controller, the actuation commands do not have to wait for the feedback error signals and will be activated as soon as the driver's commands are applied. Therefore, the feedforward controller enhances both the performance of the feedback controller and the overall performance of the vehicle. To design the feedforward controller, first, a sensitivity analysis was performed on the open-loop vehicle dynamics using sideslip angle and yaw rate phase portraits. The effect of various torque distribution ratios on the nonlinear dynamics and equilibrium points concluded that sending more torque to the rear axle changes the location of the saddle points closer to the center of the phase plane. As the saddle points move closer to the center of the phase plane, the safe envelop shrinks and the vehicle becomes unstable faster. This is while sending torque to the front axle moves the location of the saddle points farther from the center of the phase plane and increases the size of the safe envelope. Therefore, it was

necessary to find an optimum ratio for the torque distribution at each driving moment to have the maximum lateral grip and for performing sharp cornering maneuvers without any oversteering or understeering. Having a real-time optimal torque distribution with the objective of maximizing the lateral grip perfectly solved the problem of torque distribution. The optimal axial torque distribution algorithm was implemented as a feedforward controller and evaluated through simulations and experimental studies.

The optimal axial torque distribution algorithm was extended to a corner-base configuration which could optimally distribute driver torque input into all the corners. The corner-base version of the optimal torque distribution was also implemented in the form of a feedforward controller and it was shown that it could successfully maximize the lateral grip and enhance the vehicle maneuverability during harsh cornering maneuvers. Optimizing the torque corners resulted in a 45% increase in the lateral acceleration compared to an AWD vehicle with the constant torque distribution. Comparing the experimental results of an axial torque distribution with the corner torque distribution strategies, it was shown that the lateral acceleration reached to an approximate 30% higher value when the torque corners were optimized.

Although the feedforward controller enhanced the vehicle maneuverability, a feedback controller was required to assure stability and yaw tracking of the vehicle. The designed multi-actuation constrained feedback MPC successfully tracked the desired lateral dynamics and optimized the actuation commands. Due to the high number of actuators, a real-time constraint adjustment module was designed to observe the overall behavior of the vehicle. If the operation of an actuator was not necessary at a moment, the constraint adjustment module would close the boundaries of the actuator constraint to prevent it from being activated. The constraint adjustment module successfully improved the performance of the designed MPC and reduced the operation of actuators when not needed.

Integration of the optimal torque distribution and active aerodynamic system let a performance driver request more traction/brake torque during high-speed maneuvers. Activating the aero surfaces at the front and rear of the vehicle balanced the normal load distribution at the corners. It also lets the optimal torque distribution strategy to better stabilize the vehicle during harsh cornering maneuvers.

7.2. Future Work

For the extension of the studies performed in this thesis, here are suggestions, which can be considered for future works:

- **Feedback Controller for Maximizing lateral grip**

The designed feedforward controller can use feedback sensory information to increase the accuracy and performance of the optimal torque distribution strategy. It should be noted that the objective of the designed torque distribution strategy is to maximize the lateral grip. Therefore, in some cases, this objective can be in the fight with the objective of the yaw tracking feedback controller. Therefore, the conflict between these two main objectives must be studied carefully.

- **Increasing optimal torque distribution robustness to the friction coefficient**

As mentioned in the thesis, the friction coefficient plays a key role in the optimal torque distribution strategy. In a worst-case scenario, if the friction coefficient cannot be estimated accurately, a special condition can be defined for the controller to adjust the constraints respectively. For instance, if the friction coefficient is not accurate and the vehicle is losing its stability, the optimization constraints can be adjusted and be set to the previously defined extreme case parameters to consider the friction coefficient in its minimum value and keep the vehicle stable.

- **Including road angles in the control design:**

In Chapter 3, the dynamic model of a vehicle moving on a road with bank and grade angles was developed. This model can be used as the MPC prediction model to extend this work to non-flat roads. When a traditional vehicle dynamic model that does not consider road angles is used as the prediction model, the controller performance might be compromised when the vehicle drives on non-flat roads. Adding road angles to the state-space can make the prediction model more precise and result in a better performance of the control system when the vehicle is moving on a road with bank and grade angles.

- **Adding longitudinal dynamics in the modeling and control design:**

The longitudinal dynamics can be added to the open-loop analysis performed on the 2-D phase portraits. 3-D phase portraits are also great tools for analyzing nonlinear vehicle dynamics. In addition, the longitudinal dynamics can be added to the state-space model. In this thesis, the longitudinal speed was assumed constant during the prediction horizon and was updated only at each time step through

available sensory measurements. By considering the longitudinal speed as a state variable, its value will be updated during the prediction horizon and it will improve the performance of the MPC. It should be mentioned that adding longitudinal speed as a state will increase the nonlinearity of the model, and the prediction model must be linearized or a nonlinear MPC must be used to solve the problem.

- **Feedforward controller in the form of MPC:**

For improving the performance of the feedforward controller, both for maximizing the lateral grip and for activating aerodynamic surfaces, the optimization can be replaced by a model predictive structure to improve the accuracy and performance of the feedforward control systems.

- **Adding wheel dynamics to the control structure:**

To improve the accuracy of the optimal torque distribution, wheel dynamics can be added to the state-space model. This would allow estimation of longitudinal forces with a lower error by including the wheel spin and slip ratio effect on the tire force generations. In addition, wheel stability control can be added to the multi-actuator control structure to help the prediction model better detect tire saturation.

- **Adding roll dynamics:**

Adding roll dynamics will allow incorporating the lateral load transfers during cornering maneuvers in the controller. This would improve the feedforward controller by generating more accurate normal load estimations, and the MPC feedback controller to have a more accurate prediction model. The accuracy in normal load prediction also enhances the controller performance by having a more accurate tire model and estimating lateral tire forces better.

References

[1] H. Pacejka, *Tire and vehicle dynamics*. Elsevier, 2005.

[2] K. Kritayakirana and J. C. Gerdes, "Autonomous vehicle control at the limits of handling," *Int. J. Veh. Auton. Syst.*, vol. 10, no. 4, pp. 271–296, 2012.

[3] A. M. Daher, C. R. Bardawil, and N. A. Daher, "Vehicle stability based on g−g diagram through braking and driveline," in *2017 American Control Conference (ACC)*, 2017, pp. 309–314, doi: 10.23919/ACC.2017.7962971.

[4] U. Kalabić, A. Chakrabarty, R. Quirynen, and S. Di Cairano, "Learning autonomous vehicle passengers' preferred driving styles using g-g plots and haptic feedback," in *2019 IEEE Intelligent Transportation Systems Conference (ITSC)*, 2019, pp. 4012–4017, doi: 10.1109/ITSC.2019.8917328.

[5] J. Ni, J. Hu, and C. Xiang, "Robust Path Following Control at Driving/Handling Limits of an Autonomous Electric Racecar," *IEEE Trans. Veh. Technol.*, vol. 68, no. 6, pp. 5518–5526, 2019, doi: 10.1109/TVT.2019.2911862.

[6] R. S. Rice, "Measuring car-driver interaction with the g-g diagram," *SAE Technical Papers*. 1973, doi: 10.4271/730018.

[7] J. Ni and J. Hu, "Dynamics control of autonomous vehicle at driving limits and experiment on an autonomous formula racing car," *Mech. Syst. Signal Process.*, vol. 90, pp. 154–174, 2017.

[8] K. Kritayakirana and J. C. Gerdes, "Autonomous cornering at the limits: Maximizing a 'gg' diagram by using feedforward trail-braking and throttle-on-exit," *IFAC Proc. Vol.*, vol. 43, no. 7, pp. 548–553, 2010.

[9] K. Sawase and Y. Ushiroda, "Improvement of vehicle dynamics by right-and-left torque vectoring system in various drivetrains," *Mitsubishi Mot. Tech. Rev.*, vol. 20, pp. 14–20, 2008.

[10] M. Klomp, "Longitudinal force distribution using quadratically constrained linear

programming," *Veh. Syst. Dyn.*, vol. 49, no. 12, pp. 1823–1836, 2011.

[11] J. Ni, J. Hu, and C. Xiang, "Envelope control for four-wheel independently actuated autonomous ground vehicle through AFS/DYC integrated control," *IEEE Trans. Veh. Technol.*, vol. 66, no. 11, pp. 9712–9726, 2017.

[12] Y. Matsuo, A. Okada, S. Kasuga, and S. Sekido, "Intelligent four-wheel-drive system," SAE Technical Paper, 1993.

[13] M. Klomp, *Longitudinal force distribution and road vehicle handling*. Chalmers University of Technology, 2010.

[14] R. Rieveley, "The Effect of Direct Yaw Moment on Human Controlled Vehicle Systems," 2010.

[15] K. Sawase and Y. Sano, "Application of active yaw control to vehicle dynamics by utilizing driving/breaking force," *JSAE Rev.*, vol. 20, no. 2, pp. 289–295, 1999.

[16] M. Klomp and R. Thomson, "Influence of front/rear drive force distribution on the lateral grip and understeer of all-wheel drive vehicles," *Int. J. Veh. Des.*, vol. 56, no. 1–4, pp. 34–48, 2011.

[17] R. Rajamani, N. Piyabongkarn, J. Lew, K. Yi, and G. Phanomchoeng, "Tire-road friction-coefficient estimation," *IEEE Control Syst. Mag.*, vol. 30, no. 4, pp. 54–69, 2010.

[18] J. Wang, L. Alexander, and R. Rajamani, "Friction estimation on highway vehicles using longitudinal measurements," *J. Dyn. Sys., Meas., Control*, vol. 126, no. 2, pp. 265–275, 2004.

[19] R. Rajamani, G. Phanomchoeng, D. Piyabongkarn, and J. Y. Lew, "Algorithms for real-time estimation of individual wheel tire-road friction coefficients," *IEEE/ASME Trans. Mechatronics*, vol. 17, no. 6, pp. 1183–1195, 2011.

[20] Y.-H. J. Hsu, S. M. Laws, and J. C. Gerdes, "Estimation of tire slip angle and friction limits using steering torque," *IEEE Trans. Control Syst. Technol.*, vol. 18, no. 4, pp. 896–907, 2009.

[21] S. H. Strogatz, *Nonlinear dynamics and chaos with student solutions manual: With applications to physics, biology, chemistry, and engineering*. CRC press, 2018.

[22] K. Liu, J. Gong, S. Chen, Y. Zhang, and H. Chen, “Model predictive stabilization control of high-speed autonomous ground vehicles considering the effect of road topography,” *Appl. Sci.*, vol. 8, no. 5, p. 822, 2018.

[23] M. V Cook, *Flight dynamics principles: a linear systems approach to aircraft stability and control*. Butterworth-Heinemann, 2012.

[24] S. M. Erlien, S. Fujita, and J. C. Gerdes, “Safe driving envelopes for shared control of ground vehicles,” *IFAC Proc. Vol.*, vol. 46, no. 21, pp. 831–836, 2013.

[25] Y. Huang, W. Liang, and Y. Chen, “Stability Regions of Vehicle Lateral Dynamics: Estimation and Analysis,” *J. Dyn. Syst. Meas. Control*, vol. 143, no. 5, 2020.

[26] C. Tang and A. Khajepour, “Integrated Stability Control for Narrow Tilting Vehicles: An Envelope Approach,” *IEEE Trans. Intell. Transp. Syst.*, 2020.

[27] Y. Huang and Y. Chen, “Vehicle Lateral Stability Control Based on Shiftable Stability Regions and Dynamic Margins,” *IEEE Trans. Veh. Technol.*, 2020.

[28] S. Inagaki, I. Kushiro, and M. Yamamoto, “Analysis on vehicle stability in critical cornering using phase-plane method,” *Jsae Rev.*, vol. 2, no. 16, p. 216, 1995.

[29] C. E. Beal, *Applications of model predictive control to vehicle dynamics for active safety and stability*. Stanford University, 2011.

[30] C. E. Beal and J. C. Gerdes, “Model predictive control for vehicle stabilization at the limits of handling,” *IEEE Trans. Control Syst. Technol.*, vol. 21, no. 4, pp. 1258–1269, 2012.

[31] M. Brown, J. Funke, S. Erlien, and J. C. Gerdes, “Safe driving envelopes for path tracking in autonomous vehicles,” *Control Engineering Practice*, vol. 61. pp. 307–316, 2017, doi: 10.1016/j.conengprac.2016.04.013.

[32] C. G. Bobier and J. C. Gerdes, “Staying within the nullcline boundary for vehicle envelope control using a sliding surface,” *Veh. Syst. Dyn.*, vol. 51, no. 2, pp. 199–217, 2013.

[33] S. M. Erlien, S. Fujita, and J. C. Gerdes, “Shared Steering Control Using Safe Envelopes for Obstacle Avoidance and Vehicle Stability,” *IEEE Transactions on Intelligent Transportation Systems*, vol. 17, no. 2. pp. 441–451, 2016, doi: 10.1109/TITS.2015.2453404.

[34] C. G. Bobier-Tiu, C. E. Beal, J. C. Kegelman, R. Y. Hindiyeh, and J. C. Gerdes, “Vehicle control synthesis using phase portraits of planar dynamics,” *Veh. Syst. Dyn.*, vol. 57, no. 9, pp. 1318–1337, 2019.

[35] C. E. Beal and C. Boyd, “Coupled lateral-longitudinal vehicle dynamics and control design with three-dimensional state portraits,” *Veh. Syst. Dyn.*, vol. 57, no. 2, pp. 286–313, 2019.

[36] L. Guo, P. Ge, and D. Sun, “Torque Distribution Algorithm for Stability Control of Electric Vehicle Driven by Four In-Wheel Motors Under Emergency Conditions,” *IEEE Access*, vol. 7, pp. 104737–104748, 2019, doi: 10.1109/ACCESS.2019.2931505.

[37] E. Joa, K. Park, Y. Koh, K. Yi, and K. Kim, “A tyre slip-based integrated chassis control of front/rear traction distribution and four-wheel independent brake from moderate driving to limit handling,” *Veh. Syst. Dyn.*, vol. 56, no. 4, pp. 579–603, 2018.

[38] Y. Chen, S. Chen, Y. Zhao, Z. Gao, and C. Li, “Optimized Handling Stability Control Strategy for a Four In-Wheel Motor Independent-Drive Electric Vehicle,” *IEEE Access*, vol. 7, pp. 17017–17032, 2019, doi: 10.1109/ACCESS.2019.2893894.

[39] D. Mikle and M. Bat’a, “Torque Vectoring for an Electric All-wheel Drive Vehicle,” *IFAC-PapersOnLine*, vol. 52, no. 27, pp. 163–169, 2019, doi: https://doi.org/10.1016/j.ifacol.2019.12.750.

[40] M. Chae, Y. Hyun, K. Yi, and K. Nam, “Dynamic Handling Characteristics Control of an in-Wheel-Motor Driven Electric Vehicle Based on Multiple Sliding Mode Control Approach,” *IEEE Access*, vol. 7, pp. 132448–132458, 2019, doi: 10.1109/ACCESS.2019.2940434.

[41] J. Liu, H. Zhong, L. Wang, and H. Chen, “A Novel Torque Distribution Strategy for Distributed-Drive Electric Vehicle Considering Energy Saving and Brake Stability,” SAE Technical Paper, 2019.

[42] T. Goggia *et al.*, “Integral sliding mode for the torque-vectoring control of fully electric vehicles: Theoretical design and experimental assessment,” *IEEE Trans. Veh. Technol.*, vol. 64, no. 5, pp. 1701–1715, 2014.

[43] Y. Ren, G. Yin, G. Li, T. Xia, J. Liang, and V. Meyer, “A Real-time and Parameterized

Optimal Torque Distribution Strategy for 4WID Electric Vehicle without Road Adhesion Information," in *2019 3rd Conference on Vehicle Control and Intelligence (CVCI)*, 2019, pp. 1–6.

[44] A. M. Dizqah, B. Lenzo, A. Sorniotti, P. Gruber, S. Fallah, and J. De Smet, "A fast and parametric torque distribution strategy for four-wheel-drive energy-efficient electric vehicles," *IEEE Trans. Ind. Electron.*, vol. 63, no. 7, pp. 4367–4376, 2016.

[45] E. Esmailzadeh, G. R. Vossoughi, and A. Goodarzi, "Dynamic modeling and analysis of a four motorized wheels electric vehicle," *Veh. Syst. Dyn.*, vol. 35, no. 3, pp. 163–194, 2001.

[46] E. Esmailzadeh, A. Goodarzi, and G. R. Vossoughi, "Optimal yaw moment control law for improved vehicle handling," *Mechatronics*, vol. 13, no. 7, pp. 659–675, 2003.

[47] A. Goodarzi and E. Esmailzadeh, "Design of a VDC system for all-wheel independent drive vehicles," *IEEE/ASME Trans. Mechatronics*, vol. 12, no. 6, pp. 632–639, 2007.

[48] Y. Cao, L. Zhai, T. Sun, and H. Gu, "Straight Running Stability Control Based on Optimal Torque Distribution for a Four in-wheel Motor Drive Electric Vehicle," *Energy Procedia*, vol. 105, pp. 2825–2830, 2017, doi: https://doi.org/10.1016/j.egypro.2017.03.616.

[49] L. Zhai, T. Sun, and J. Wang, "Electronic stability control based on motor driving and braking torque distribution for a four in-wheel motor drive electric vehicle," *IEEE Trans. Veh. Technol.*, vol. 65, no. 6, pp. 4726–4739, 2016.

[50] H. Her, Y. Koh, E. Joa, K. Yi, and K. Kim, "An integrated control of differential braking, front/rear traction, and active roll moment for limit handling performance," *IEEE Trans. Veh. Technol.*, vol. 65, no. 6, pp. 4288–4300, 2015.

[51] J. Huang, Y. Liu, M. Liu, M. Cao, and Q. Yan, "Multi-Objective Optimization Control of Distributed Electric Drive Vehicles Based on Optimal Torque Distribution," *IEEE Access*, vol. 7, pp. 16377–16394, 2019, doi: 10.1109/ACCESS.2019.2894259.

[52] C. Lin, S. Liang, J. Chen, and X. Gao, "A Multi-Objective Optimal Torque Distribution Strategy for Four In-Wheel-Motor Drive Electric Vehicles," *IEEE Access*, vol. 7, pp. 64627–64640, 2019, doi: 10.1109/ACCESS.2019.2917313.

[53] A. Tahouni, M. Mirzaei, and B. Najjari, “Novel Constrained Nonlinear Control of Vehicle Dynamics Using Integrated Active Torque Vectoring and Electronic Stability Control,” *IEEE Trans. Veh. Technol.*, vol. 68, no. 10, pp. 9564–9572, 2019, doi: 10.1109/TVT.2019.2933229.

[54] J. Velazquez Alcantar and F. Assadian, “Vehicle dynamics control of an electric-all-wheel-drive hybrid electric vehicle using tyre force optimisation and allocation,” *Veh. Syst. Dyn.*, vol. 57, no. 12, pp. 1897–1923, Dec. 2019, doi: 10.1080/00423114.2019.1585556.

[55] H. Pacejka, *Tire and Vehicle Dynamics*. Elsevier, 2012.

[56] J. Katz, “Aerodynamic model for wing-generated down force on open-wheel-racing-car configurations,” *SAE Trans.*, pp. 1106–1115, 1986.

[57] P. G. Wright, “The influence of aerodynamics on the design of Formula One racing cars,” *Int. J. Veh. Des.*, vol. 3, no. 4, pp. 383–397, 1982.

[58] S. Codling, G. Murray, and P. Windsor, *Art of the Formula 1 race car*. MotorBooks International, 2010.

[59] K. Kurec, M. Remer, and J. Piechna, “The influence of different aerodynamic setups on enhancing a sports car’s braking,” *Int. J. Mech. Sci.*, vol. 164, p. 105140, 2019.

[60] M. Hammad, K. Qureshi, and Y. He, “Safety and Lateral Dynamics Improvement of a Race Car Using Active Rear Wing Control,” SAE Technical Paper, 2019.

[61] L. W. Yew, A. S. M. Al-Obaidi, and S. Namasivayam, “Design and Development of a Multi-Element Active Aerodynamic Package to Enhance the Performance of Taylor’s Formula SAE Car,” 2017.

[62] K. Kurec, M. Remer, J. Broniszewski, P. Bibik, S. Tudruj, and J. Piechna, “Advanced modeling and simulation of vehicle active aerodynamic safety,” *J. Adv. Transp.*, vol. 2019, 2019.

[63] J. Cai, S. Kapoor, T. Sikder, and Y. He, “Effects of Active Aerodynamic Wings on Handling Performance of High-Speed Vehicles,” SAE Technical Paper, 2017.

[64] R. Tarulescu, S. Tarulescu, and C. Leahu, “Downforce variation dependence of angle of incidence modification for the rear wing of high speed vehicles,” in *IOP Conference Series:*

Materials Science and Engineering, 2017, vol. 252, p. 12025.

[65] A. Barari, F. Diba, and E. Esmailzadeh, "Down force control of the low velocity racing car using active aerodynamic inverse wings," *Proceedings of the ASME Design Engineering Technical Conference*, vol. 8. pp. 739–745, 2011, doi: 10.1115/DETC2011-48308.

[66] A. H. Shahein, A. A. Ata, E. H. Haraz, and B. M. El-Souhily, "Vibration suppression of terrains irregularities using active aerodynamic surface for half-car model sport vehicles," *J. Vib. Control*, p. 1077546320915316, 2020.

[67] M. Corno, S. Bottelli, M. Tanelli, C. Spelta, and S. M. Savaresi, "Active control of aerodynamic surfaces for ride control in sport vehicles," *IFAC Proc. Vol.*, vol. 47, no. 3, pp. 7553–7558, 2014.

[68] M. Corno, S. Bottelli, G. Panzani, C. Spelta, M. Tanelli, and S. M. Savaresi, "Performance Assessment of Active Aerodynamic Surfaces for Comfort and Handling Optimization in Sport Cars," *IEEE Trans. Control Syst. Technol.*, vol. 24, no. 1, pp. 189–199, 2016, doi: 10.1109/TCST.2015.2424158.

[69] J. Meder, T. Wiegand, and M. Pfadenhauer, "Adaptive aerodynamics of the new Porsche 911 Turbo," *ATZ worldwide*, vol. 116, no. 2. pp. 42–45, 2014, doi: 10.1007/s38311-014-0023-4.

[70] F. Diba, A. Barari, and E. Esmailzadeh, "Handling and safety enhancement of race cars using active aerodynamic systems," *Veh. Syst. Dyn.*, vol. 52, no. 9, pp. 1171–1190, 2014.

[71] D. T. Ayyagari and Y. He, "Aerodynamic analysis of an active rear split spoiler for improving lateral stability of high-speed vehicles," *Int. J. Veh. Syst. Model. Test.*, vol. 12, no. 3–4, pp. 217–239, 2017.

[72] Z. Chen, Y. Wu, and F. Li, "Integrated Control of Differential Braking and Active Aerodynamic Control for Improving High Speed Stability of Vehicles," *Int. J. Automot. Technol.*, vol. 21, no. 1, pp. 61–70, 2020.

[73] A. H. Ahangarnejad, S. Melzi, and M. Ahmadian, "Integrated Vehicle Dynamics System through Coordinating Active Aerodynamics Control, Active Rear Steering, Torque Vectoring and Hydraulically Interconnected Suspension," *Int. J. Automot. Technol.*, vol. 20, no. 5, pp.

903–915, 2019.

[74] M. Hammad, “Design and analysis of active aerodynamic control systems for increasing the safety of high-speed road vehicles.” 2019.

[75] K. Shi, X. Yuan, and Q. He, “Double-layer dynamic decoupling control system for the yaw stability of four wheel steering vehicle,” *Int. J. Control. Autom. Syst.*, vol. 17, no. 5, pp. 1255–1263, 2019.

[76] C. Sun, X. Zhang, Q. Zhou, and Y. Tian, “A model predictive controller with switched tracking error for autonomous vehicle path tracking,” *IEEE Access*, vol. 7, pp. 53103–53114, 2019.

[77] S. Li, G. Wang, B. Zhang, Z. Yu, and G. Cui, “Vehicle Yaw Stability Control at the Handling Limits Based on Model Predictive Control,” *Int. J. Automot. Technol.*, vol. 21, no. 2, pp. 361–370, 2020.

[78] M. Ataei, A. Khajepour, and S. Jeon, “Model Predictive Control for integrated lateral stability, traction/braking control, and rollover prevention of electric vehicles,” *Veh. Syst. Dyn.*, vol. 58, no. 1, pp. 49–73, 2020.

[79] Y. Zhang, A. Khajepour, and M. Ataei, “A universal and reconfigurable stability control methodology for articulated vehicles with any configurations,” *IEEE Trans. Veh. Technol.*, vol. 69, no. 4, pp. 3748–3759, 2020.

[80] Y. Zhang, “Multi-axle vehicle modeling and stability control: A reconfigurable approach,” 2019.

[81] H. Li and Y. Luo, “Integrated Coordination Control for Distributed Drive Electric Vehicle Trajectory Tracking,” *Int. J. Automot. Technol.*, vol. 21, no. 4, pp. 1047–1060, 2020.

[82] M. Fnadi, W. Du, F. Plumet, and F. Benamar, “Constrained Model Predictive Control for dynamic path tracking of a bi-steerable rover on slippery grounds,” *Control Eng. Pract.*, vol. 107, p. 104693.

[83] E. Hashemi, M. Jalali, A. Khajepour, A. Kasaiezadeh, and S.-K. Chen, “Vehicle Stability Control: Model Predictive Approach and Combined-Slip Effect,” *IEEE/ASME Trans.*

Mechatronics, 2020.

[84] L. Yang, M. Yue, H. Tian, and B. Yao, “Tire blow-out control for direct drive electric vehicles using reconfiguration of torque distribution and vertical load,” *Trans. Inst. Meas. Control*, vol. 42, no. 8, pp. 1547–1558, 2020.

[85] A. Nahidi, A. Kasaiezadeh, S. Khosravani, A. Khajepour, S.-K. Chen, and B. Litkouhi, “Modular integrated longitudinal and lateral vehicle stability control for electric vehicles,” *Mechatronics*, vol. 44, pp. 60–70, 2017.

[86] J. Nah and S. Yim, “Vehicle Stability Control with Four-Wheel Independent Braking, Drive and Steering on In-Wheel Motor-Driven Electric Vehicles,” *Electronics*, vol. 9, no. 11, p. 1934, 2020.

[87] L. Zhang *et al.*, “Model predictive control for integrated longitudinal and lateral stability of electric vehicles with in-wheel motors,” *IET Control Theory Appl.*, vol. 14, no. 18, pp. 2741–2751, 2020.

[88] K. C. Veluvolu, J. J. Rath, M. Defoort, and Y. C. Soh, “Estimation of side slip and road bank angle using high-gain observer and higher-order sliding mode observer,” in *2015 International Workshop on Recent Advances in Sliding Modes (RASM)*, 2015, pp. 1–6.

[89] B. L. Boada, D. Garcia-Pozuelo, M. J. L. Boada, and V. Diaz, “A constrained dual Kalman filter based on pdf truncation for estimation of vehicle parameters and road bank angle: Analysis and experimental validation,” *IEEE Trans. Intell. Transp. Syst.*, vol. 18, no. 4, pp. 1006–1016, 2016.

[90] J. Ryu and J. C. Gerdes, “Estimation of vehicle roll and road bank angle,” in *Proceedings of the 2004 American control conference*, 2004, vol. 3, pp. 2110–2115.

[91] H. F. Grip, L. Imsland, T. A. Johansen, J. C. Kalkkuhl, and A. Suissa, “Estimation of road inclination and bank angle in automotive vehicles,” in *2009 American control conference*, 2009, pp. 426–432.

[92] S. Kidane, L. Alexander, R. Rajamani, P. Starr, and M. Donath, “Road bank angle considerations in modeling and tilt stability controller design for narrow commuter vehicles,”

in *2006 American control conference*, 2006, pp. 6-pp.

[93] Y. Guizhen, L. Honggang, W. Pengcheng, W. Xinkai, and W. Yunpeng, "Real-time bus rollover prediction algorithm with road bank angle estimation," *Chaos, Solitons & Fractals*, vol. 89, pp. 270–283, 2016.

[94] B. L. Stevens, F. L. Lewis, and E. N. Johnson, *Aircraft control and simulation: dynamics, controls design, and autonomous systems*. John Wiley & Sons, 2015.

[95] R. Rajamani, *Vehicle dynamics and control*. Springer Science & Business Media, 2011.

[96] H. Pacejka, "Tire and Vehicle Dynamics," *Tire and Vehicle Dynamics*. 2012, doi: 10.1016/C2010-0-68548-8.

[97] C. G. Bobier, "A phase portrait approach to vehicle stabilization and envelope control." Stanford University, 2012.

[98] M. Pourahmadi, "Taylor expansion of and some applications," *Am. Math. Mon.*, vol. 91, no. 5, pp. 303–307, 1984.

[99] M. Jalali, A. Khajepour, S. Chen, and B. Litkouhi, "Handling delays in yaw rate control of electric vehicles using model predictive control with experimental verification," *J. Dyn. Syst. Meas. Control*, vol. 139, no. 12, 2017.

[100] L. Wang, *Model predictive control system design and implementation using MATLAB®*. Springer Science & Business Media, 2009.

[101] C. G. Bobier-Tiu, C. E. Beal, J. C. Kegelman, R. Y. Hindiyeh, and J. C. Gerdes, "Vehicle control synthesis using phase portraits of planar dynamics," *Vehicle System Dynamics*, vol. 57, no. 9. pp. 1318–1337, 2019, doi: 10.1080/00423114.2018.1502456.